

**Structural Relaxation and the Glass Transition  
in Metallic Glasses**

by

Ralf Brüning, M.Sc.  
Department of Physics, McGill University  
Montreal, Canada

A Thesis submitted to the  
Faculty of Graduate Studies and Research  
in partial fulfillment of the requirements for the degree of  
Doctor of Philosophy

© Ralf Brüning, 1990

## Abstract

This thesis presents for the first time direct structural measurements of both reversible and irreversible structural relaxation and the glass transition in the metal-metalloid glass  $\text{Pd}_{40}\text{Ni}_{40}\text{P}_{20}$ . The techniques have been x-ray diffraction and Mössbauer spectroscopy, and a new analysis method for changes of amorphous diffraction patterns was developed.

It is found that irreversible relaxation proceeds by many local shear-type motions involving the metal atoms, and that it is accompanied by a small densification. Reversible relaxation at high annealing temperatures entails the same microscopic processes, but it does not change the density of the glass. The type of atomic processes changes continuously as the annealing temperature is lowered, and at sufficiently low temperatures the distribution of metal atoms remains constant, so that reversible relaxation then proceeds via rearrangement of the metalloid atoms. This rearrangement leads to more ordered, but less isotropic atomic sites.

The second part of the thesis is concerned with the motion of the atoms in a metallic glass below and above the glass transition. Mössbauer spectroscopy allows the direct measurement of vibrational and diffusional motion. The increase of the amplitude of atomic vibration has the same temperature dependence as the increase in volume that marks the glass transition, thus the two processes are governed by the same mechanism. The directly measured diffusional motion is in agreement with macroscopic measurements of diffusion.

## Résumé

Cette thèse présente pour la première fois des mesures directes des relaxations structurelles réversibles et irréversibles et de la transition vitreuse dans le  $\text{Pd}_{40}\text{Ni}_{40}\text{P}_{20}$ . La diffraction des rayons X et la spectroscopie Mössbauer ont été employées, et une nouvelle méthode d'analyse pour la variation dans les profils de diffraction amorphes a été développée.

Il est obtenu que la relaxation irréversible procède par mouvement local en cission faisant intervenir les atomes métalliques et s'accompagne d'une faible augmentation de densité. La relaxation réversible à des températures de recuit élevées fait intervenir les mêmes processus microscopiques mais sans modifier la densité du verre. Le type de processus atomique change de manière continue avec la diminution de la température de recuit et, à des températures suffisamment basses, la distribution des atomes métalliques demeure constante. Par contre, les déplacements des atomes métalloïdes entraînent des sites atomiques plus ordonnés mais moins isotropiques.

La seconde partie de cette thèse est consacrée à l'étude du mouvement des atomes dans un verre métallique de part et d'autre de la transition vitreuse. La spectroscopie Mössbauer permet la mesure directe des mouvements vibrationnel et diffusionnel. L'augmentation de l'amplitude des vibrations atomiques dépend de la température de la même façon que l'augmentation de volume marquant la transition vitreuse : les deux processus sont donc gouvernés par le même mécanisme. Le mouvement diffusionnel mesuré directement est en accord avec les mesures macroscopiques de la diffusion.

## Acknowledgements

Many people have helped me to prepare this theses. It is a pleasure to acknowledge the support and friendship of my theses supervisor, John Ström-Olsen. His advice was very helpful, and discussions with him clarified many aspects of the physics involved. His help in proofreading was extremely valuable. I wish to thank Zaven Altounian for his critical advice and attention to important detail.

Parts of the experimental work, in particular the Mössbauer experiments, were carried out together with Dominic Ryan. Dominic taught me about experimental techniques, and he also took part in proofreading the thesis. Mark Sutton gave me access to his x-ray diffractometer and showed me the most appropriate way of using it. Through him I had access to software that was important for the data analysis. Milton From shared his experience in high precision x-ray diffraction with me, and it was his program that I used for the calculation of the structure factors.

John Kitching prepared several samples, and made many of DSC measurements which are included in this thesis.

Frank van Gils helped me in many cases through his technical skills, and working with him was very enjoyable. John Egyed and Michel Champagne did the necessary machining, including the manufacture of the parts for the Mössbauer furnace.

During my stay at McGill I profited from the friendship and many discussions with Christopher Roland, Reinhart Richter, Dave Baxter, Steve Brauer, Andrew Dawson, Ian Graham, Jacques Mainville (who translated the abstract) and many others.

I received financial support through a stipend from the Evangelisches Studienwerk e.V., West Germany, throughout my years at university. Without this support, I could not have studied in the same way.

From the Faculty of Graduate Studies at McGill University I received an Alexander McFee Fellowship and a McGill Major Award. The government of Quebec supported me by waiving the foreign student differential fees.

# Contents

<b>Abstract</b>	<b>i</b>
<b>Résumé</b>	<b>ii</b>
<b>Acknowledgements</b>	<b>iii</b>
<b>Table of Contents</b>	<b>iii</b>
<b>List of Figures</b>	<b>vi</b>
<b>List of Tables</b>	<b>viii</b>
<b>1 Introduction</b>	<b>1</b>
<b>2 Experimental Methods</b>	<b>12</b>
2.1 Preparation of the Samples . . . . .	12
2.2 Differential Scanning Calorimetry (DSC) . . . . .	14
2.3 Sample Annealing . . . . .	17
2.4 Density Measurements . . . . .	17
2.4.1 Measurement of the Room Temperature Density . . . . .	17
2.4.2 Thermal Expansion Measurement . . . . .	18
2.5 High Precision X-Ray Diffraction Measurements . . . . .	21
2.5.1 The Diffractometer . . . . .	22
2.5.2 Determination of the Structure Factor and the Radial Distribution Function from Measured Scattering Intensities . . . . .	26
2.6 Mössbauer Spectroscopy . . . . .	30
2.6.1 The Recoil-Free Fraction . . . . .	31
2.6.2 The Center Shift . . . . .	32
2.6.3 The Quadrupole Splitting . . . . .	32
2.6.4 System Configuration . . . . .	34
2.6.5 Room Temperature Measurements . . . . .	35
2.6.6 Mössbauer Furnace and High Temperature Measurements . . . . .	35
2.6.7 Data Fitting Procedures . . . . .	41
<b>3 Structural Relaxation</b>	<b>48</b>

3.1	Introductory Remarks . . . . .	48
3.2	Calorimetry . . . . .	49
3.2.1	Crystallization and Glass Transition . . . . .	51
3.2.2	Irreversible Relaxation . . . . .	55
3.2.3	Reversible Relaxation . . . . .	59
3.2.4	Summary of the DSC Results . . . . .	68
3.3	X-Ray Diffraction . . . . .	69
3.3.1	The Data . . . . .	70
3.3.2	Method of Analysis . . . . .	77
3.3.3	Results . . . . .	85
3.4	Mössbauer Spectroscopy . . . . .	93
3.4.1	The Data . . . . .	94
3.4.2	Discussion . . . . .	97
3.5	Summary . . . . .	103
<b>4</b>	<b>Mössbauer Spectroscopy Measurement of the Glass Transition</b>	<b>109</b>
4.1	Introduction . . . . .	109
4.2	The Spectra . . . . .	116
4.3	Procedure for Fitting the Spectra . . . . .	120
4.4	Data Analysis . . . . .	122
4.4.1	The Recoil-Free Fraction . . . . .	122
4.4.2	The Center Shift . . . . .	130
4.4.3	The Quadrupole Splitting . . . . .	132
4.4.4	The Linewidth . . . . .	134
4.5	Discussion . . . . .	136
<b>5</b>	<b>Conclusion</b>	<b>140</b>
	<b>References</b>	<b>144</b>

# List of Figures

1.1	The structure factor of four states of matter. . . . .	2
2.1	Schematic diagram of a Perkin-Elmer DSC-2c differential scanning calorimeter. . . . .	15
2.2	Typical DSC data for reversible relaxation. . . . .	16
2.3	The thermal expansion of lead measured with a dilatometer cell. . . . .	21
2.4	Schematic diagram of the diffractometer. . . . .	23
2.5	Effect of the sample position on the scattered intensity. . . . .	25
2.6	Schematic cross section of the Mössbauer furnace. . . . .	36
2.7	Photograph of the Mössbauer furnace (front view). . . . .	37
2.8	Photograph of the Mössbauer furnace (rear view). . . . .	38
2.9	Photograph of the disassembled Mössbauer furnace (front view). . . . .	39
2.10	Resonant absorption by the beryllium windows of the Mössbauer furnace. . . . .	40
2.11	Mössbauer spectrum of an as-quenched $\text{Pd}_{40}\text{Ni}_{40}\text{P}_{20}$ sample. . . . .	42
2.12	The quadrupole splitting distributions obtained by three fitting methods. . . . .	45
2.13	The residual error in fitting the Mössbauer spectra. . . . .	47
3.1	Schematic diagram of the dependence of the enthalpy and the specific heat on the thermal history. . . . .	50
3.2	DSC trace of the glass transition and crystallization in $\text{Pd}_{40}\text{Ni}_{40}\text{P}_{20}$ . . . . .	52
3.3	Heating rate dependence of various processes in $\text{Pd}_{40}\text{Ni}_{40}\text{P}_{20}$ . . . . .	54
3.4	Heat flow during irreversible and reversible structural relaxation in $\text{Pd}_{40}\text{Ni}_{40}\text{P}_{20}$ . . . . .	56
3.5	Irreversible and reversible relaxation enthalpies as a function of quench rate for $\text{Fe}_{82.5}\text{B}_{17.5}$ . . . . .	57
3.6	Dependence of irreversible relaxation on the method of amorphization. . . . .	58
3.7	Reversible enthalpy change as a function of $T_a$ and $t_a$ . . . . .	62
3.8	Measured diffusion coefficients in metal-metalloid amorphous alloys. . . . .	64
3.9	Reversible relaxation in metal-metalloid and binary metal-metal glasses. . . . .	65
3.10	Composition dependence of reversible relaxation in ternary metal-metal glasses. . . . .	67
3.11	Structure factor of $\text{Pd}_{40}\text{Ni}_{40}\text{P}_{20}$ . . . . .	70
3.12	Radial distribution function of $\text{Pd}_{40}\text{Ni}_{40}\text{P}_{20}$ . . . . .	71

3.13	Irreversible and reversible changes in $S(q)$ . . . . .	72
3.14	Reversibility of structural changes measured by x-ray diffraction. . . . .	73
3.15	Irreversible change of the interference function of $\text{Fe}_{40}\text{Ni}_{40}\text{P}_{14}\text{B}_6$ . . . . .	75
3.16	Irreversible change of the interference function of $\text{Pd}_{80}\text{Si}_{20}$ . . . . .	75
3.17	Irreversible changes of the distribution of the scattered intensity from $\text{Pd}_{82}\text{Si}_{18}$ . . . . .	76
3.18	Irreversible change of the interference function of $\text{Cu}_{57}\text{Zr}_{43}$ . . . . .	77
3.19	Fitting of the changes in the structure factor. . . . .	80
3.20	The radial distribution function of $\text{Pd}_{40}\text{Ni}_{40}\text{P}_{20}$ . . . . .	84
3.21	The fitting functions $\alpha_r(q)$ and $\beta_r(q)$ . . . . .	86
3.22	Changes in density and atomic order measured by x-ray diffraction. . . . .	89
3.23	Changes of the Mössbauer spectrum caused by structural relaxation. . . . .	95
3.24	The quadrupole splitting distribution of for three different annealing states. . . . .	96
3.25	Change of the Mössbauer fitting parameters. . . . .	98
3.26	Change of the Mössbauer fitting parameter $a$ . . . . .	99
3.27	Changes of density and atomic order scaled to the enthalpy changes. . . . .	104
3.28	Changes of Mössbauer fitting parameters scaled to the enthalpy changes. . . . .	105
4.1	The vibrational amplitude and the linewidth obtained from Mössbauer spectroscopy in $\text{HCl} \cdot 6\text{H}_2\text{O}$ . . . . .	114
4.2	The $f$ -factor of supercooled $\text{H}_3\text{PO}_4 \cdot \text{H}_2\text{O}$ and $\text{H}_3\text{PO}_4 \cdot 6\text{H}_2\text{O}$ . . . . .	115
4.3	Mössbauer spectra of $\text{Pd}_{40}\text{Ni}_{40}\text{P}_{20}$ at different temperatures. . . . .	118
4.4	The increase of the $f$ -factor during isothermal crystallization. . . . .	119
4.5	The temperature dependence of the correlation between the quadrupole splitting and the isomer shift. . . . .	121
4.6	Observation of the glass transition in $\text{Pd}_{40}\text{Ni}_{40}\text{P}_{20}$ by the change in $f$ -factor, thermal expansion and heat flow. . . . .	123
4.7	The root mean square amplitude of atomic vibration and the diffusional line broadening between room temperature to above $T_g$ . . . . .	125
4.8	The volume increase of amorphous $\text{Pd}_{40}\text{Ni}_{40}\text{P}_{20}$ as a function of temperature. . . . .	126
4.9	Comparison of the mean square vibrational displacement obtained from the $f$ -factor and thermal expansion. . . . .	128
4.10	The temperature dependence of the center shift $\delta$ . . . . .	130
4.11	The temperature dependence of the isomer shift $\delta_{ISO}$ . . . . .	131
4.12	The temperature dependence of the mean quadrupole splitting $\langle Q \rangle$ . . . . .	133

## List of Tables

2.1	Raw Materials. . . . .	13
2.2	Density measurements. . . . .	19
2.3	Operating conditions of the Mössbauer furnace. . . . .	43
3.1	The activation energies $E_a$ and the trial frequencies $\nu_0$ for various processes. . . . .	54
3.2	Comparison of the X-ray Diffraction Results with Enthalpy and Density Measurements. . . . .	88
4.1	Measurements of the glass transition by Mössbauer spectroscopy. . . .	112
4.2	Measurements of the glass transition by Mössbauer spectroscopy (cont.).	113

# Chapter 1

## Introduction

This thesis is about the structure of metallic glasses: how it is affected by thermal annealing and how it changes as one approaches the glass transition.

A glass is essentially a frozen liquid. If a liquid is cooled rapidly to far below the equilibrium melting point  $T_m$ , there is insufficient time and thermal energy for the crystal phase to nucleate and grow. An amorphous solid, or glass, is thus formed. A glass retains a static atomic structure very similar to that of a liquid (see Figure 1.1), but shows many macroscopic properties (e.g. elastic constants) like those of a normal crystalline solid. The rate of cooling needed to form an amorphous solid depends on the system. Silicates form glasses even at very slow cooling rates (degrees per hour), and indeed are hard to crystallize. Metals on the other hand only form glasses at high cooling rates ( $\approx 10^6$  K/s or greater may be necessary) and usually have to be held several hundred degrees below  $T_m$  to prevent crystallization on laboratory time scales.

When the temperature of a glass is raised several phenomena occur. As in a crystalline solid there is the usual thermal expansion, which takes place at the speed of sound. But there are additional changes of the structure, as may be best understood by first considering the behavior of a liquid, which, unlike a glass, can sample all of its equivalent configurations over typical measurement times and so is in internal thermodynamic equilibrium. As the temperature is changed the average

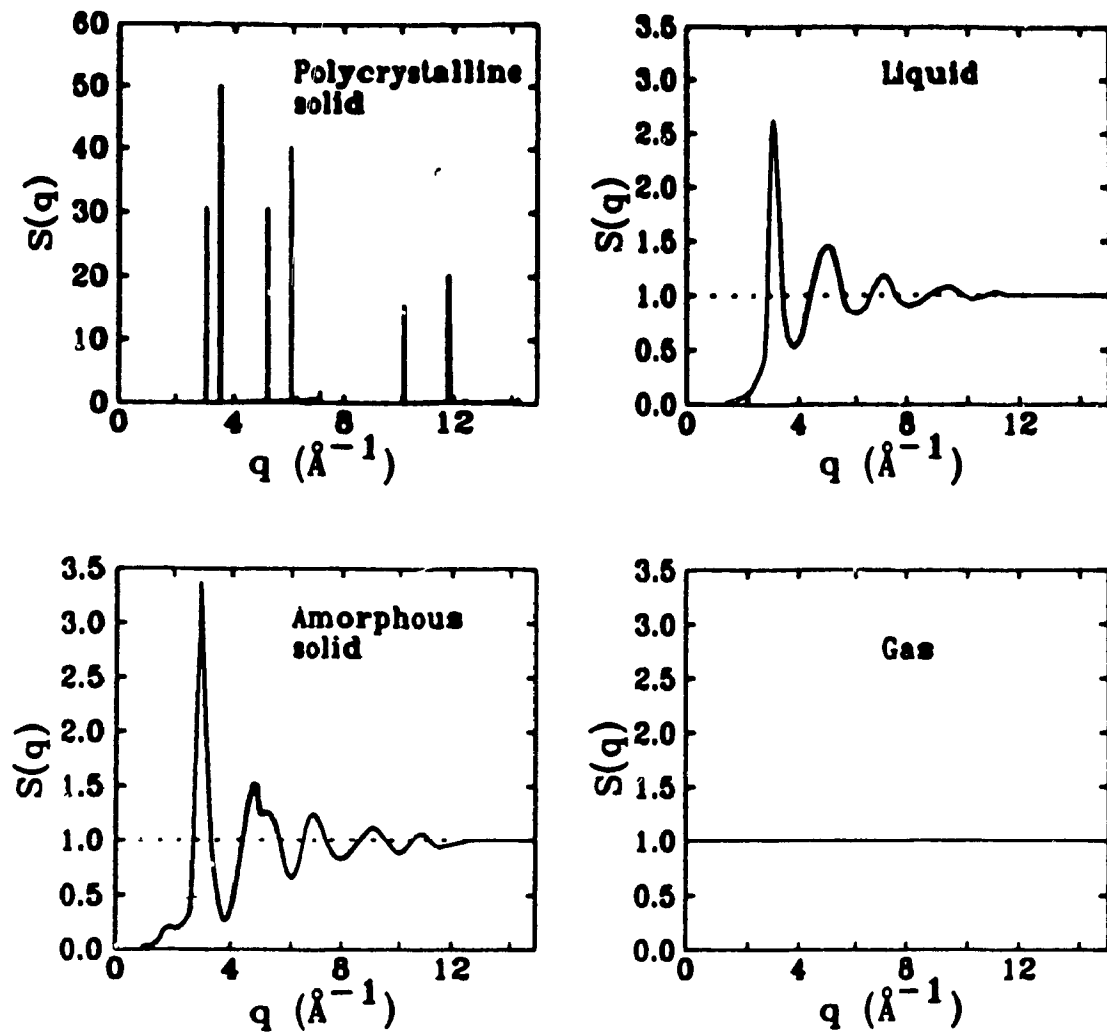


Figure 1.1: The structure factor of four states of matter. The structure factor,  $S(q)$ , is the Fourier transform of the radial distribution of the atoms (see Section 2.5.2). Diagram from [1].

equilibrium structure of the liquid changes also. The most prominent trend is the damping out of oscillations in the pair distribution function with increasing temperature (Huijben and van der Lugt, 1976 [2] and Etherington *et al.*, 1984 [3]). Similar changes would also occur in glasses if the atoms could move freely because, like the liquid, the glass has different states of lowest energy at different temperatures. In the glass, however, transformation between these configurations is impeded by the same mechanism that prevents crystallization. In consequence the changes occur very slowly and look more like a relaxation of the structure. In fact the glass may never reach the lowest local minimum of energy.

Traditionally this "structural relaxation" has been divided into irreversible and reversible contributions. Irreversible structural relaxation refers to the changes which occur when the glass is first heated after the rapid quench from the melt, so that the original unrelaxed state can only be restored by repeating the melt and quench cycle. Reversible structural relaxation refers to the adjustments of the structure of the glass which occur as the temperature of the glass is cycled below the glass transition (see below) and is thus reversible in a practical sense. In order for a relaxation process to qualify as reversible all the observables of the material have to be recovered within experimental error.

As the temperature is further raised, increasing thermal activation ensures that these processes occur more and more rapidly until eventually a point is reached where they occur at such a rate that the material begins to flow. This point is called the glass transition temperature,  $T_g$ , beyond which the material actually becomes a liquid (though, since in most cases  $T_g < T_m$ , the liquid is metastable and so transforms into the crystalline phase).

Historically the effects of structural relaxation in metallic glasses, especially reversible relaxation, were first seen through their influence on magnetic properties, most notably the Curie temperature (Egami 1978 [4]), because of the technical importance of ferromagnetic metallic glasses. A great deal of research has since been carried out on structural relaxation, mostly through measurement of its effect on

macroscopic properties. The following list, through not exhaustive, gives an idea of the range of parameters examined: atomic diffusivity (Chen 1978, [5]), viscosity (Taub and Spaepen, 1980 [6]), Young's modulus (Kursmovic and Scott, 1980 [7]), specific heat (Chen, 1981 [8]), superconducting transition temperature (Anderson *et al.*, 1982 [9]), internal friction (Morito and Egami, 1983 [10]), density and length (Cahn *et al.*, 1984 [11]), magnetization (O'Handley *et al.*, 1984 [12]), electrical resistivity (Balanzat *et al.*, 1980 [13]), magnetic aftereffect (Guo *et al.*, 1985 [14]), shear modulus (Dietz and Stanglmeier, 1987 [15]) and low temperature thermal conductivity (Herlach *et al.*, 1987 [16]). More references may be found in the articles cited, and in the reviews by Egami [4,17,18] and Gibbs and Hygate [19].

The question now arises: what has been learned about structural relaxation from these studies? Firstly the activation energies – *i.e.* the energy barriers which the atoms have to overcome in order for a structural change to occur and control the kinetics of structural relaxation – have been well determined from the time and temperature dependence of the physical parameters, and the results are fairly independent of the parameter examined. The processes occur over a wide temperature range, which indicates that the activation energies are also widely spread (see *e.g.* [8,20]). Secondly it has been found that many changes of physical properties correlate with each other: for example the Young's modulus increases as the density increases (Chen, 1978 [21]); the Curie temperature increases as the internal friction decreases (Morito and Egami, 1983 [10]); the density and hardness increase as the fracture toughness and the resistivity decreases (Hunger *et al.*, 1984 [22]). This suggests that some universal behavior governs relaxation of the glass.

Several attempts have been made to understand structural relaxation in terms of underlying microscopic processes. These have followed one or both of two theories. The first is the free volume theory (Turnbull and Cohen, 1960 [23]) which describes the evolution of the glass in the spirit of the role of defects in crystals. The free volume of an atom is "that part of its nearest neighbor cage in which the atom can move around without an energy change" (Spaepen, 1976 [24]) and is

therefore a measure of the difference between the actual atomic packing and some ideal. This model can explain the temperature dependence of the viscosity around  $T_g$  ([24] and the increase of the elastic moduli [21] and viscosity upon isothermal annealing [6,25-27], because thermal annealing reduces the amount of free volume of a rapidly quenched sample [28] (the sample becomes denser), so making it harder for atoms to move about. Although the free volume theory has met with some success, its limitation is that it describes the state of the glass by a single parameter, and cannot take into account changes of the structure of the glass other than density changes. A second model, introduced by Egami (Egami, 1978 and 1986 [4,18]), is more general in this respect. It stresses the distinction between the topological short range order (TSRO) and the chemical short range order (CSRO) in multi-component glasses. TSRO refers to the spatial arrangement of the atoms without considering the different atomic species, and includes changes in the free volume. CSRO indicates the nature of the chemical ordering between the atoms for a given spatial arrangement, and changes in it may be compared to the order-disorder transition in certain crystals, like  $\text{Cu}_3\text{Au}$ . Since then many authors have attributed reversible structural relaxation at low temperature (*i.e.* well below  $T_g$ ) to changes in CSRO alone [13,29,30].

However, these are hypotheses; to test them, direct measurements of the structure are needed. Very little has been discovered so far about the actual atomic processes occurring either during structural relaxation or during the approach to the glass transition. Indeed, relatively little can be learned from macroscopic parameters about the exact nature of the microscopic processes, since there is rarely a one-to-one correspondence between changes on a macroscopic and a microscopic level. For example, how can one relate a one percent change in resistance to a particular atomic displacement?

Two obvious techniques to obtain information about local atomic processes are diffraction (x-ray or neutron) and Mössbauer spectroscopy. Diffraction results from the interference between the waves scattered by the atoms, from which the radial

distribution of the atoms may be inferred. There have been relatively few diffraction studies of relaxation in metallic glasses, because of the difficulties involved in the measurements: the range of different local environments in the amorphous solid is much larger than the changes caused by structural relaxation and high precision is required to resolve them. In fact until the present work there have been no observations of reversible changes of radial distribution function reported, only of irreversible changes. As examples of the latter, Egami measured irreversible changes in the structure factor in  $\text{Fe}_{40}\text{Ni}_{40}\text{P}_{14}\text{B}_6$  by energy dispersive x-ray diffraction [31], and Waseda and Egami reported similar measurements by conventional x-ray diffraction on  $\text{Pd}_{80}\text{Si}_{20}$  [32]. They observed changes in the short range order. Specifically, during irreversible structural relaxation the peaks in the radial distribution of the atoms are enhanced and the correlation of the atomic positions increases for atoms that are several interatomic spacings apart, while the nearest neighbor distance between the atoms is nearly unchanged. Similar results were found by Mizoguchi *et al.* [33] on  $\text{Mg}_{70}\text{Zn}_{30}$ . Conversely, Chason *et al.* [34] interpreted the results of their measurements on  $\text{Pd}_{82}\text{Si}_{18}$  in terms of density changes only. Schaal *et al.* [35] measured structural relaxation of  $\text{Pd}_{52}\text{Ni}_{32}\text{P}_{16}$  by neutron diffraction and the results were similar to those obtained by x-ray scattering.

Complementary to these conventional diffraction studies, small angle x-ray or neutron diffraction experiments have been reported by Wu *et al.* [36], Schild *et al.* [37], Yavari *et al.* [38], Lamparter *et al.* [39] and others. These experiments probe the structure on longer length scales. Compositional inhomogeneities rather than density fluctuations give rise to most of the low angle scattering. Long range fluctuations seem to be favored by annealing [36], and small inhomogeneities grow in size [39]. These measurements are technically difficult and very much influenced by the sample geometry, impurities, nucleation and crystallization, which are unrelated to the structure of the glass. Some studies report that irreversible relaxation increases the scattering at small angles, while others report a decrease. But it appears that fluctuations exist in the amorphous structure with typical length scales between 10

and  $100 \text{ \AA}^1$  which can be influenced by thermal annealing [39].

Several studies of the effects of irreversible structural relaxation were also made by measuring the extended x-ray absorption fine structure (EXAFS), which, like diffraction, provides information about the radial distribution of the atoms. Unfortunately the deconvolution of the experimental data is not straightforward. There is a large uncertainty in the deconvolution of the signal at low scattering vectors, and therefore the long range correlations in the structure cannot be determined. The advantage of this method is that the scattering with high momentum transfer can be measured, thus the distribution of the nearest neighbor atoms is much better resolved than in conventional diffraction. The most conclusive result of these measurements is a sharpening of the nearest neighbor atomic shells, which was seen by Yu *et al.* in  $\text{Fe}_{79}\text{Si}_{11}\text{B}_{10}$  [40], and by Cocco *et al.* in  $\text{Pd}_{76}\text{B}_{24}$  [41].

Apart from the fact that these studies have only measured irreversible relaxation, an analysis of the changes in the radial distribution function in terms of well defined local structural changes is still missing. All the data have been analyzed so far assuming just a single process (density changes or some appropriate sharpening of the radial distribution function), even though the macroscopic measurements referred to above indicate several types of processes.

So far we have only discussed techniques that access the radial distribution of the atoms. A different type of information about the local atomic environment may be derived from Mössbauer spectroscopy, which measures the hyperfine splitting of the nuclear levels that undergo a transition (usually the 14.4 keV transition in  $^{57}\text{Fe}$ ). Takahara *et al.* [42] recently measured irreversible structural relaxation in a magnetic metallic glass, and observed a sharpening in the distribution of local magnetic fields, while the average magnetic field did not change. Although this indicates a more homogeneous distribution of local sites, no direct information on

---

<sup>1</sup>The non-SI (système international) units employed in this thesis are:

Angström:  $1 \text{ \AA} = 10^{-10} \text{ m}$ , and

Electron-Volt:  $1 \text{ eV} = 1.60219 \times 10^{-19} \text{ J}$ .

the structure can be obtained from this, because the details of the magnetic exchange interaction are unknown. The situation is different in non-magnetic glasses because the degeneracy of the nuclear levels is only lifted by the electric field gradient, which depends on the symmetry of the local atomic distribution [43,44]. (A deviation from a locally isotropic environment will lead to an electric field gradient at the site of the nucleus, which splits the nuclear levels.) This splitting can only be measured with sufficient accuracy if no additional magnetic splitting of the lines is present, so that it is essential to choose a non-magnetic glass to determine the evolution of the local symmetry directly. Until the present such an experiment has not been performed. This work represents the first experiment of its kind.

Thus previous microstructural studies have left many questions unanswered, and further experiments are required. For example it is not known how macroscopic density changes relate to changes in the radial distribution of the atoms, or whether the widely different activation energies observed correspond to systematically different atomic processes. There has been no study of the dependence of the angular distribution of the atoms on structural relaxation, and no investigation of reversible structural relaxation by either diffraction measurements or Mössbauer spectroscopy. No direct measurement of atomic motion at and above the glass transition exists. No connection has been made between the microscopic models of structural relaxation based on macroscopic measurements, and direct measurements of structural relaxation. Finally, no microstructural observation has been made of the reversible processes. This thesis set out to answer these questions.

In order to see the effects of structural relaxation most clearly and dramatically, we looked for a glass of exceptional stability, so that it may sustain extensive annealing without crystallization, thereby maximizing the effects of relaxation. Such a glass is  $\text{Pd}_{40}\text{Ni}_{40}\text{P}_{20}$ , and most measurements have been made on this glass. In general, high cooling rates are required for making metallic glasses, and only a few may be heated to  $T_g$  without crystallizing.  $\text{Pd}_{40}\text{Ni}_{40}\text{P}_{20}$  is an exception in so far as it is stable above  $T_g$  for a considerable time. Chen first measured the glass transition

at about 570 K (Chen, 1976 [45]) and found that the ratio of the glass transition and the melting point, 886 K [46], is high for a metallic glass, which explains why the supercooled liquid is so stable. Its stability has been used by Drehman *et al.* to prepare bulk samples by slow cooling in vacuum [47], and by Kui *et al.* to produce fully amorphous bulk samples by slowly cooling the material in boron oxide [48].

If one were to pick the macroscopic property which most directly reflects the state of the glass, the choice would certainly be the enthalpy (or changes in the enthalpy) for a number of reasons. First, enthalpy changes relate very closely to changes in atomic order and so may be used in a simple way to provide a measure for structural changes in a system-independent way (unlike, say, Curie temperature or electrical resistivity). Enthalpy changes can be measured quite simply by scanning calorimetry, which measures the heat flow into and out of the sample upon heating, as will be discussed in detail below. In addition, enthalpy changes are recorded as a function of temperature and time, which allows one to determine the activation energies of structural changes. For reversible processes the energy jump for a single process can be estimated. In a thermogram, the overall appearance of irreversible relaxation and reversible relaxation at high and low temperatures are quite distinct, as will be discussed in detail at the beginning of Chapter 3. For these reasons enthalpy measurements used as a benchmark for structural relaxation, and also served as the starting point for *direct* measurements of the local structural changes. X-ray diffraction, sensitive to the radial distribution of the atoms, and Mössbauer spectroscopy, giving information on to the local site symmetry, were used as complementary probes of the local atomic structure. These results will be related to and scaled with the calorimetric data.

To complement the studies mentioned above on a single system, a survey study of enthalpy changes in several metallic glass systems was made in order to examine the role composition plays in determining the magnitude of structural relaxation and hence, in particular, whether changes in CSRO play a role.

The first measurement of the glass transition in a metallic glass by Mössbauer

spectroscopy is reported in this thesis. Mössbauer spectroscopy has been applied quite commonly to measure how the motion of molecules or ions changes at the glass transition in non-metallic glasses, because it detects both the vibrational motion and the diffusional motion of atoms on the time scale of a tenth of a microsecond, and thus provides unique information about the atomic dynamics.

We have made the same measurement on a metallic glass out of a two-fold interest. First, we are interested in the microscopic dynamics of amorphous  $\text{Pd}_{40}\text{Ni}_{40}\text{P}_{20}$  where we study the result of the atomic motion, *i.e.* we want to know *how* the structural changes occur. Secondly, metallic glasses are, in contrast to conventional glasses, structurally much less complex: there is less residual atomic ordering since metallic ions can be considered, to a good approximation, as spherical units, and the metallic bonding as isotropic (as can be seen from the fact that most metals have a close packed structure, and also that hard sphere models provide a good description of the structure of a metallic glass). Of course this is also why they crystallize so readily, which in most cases prevents prolonged measurements at high temperatures. Since metallic glasses are so simple, they are also the best model system to study the glass transition, as is shown by the popularity of molecular dynamics simulation of the glass transition in metallic glasses (see *e.g.* [49-52]).

The collection of a Mössbauer spectrum takes in general a time of the order of one day, so that for most glasses the onset crystallization would interfere with the measurement of the glass transition. Once more we have made use of the exceptional stability of  $\text{Pd}_{40}\text{Ni}_{40}\text{P}_{20}$ , and in addition the experimental technique was optimized to allow the rapid collection of spectra of good quality, which has made the experiment possible. As a reference for these data of the microscopic dynamics, macroscopic measurements of the volume expansion of the glass and the specific heat at the glass transition have been made.

In the following Chapter, details of the sample preparation and the experimental techniques are given. In Chapter 3, the results of the measurements of structural relaxation are first reported and discussed separately for calorimetry, x-ray diffrac-

tion and Mössbauer spectroscopy, and then compared and discussed together in the last section of that Chapter. Chapter 4 contains the measurements of the glass transition by Mössbauer spectroscopy. The findings of the thesis are summarized in Chapter 5.

## Chapter 2

# Experimental Methods

### 2.1 Preparation of the Samples

Experiments were performed on melt-spun ribbons of alloys of the composition  $\text{Pd}_{40}\text{Ni}_{40}\text{P}_{20}$  and  $(\text{M}^a_x\text{M}^b_{1-x})_{33}\text{Zr}_{66}$  ( $\text{M}^a, \text{M}^b = \text{Fe}, \text{Co}, \text{Ni}, \text{Cu}$ ). The ingots for melt-spinning were prepared from the raw materials listed in Table 2.1.

Ingots for melt-spinning were prepared in an arc-furnace under titanium gettered prepurified argon. The copper and cobalt ingots were etched with diluted  $\text{HNO}_3$  to remove surface contaminants. The solid ingots were washed in ethanol before alloying. Ingots of the composition  $\text{Pd}_{40}\text{Ni}_{40}\text{P}_{20}$  were made by first melting the  $\text{Ni}_2\text{P}$  powder into solid pellets, and then alloying them appropriate amounts of palladium. The evaporation of phosphorus was minimized by keeping the hot handling time short, typically a few seconds. It was verified by weighing the material before and after alloying that less than 1 at. % phosphorus was lost. (Usually the phosphorus condensed onto the cold copper base of the arc-melter.) 5 mg  $^{57}\text{Fe}$  (which corresponds to 0.5 at. %) was added to the  $\text{Pd}_{40}\text{Ni}_{40}\text{P}_{20}$  ingots for the samples to be used in the Mössbauer experiments. Adding the  $^{57}\text{Fe}$  to the already prepared Pd-Ni-P minimized the loss upon alloying.

Both wide and narrow ribbon samples were produced by single roller melt

Table 2.1: Raw Materials.

	Supplier	Form	Purity
Pd	Alfa Products	powder -20mesh	m99.95 %
Pd	Engelhard Corporation	bar	99.9 %
Ni <sub>2</sub> P	Alfa Products	powder -100mesh	99.5 %
<sup>57</sup> Fe	E.I. DuPont de Nemours & Co.	powder	93.31 % enriched
Zr	Alfa Products	crystal bar	m99.95 %
Fe	Alfa Products	lump random	m99.95 %
Ni	Alfa Products	shot	m99.9+ %
Cu	Alfa Products	shot	99.9 %
Co	Alfa Products	pieces	99.9+ %

quenching using a copper wheel; a tangential velocity of about 30 m/s gave good results. The alloys were melted by r.f. induction in a quartz crucible under 17 kPa pressure of helium. The melts were ejected out of the crucible under an argon pressure of 100 kPa released by a manually operated solenoid valve. Narrow ribbons were obtained using a crucible with a small circular orifice (typically 0.4 mm in diameter); the resulting ribbons were 1 to 2 mm wide and about 20  $\mu$ m thick. Some experiments required wider ribbons, which were cast from a crucible with a slot. The tube was made by mounting a quartz tube (20.4 mm outside diameter, 17.8 mm inside diameter) horizontally and then melting it from above at approximately 4 cm from the end with a propane-oxygen torch. The surface slowly collapsed and formed, if done carefully, a horizontal and straight edge. Then the tube was turned and the opposite side was melted until a narrow slot was formed, approximately 0.3 mm wide. The crucible so made was then cut on a diamond wheel at the neck of the slot to ensure a good flow of the liquid. Suitable ingot weights for melt-spinning by this method are 2 to 3 g, and the ribbons obtained were 11 mm wide and 30  $\mu$ m thick, and of good quality.

That the samples were amorphous was checked by conventional x-ray diffrac-

tion before and after all measurements. Crystalline contaminants down to a level of about 2% can be detected by this method. Data were taken only from samples that were amorphous according to this criterion. This is important, since measurements on  $(\text{Fe}_x\text{Ni}_{1-x})_{80}\text{B}_{10}\text{Si}_{10}$  show that crystallization at the surface of the sample (the part of the sample most susceptible to deterioration) strongly affects structural relaxation [20,53].

## 2.2 Differential Scanning Calorimetry (DSC)

The enthalpy flow into and out of the sample was measured with a Perkin Elmer Differential Scanning Calorimeter DSC-2c, shown schematically in Figure 2.1. The calorimeter has two holders which are resistively heated and a resistance thermometer is attached to each holder. One of the holders contains the sample, while the other contains a reference sample. The two holders are programmed to be heated or cooled at a specific rate, and the difference in electric power required to keep the two holders at the same temperature is recorded as a function of temperature. Such a measurement is a sensitive and easy-to-use method to detect and monitor any heat flow into or out of the sample. In this study it has been used to characterize crystallization, the glass transition, and reversible and irreversible structural relaxation.

To protect the sample from oxidation at high temperatures the calorimeter was operated under a flow of high purity argon, which according to suppliers specifications contained less than 3 ppm  $\text{O}_2$  and 5 ppm  $\text{H}_2\text{O}$ . The gas was passed through a drying agent before entering the sample space. Many of the measurements were done close to the noise level of the instrument; this required extra care. The sample mass was typically 50 mg and the instrument was always given time to stabilize before the measurements by heating the sample cell to 800 K or above. Since the thermal processes that are of interest here occur only once upon heating the sample, they can be resolved more clearly by immediately measuring the same sample

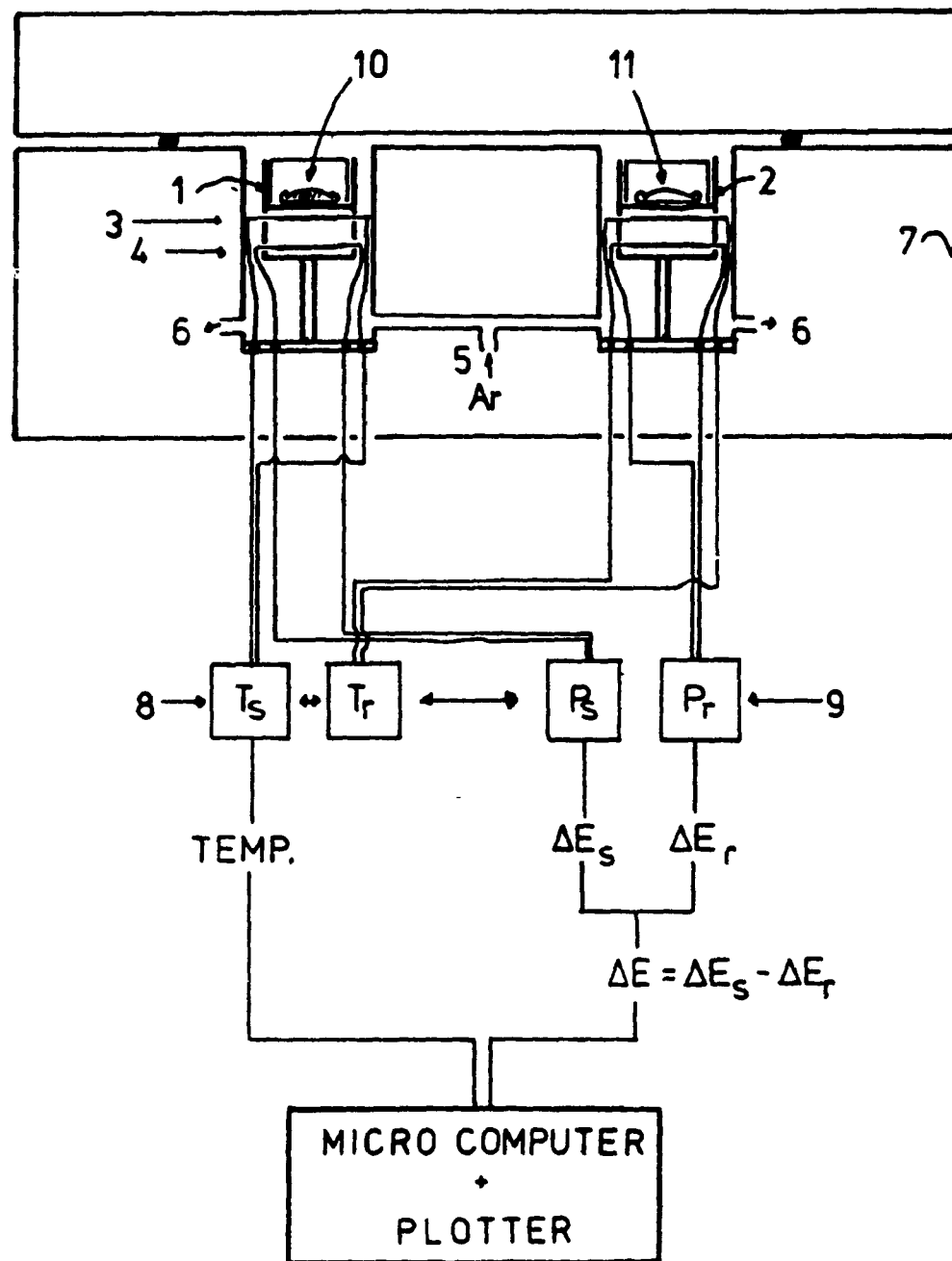


Figure 2.1: Schematic diagram of a Perkin-Elmer DSC-2c. Diagram from [54].

- |                            |   |
|----------------------------|---|
| 1 - sample holder          | 7 - aluminum body (heat sink)             |
| 2 - reference holder       | 8 - thermometers for sample and reference |
| 3 - resistance thermometer | 9 - power supplies for heaters            |
| 4 - heater                 | 10 - sample confined in aluminium pan     |
| 5 - argon inlet            | 11 - reference sample                     |
| 6 - argon outlet           |   |

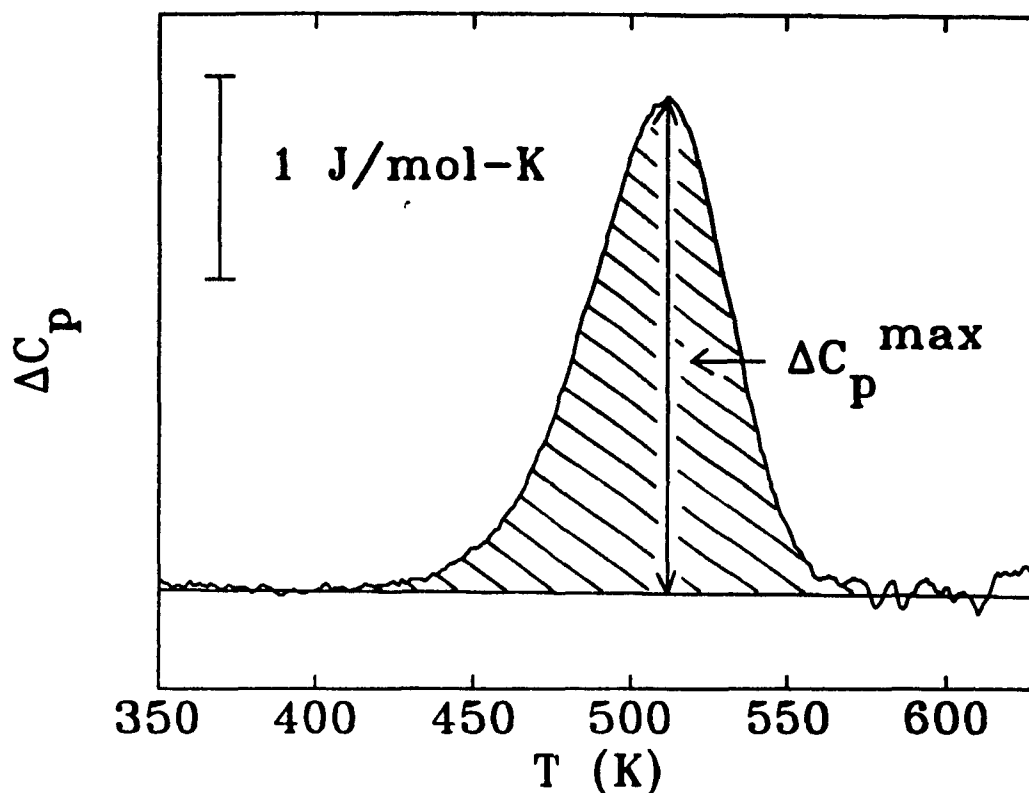


Figure 2.2: Typical DSC data for reversible relaxation. The linear background specific heat is interpolated. The maximum peak height  $\Delta C_p^{max}$  and the peak area, corresponding to the enthalpy change  $\Delta H$ , are determined with respect to it.

again. The resulting background scan is then subtracted from the first scan. This procedure directly eliminates the normal specific heat of the sample, resolves slight changes in the heat flow more clearly and reduces the effects of any instrumental drift.

The signals that were measured ranged between  $0.2$  and  $15 \text{ J mol}^{-1}\text{K}^{-1}$ . The noise level of the measurements with background subtraction was  $0.2 \text{ J mol}^{-1}\text{K}^{-1}$ . In some cases the peak areas (total enthalpy change) rather than the difference in heat flow was taken as a measure for structural relaxation effects. A typical data curve is shown in Figure 2.2, which also indicates how the peak heights and the peak areas have been determined. The exact procedure adopted to obtain the thermogram is described in Section 3.2.3. Fluctuations of the instrument appear, in spite of the precautions taken, as a curved baseline in the data. Also expansion and movement

of the sample in the holder can lead to sudden jumps in the signal.

For the determination of the peak height of the reversible endotherm it is possible to interpolate the noise to reduce the error to about  $0.1 \text{ J mol}^{-1} \text{ K}^{-1}$ . This is approximately the standard deviation obtained from the scatter of the data obtained by repeated a measurement.

The calorimeter was programmed to perform various anneals, which were followed by automated measurement. This made the apparatus more efficient by allowing unmonitored overnight use.

## 2.3 Sample Annealing

Short-time annealing of small samples was done in the calorimeter, as described above. All other annealing was carried out in a conventional wire-wound resistance furnace under helium at 17 kPa. To keep the wide ribbons flat<sup>1</sup> the samples were held between aluminium plates during the heat treatment. The pressure exerted on the ribbon is very small, and does not lead to any anisotropy of the sample. All annealing in the resistance furnace was monitored by concurrently annealing a reference sample, cut from the same batch, which was afterwards analyzed by DSC.

## 2.4 Density Measurements

### 2.4.1 Measurement of the Room Temperature Density

The densities of some of the wide  $\text{Pd}_{40}\text{Ni}_{40}\text{P}_{20}$  ribbons was measured by Archimedes' method (see e.g. Pratten, 1981 [55]). The density of a body can be determined by measuring its weight  $W$  and in its apparent weight in a liquid  $W_l$ . Then the mass of the sample is  $m = gW$ , and the mass of displaced liquid is  $\Delta m = g(W - W_l)$ ,

---

<sup>1</sup> $\text{Pd}_{40}\text{Ni}_{40}\text{P}_{20}$  in the supercooled liquid state (above  $T_g$ ) is a very viscous liquid, and small pieces of ribbon will contract to little beads under the influence of surface tension within a few minutes.

and the density is given by:  $\rho = m/V = m\rho_l/\Delta m$ . Because of its optimal combination of high density and low surface tension, tetrabromoethane ( $C_2H_2Br_4$ , density  $\rho_l = 2.97 \text{ g/cm}^3$ ) was chosen for the working fluid. The sample dimensions were  $30 \times 11 \times 0.030 \text{ mm}^3$  and the weight was typically 70 mg. A servo-controlled microbalance, part of a Perkin-Elmer thermo-gravimetric analyzer (TGA-7), was used for the weighing. It was protected from air draft perturbations by a cardboard box. With this arrangement weights can be determined to within  $2 \mu\text{g}$ . Two measuring platforms, connected by an amorphous metal fiber of  $15 \mu\text{m}$  diameter, were suspended from the balance arm so that the lower platform was immersed in the liquid. The force on the suspension wire resulting from the surface tension at the interface is approximately given by:  $F = 2\pi r\sigma \cos \alpha$ , where  $r$  is the diameter of the wire,  $\sigma$  the surface tension and  $\alpha$  the angle of the meniscus of the liquid at the wire [56]. It represents a major source of experimental error: the value of  $\sigma$  for  $C_2H_2Br_4$  is  $0.050 \text{ N m}^{-1}$  (compared to  $0.073 \text{ N m}^{-1}$  for water) [57], which leads to a force equivalent to a mass of  $240 \mu\text{g}$  or less (depending on  $\alpha$ ). This is about ten times larger than the necessary precision. Hence the reproducibility of the surface tension, in particular of  $\alpha$ , is crucial for the success of the experiment. To improve the accuracy of the result all samples were measured several times in random order, which avoids systematic errors due to temperature and composition changes. The measured values are given in Table 2.2. The precision of each the measurement was about 0.12 %, and the expected error of the average values was 0.05 %. The largest density difference between samples is 0.22 %.

### 2.4.2 Thermal Expansion Measurement

The volume expansion of a  $Pd_{40}Ni_{40}P_{20}$  sample was measured using a commercial thermo-mechanical analyzer (Perkin-Elmer TMA-7). The TMA consists of a furnace, and a probe that may be lowered into the furnace. The probe measures the thermal expansion of a sample at constant heating rate. It can be adjusted so that it provides constant pressure or tension, according to the requirement of the specific

Table 2.2: Density measurements. The apparent mass difference,  $\Delta m$ , the mass,  $m$  and the relative density,  $\rho/\rho_1$ , for  $\text{Pd}_{40}\text{Ni}_{40}\text{P}_{20}$  in various annealing states (see Chapter 3) during irreversible relaxation. The experimental uncertainties  $\Delta\bar{\rho}$  have been calculated by dividing the experimental scatter by  $\sqrt{n-1}$ , where  $n$  is the number of measurements.

Sample State	$\Delta m$ ( $\mu\text{g}$ )	$m$ ( $\mu\text{g}$ )	$\rho/\rho_1$	$(\bar{\rho} \pm \Delta\bar{\rho})/\rho_1$
As-Made	21633	68644	3.1731	$3.1708 \pm 0.0022$
	21612	68630	3.1756	
	21676	68632	3.1663	
	21643	68704	3.1744	
	21712	68714	3.1648	
Partially Relaxed (Heated to 540 K)	25723	81604	3.1724	$3.1735 \pm 0.0009$
	25729	81627	3.1726	
	25707	81609	3.1746	
	25708	81690	3.1777	
	25751	81674	3.1717	
	25751	81684	3.1721	
Reference State	19830	63027	3.1784	$3.1742 \pm 0.0018$
	19827	63020	3.1785	
	19880	63008	3.1694	
	19870	63105	3.1759	
	19919	63116	3.1686	
	19875	63092	3.1744	
Reference State	24402	77596	3.1799	$3.1777 \pm 0.0017$
	24451	77643	3.1755	
	24462	77635	3.1737	
	24403	77688	3.1835	
	24471	77722	3.1761	

experiment. The probe is made out of quartz, which has a low thermal expansion coefficient, and its displacement is monitored by a linear variable differential transformer (LVDT), which is very sensitive to small displacements.

Here the TMA has been used in conjunction with a dilatometer cell. It is provided by the same company and fits into the TMA furnace. The dilatometer cell consists of a cylindrical barrel and a plunger, both made out of quartz. The plunger fits into the barrel and seals it. However, the plunger may move up and down and thus follows the thermal expansion of a sample placed inside the cell. Inside the furnace, the probe is placed on top of the plunger to detect the motion of the plunger as the sample is heated.

The inside diameter of the barrel is 7.1 mm, and the height of the sample space is 5 mm. The volume of the sample space is therefore 198 mm<sup>3</sup>. For the measurement this space is filled by the sample and a suitable medium to transfer the expansion of the sample onto the plunger. The ideal medium would be a liquid, however, no suitable liquid is available in the temperature for the range of our measurement (from 300 to 630 K). Instead we used an Al<sub>2</sub>O<sub>3</sub> powder, which flows easily and is inert. The cell has a small orifice at the side, which allows the barrel to be closed with the plunger without leaving any free space between the plunger and the filling medium. The thermal expansion of the Al<sub>2</sub>O<sub>3</sub> powder is measured and subtracted from the sample run.

Figure 2.3 shows a thermal expansion measurement on a 0.4 g bulk sample of lead. The solid line gives the density measured with the dilatometer cell, and the points are literature values [58,59]. This shows that the measurement of the thermal expansion of the lead below the melting point, 601 K, and the onset of the melting are detected reliably. However, the the dilatometer cell cannot follow the sudden expansion of the sample during melting as the Al<sub>2</sub>O<sub>3</sub> powder penetrates the sample, and the packing of the powder changes, this effect appearing as an additional signal. Thus the data cannot be used beyond the onset of melting.

To measure the thermal expansion of Pd<sub>40</sub>Ni<sub>40</sub>P<sub>20</sub> we used a bulk amorphous

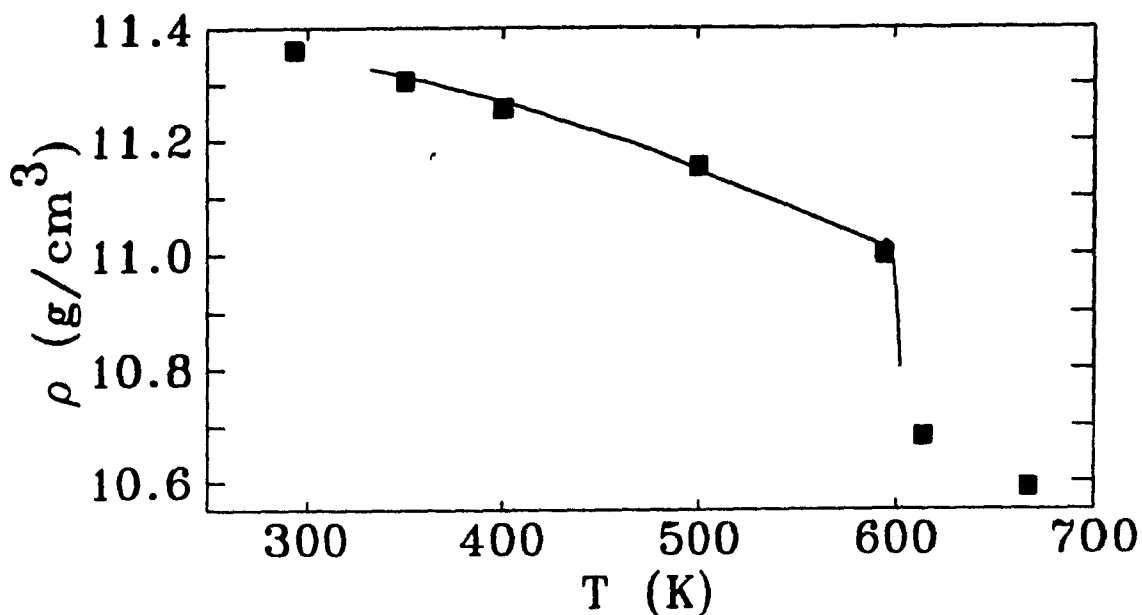


Figure 2.3: The thermal expansion of lead measured with a dilatometer cell. The points are literature values taken from [58,59].

sample that was made by cooling in  $B_2O_3$ .<sup>2</sup> The advantage of using a bulk sample is that it has a large mass compared to its dimensions, which increases the signal. The sample was cut to fit into the cell. The mass of the cut sample was 1.05 g, and its volume  $119 \text{ mm}^3$ . The data are shown in the Figures 4.6.b (thermal expansion coefficient) and 4.8 (volume change).

## 2.5 High Precision X-Ray Diffraction Measurements

The changes in the structure of the amorphous samples were measured using a diffractometer optimized for this specific purpose (Section 2.5.1). The method for calculating the structure factor,  $S(q)$ , which describes the influence of the geometrical arrangement of the atoms on the diffraction pattern, and the radial distri-

<sup>2</sup>This sample was kindly provided by D. Herlach, Institut für Raumsimulation, Köln, West Germany.

bution function  $\rho(r)$  from the experimentally observed scattering is described in Section 2.5.2.

### 2.5.1 The Diffractometer

The requirements for a diffractometer to measure the very small structural changes associated with structural relaxation are high precision combined with high signal intensity. The resolution of the instrument is much less important than in measurements on crystalline substances since in an amorphous alloy  $S(q)$  is rather broad and so, in consequence, are changes to it. To obtain such an instrument a diffractometer in the laboratory was modified to optimize its performance.

Figure 2.4 shows a schematic diagram of the diffractometer.  $\text{CuK}_\alpha$  ( $\lambda = 1.5418 \text{ \AA}$ ) radiation was used so that the first peak in the structure factor, the region of interest, was in an easily accessible regime (between  $26^\circ$  and  $60^\circ$ ). Furthermore, at this wavelength the sample is four times thicker than the absorption length, which makes several corrections discussed below small, while most of the signal still originated from the bulk of the sample rather than the surface. For the same reason the experiment was done in reflection mode. Graphite monochromator and analyzer crystals were chosen for the high x-ray reflectivity of their (002)-plane; the relatively low angular resolution of about  $0.3^\circ$  is sufficient since the width of the changes in  $S(q)$  is at least  $3^\circ$ , as will be shown later. The intensity was increased by a factor of about 7 by using a bent monochromator. It has a radius of curvature of 115 mm and focuses the beam onto the sample in the direction perpendicular to the scattering plane. The monochromator is used at the Bragg-angle for  $\text{CuK}_\alpha$  radiation,  $13.29^\circ$ , so that the focal length of the system is 250 mm. The beam intensity at the sample was optimized by choosing the distance between the source and the monochromator. In order to focus the beam over a short total distance the bent monochromator should be close to the center point between source and sample, while it has to be close to the source to collect a large solid angle of radiation. The effect of the focusing is shown by the vertical slit openings, 20 mm, at the monochromator and

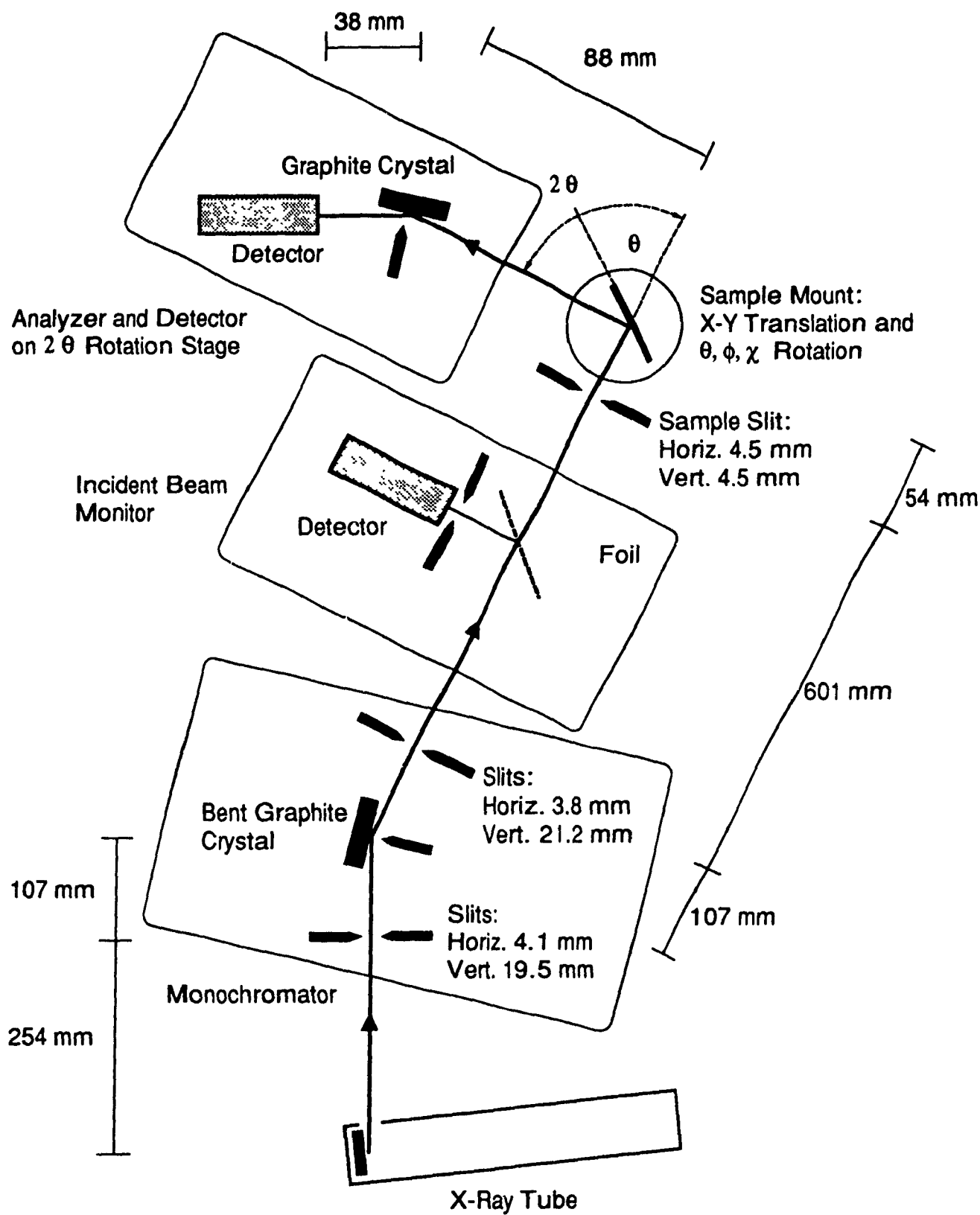


Figure 2.4: Schematic diagram of the diffractometer.

4.5 mm at the sample. The first two slits were set to cut approximately 10 % of the total intensity each; the sample slits were first set to touch the beam, and then set at 20  $\mu\text{m}$  away from it. To monitor fluctuations in the incident beam, a monitor was placed between monochromator and the sample. The monitor consisted of an  $\approx 6 \mu\text{m}$  thick Kapton<sup>TM</sup> foil, which was placed at 45° to the beam. The scattered photons were measured by a detector. The recorded intensity was used to normalize the signal, which was taken from an identical detector. A flat graphite crystal was used as an analyzer in front of the detector to ensure that only radiation originating from the sample could enter, so minimizing the contribution of air scattering. For the same reason the beam path between the x-ray tube and the sample slit and the path between the analyzer and the detector were completely enclosed. The angular resolution of the instrument measured at 0° was 0.45° FWHM. The count-rate at the maximum of the first scattering peak was typically 500 s<sup>-1</sup>.

The x-ray tube was operated at 1.6 kW. When first switched on, both the intensity and the direction of the beam fluctuated, but after waiting for about ten days, the tube stabilized and the angle of the centroid of the beam remained constant during the measurements to within 0.0017°. The distances between the x-ray source, the sample and the detector were made large so that the signal would be more sensitive to the diffraction-angles than to small displacements of the sample. In spite of this precaution reproducible sample mounting proved very important. Figure 2.5 shows the scattered intensity as a function of the position of the sample in the scattering volume (*i.e.* the overlap between the space illuminated by the source and the space seen by the detector). This curve allowed us to estimate that the accuracy necessary for the alignment of the sample surface with the goniometer axis is about 20  $\mu\text{m}$ . To achieve such precision an micrometer *x-y* translation stage was mounted on an adjustable goniometer head. By viewing the sample from the side with a telemicroscope and by rotating the the goniometer by 180° displacements between the sample and the axis of rotation can be measured and corrected to within 5  $\mu\text{m}$ . The beam spot at the sample was 4.5  $\times$  4.5 mm<sup>2</sup>. The sample dimensions were

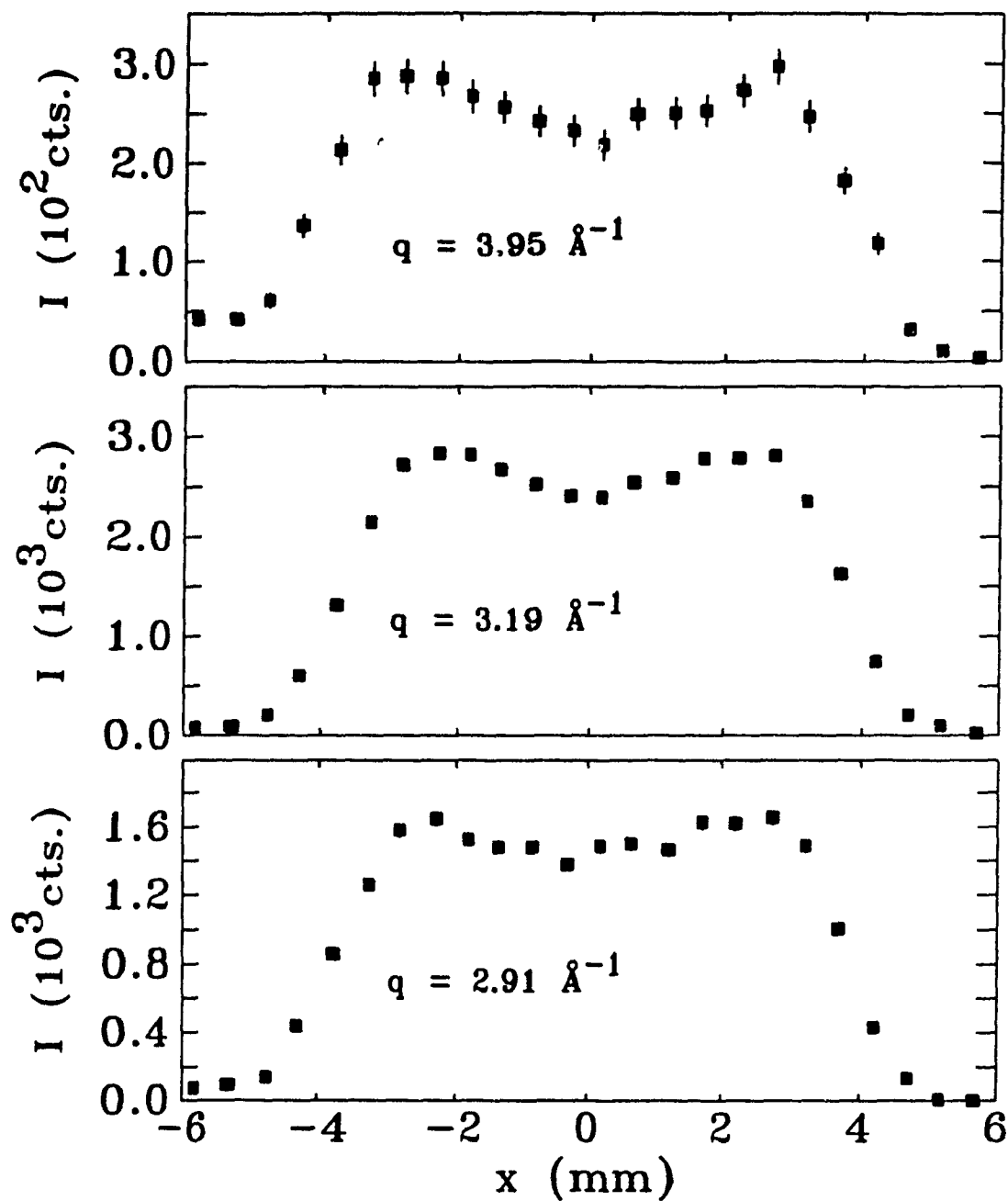


Figure 2.5: Effect of the sample position on the scattered intensity. The amorphous sample is moved in the direction perpendicular to  $\vec{q}$  through the scattering volume.  $x = 0$  mm is the position of the goniometer axis. The measurements were taken at the minimum ( $q = 3.95 \text{ \AA}^{-1}$ ), the maximum slope ( $q = 3.19 \text{ \AA}^{-1}$ ) and the maximum of  $S(q)$  ( $q = 2.91 \text{ \AA}^{-1}$ ).

$30 \times 11 \times 0.030 \text{ mm}^3$ . To hold the sample a similar device to the one employed by Chason *et al.* [34] was used, which consisted of a steel frame to hold the sample flat and an adjustable rod to maintain it under very small tension.

To reduce the effect of instrumental drifts each measurement consisted of about 20 subscans, each taking about 1 h, which were then added to form a single spectrum. The errors calculated from the variations between the subscans were close to those expected from the Poisson statistics.

The scattering vector  $q = 4\pi\lambda^{-1} \sin \theta$  was scanned from 1.8 to  $4.0 \text{ \AA}^{-1}$  in steps of  $0.04 \text{ \AA}^{-1}$ . To obtain the radial distribution function of the sample one measurement was made from 1.2 to  $7.4 \text{ \AA}^{-1}$ . The correction for air scattering was made using a background scan with no sample present.

## 2.5.2 Determination of the Structure Factor and the Radial Distribution Function from Measured Scattering Intensities

The information that one would like to obtain from x-ray diffraction is the radial distribution function (RDF) of the atoms,  $\rho(r)$ , as mentioned in the introduction.  $\rho(r)$  is the number density of the atoms at a distance  $r$  from a reference atom. What is most directly obtained from the measurements, however, is the structure factor  $S(q)$  which is related to  $\rho(r)$  by the relation (see *e.g.* [60]):

$$S(q) - 1 = \int_{r=0}^{\infty} 4\pi r^2 (\rho(r) - \rho_0) \frac{\sin(qr)}{qr} dr. \quad (2.1)$$

or its inverse:

$$2\pi^2 r (\rho(r) - \rho_0) = \int_{q=0}^{\infty} q (S(q) - 1) \sin(qr) dq. \quad (2.2)$$

$\rho_0$  is the average density.  $S(q)$  is a dimensionless quantity which describes the contribution to the elastically scattered radiation by the arrangement of the atoms. The elastic scattering from an individual atom is proportional to the atomic structure factor  $f^2(q)$ , where  $f^2(q)$  is the scattered intensity due to the interference by the

radiation scattered of the electrons present in the free atoms. Thus the elastically (or coherently) scattered intensity is  $I_{coh}(q) = NI_e f^2(q)S(q)$ , where  $N$  is the number of atoms and  $I_e$  the scattering by a single electron.  $I_e$  is a simple scale factor which we shall neglect from here on. For a dilute random arrangement of atoms, such as in an ideal gas,  $S(q)$  would be 1 (see Figure 1.1).

For a polyatomic sample  $S(q)$  is the average of the partial structure factors  $S_{ij}(q)$ , each weighted by the atomic scattering factors  $f_i(q)f_j(q)$ , where the indices  $i$  and  $j$  denote the elements. The factors  $f_i(q)$  depend on the exact radial distribution of the electrons in the atom, but to a good approximation they are the same function scaled with the number of electrons present in the atom. With this approximation the coherent scattering can be expressed by  $I_{coh}(q) = \sum_i f_i^2(q)S(q)$  [60].

The coherent scattering cannot be measured directly. From the measured intensity, the air scattering and the inelastic Compton scattering have first to be subtracted, and additional corrections must be made for the polarization of the x-rays, the absorption by the sample, the distribution of wavelengths in the primary beam and the band pass of the detector (see e.g. [61]). In discussing these corrections it is important to note that the mass absorption coefficient  $\mu/\rho$  of  $Pd_{40}Ni_{40}P_{20}$  for  $CuK_\alpha$ -radiation is  $143 \text{ cm}^2/\text{g}$  and the absorption coefficient  $0.136 \mu\text{m}^{-1}$ , so that multiple scattering can be neglected [60].

The  $30 \mu\text{m}$  thick sample is 4.1 absorption lengths thick and in consequence several corrections are small (see below). Most corrections are only of importance for the scan over the full  $q$ -range, from which the radial distribution function was calculated.

During an experiment in reflection mode half of the scattering volume is covered by the sample, so that the radiation scattered in the space behind the sample can be neglected. For that reason the correction to be applied for air scattering is half of the background radiation measured without sample. The air signal to be subtracted was 4.6, 1.1 and 0.5% of the maximum sample scattering at 1.2, 1.8 and  $2.9 \text{ \AA}^{-1}$  respectively.

The monochromator was set to pass only wavelengths in the vicinity of  $\lambda = \lambda_{\text{Cu}K\alpha}$ . The intensity of the  $K\alpha$ -radiation is an order of magnitude greater than the bremsstrahlung intensity in the same region. Hence, to a very good approximation, the wavelength distribution can be expressed by two  $\delta$ -functions:  $W(\lambda) = (2\delta(\lambda_{K\alpha 1}) + \delta(\lambda_{K\alpha 2}))/3$ .

Polarization by the sample and the monochromators was accounted for by the factor  $P(q) = 1 + \cos^2(2\theta) \cos^4(2\theta_M)$ , where  $2\theta_M$  is the scattering angle in the monochromator and analyzer.

The absorption correction is due to finite sample thickness,  $d$ . For symmetrical reflection the correction is:  $A(q, \lambda) = 1 - e^{-2\mu(\lambda)d \cos\theta}$ . The maximum correction for the  $\text{Pd}_{40}\text{Ni}_{40}\text{P}_{20}$  sample, at  $q = 7.4 \text{ \AA}^{-1}$ , is 3%.

Compton scattering is an important contribution at large  $q$ . The wavelength of the incoherent scattering is shifted according to:  $\lambda' = \lambda + 0.0486 \sin^2 \theta$ . The shift in wavelength leads to some reduction of the observed incoherent scatter because of the limited bandpass of the analyzer and affects the absorption correction because of the wavelength dependence of  $\mu$ . The following equation summarizes the corrections that had to be applied:

$$I_{\text{obs}}(q) = I_{\text{coh}}(q) + I_{\text{inc}}(q) + I_{\text{air}}(q) = \frac{I_0 N_a \rho}{M} \int \frac{W(\lambda)}{P(q)} \sum_i \left( A(q, \lambda) f_i^2(q) S(q) \nu(\lambda) + A(q, \lambda') c_i(q) \nu(\lambda') \right) d\lambda + I_{\text{air}}(q), \quad (2.3)$$

with:  $I_0$  the incident beam intensity,

$N_a$  Avogadro's number,

$\rho$  the sample density,

$M$  the formula weight,

$W(\lambda)$  the distribution of wavelengths after the monochromator,

$A(q, \lambda)$  the absorption correction,

$P(q)$ , the polarization factor,

$c_i(q)$  the Compton (incoherent) scattering factor and

$\lambda'$  the wavelength of the Compton-scattered radiation.

The integral in Equation 2.3 is reduced to a sum by the  $\delta$ -functions in in  $W(\lambda)$ .

The standard procedure to determine the prefactor  $I_0 N_a \rho / M$  is to measure the scattering to high values of  $q$  where  $S(q)$  converges to 1. The prefactor determines how much incoherent scattering is to be subtracted and gives a scale factor for  $S(q)$ . Here the  $q$ -range is limited by the wavelength of the  $\text{CuK}_\alpha$ -radiation, so that there is some uncertainty in the ratio between coherent and incoherent scattering at large angles. In spite of this, the procedure proved to be applicable, as was shown by the fact that the radial distribution function obtained by Fourier transforming  $S(q)$  gives about the right density.  $\rho_0$  was calculated self-consistently using the limit  $r \rightarrow 0$  of Equation 2.2, where  $\rho(r) = 0$ :

$$\rho_0 = \frac{1}{2\pi^2} \int_{q=0}^{\infty} q^2 (1 - S(q)) dq. \quad (2.4)$$

The numerical value of  $\rho_0$ ,  $6.5 \times 10^{22}$  atoms/cm<sup>3</sup>, is within 20% of the theoretical value  $\rho N_a / M = 8.15 \times 10^{22}$  atoms/cm<sup>3</sup>. The causes for the difference are the cutoff at  $q = 7.4 \text{ \AA}^{-1}$  in Equation 2.4 and the uncertainties in the determination of  $S(q)$ .

$S(q)$  (Figure 3.11) and  $\rho(r)$  (Figure 3.12) for a reference sample are shown in Section 3.3.1 where  $4\pi r^2 \rho(r)$  was calculated according to Equation 2.2. The deviation from  $\rho(r) = 0$  for small  $r$  (see Figure 3.12) is due to the cutoff at  $q = 7.4 \text{ \AA}^{-1}$ .

The absolute intensity varied by up to 1.5% because of drifts in the photon detection system, variations between the samples and in the mounting of the samples. To compare the structure factors directly, the integral of  $S(q)$  over the range from 1.8 to  $4.0 \text{ \AA}^{-1}$  was normalized to a constant value. A similar procedure was used by Chason *et al.* [34]. Normalizing the data in such a way is not harmful, since only the changes of shape of  $S(q)$  will be analyzed. Any information about changes in the absolute scattered intensity is of course lost. As a comparison, an estimate for the intensity change arising from density changes would be only of the order of 0.2% (compare Table 2.2). which is below the limit of detection.

## 2.6 Mössbauer Spectroscopy

A general review on the principles, methods and applications of Mössbauer spectroscopy is found in the monograph by Greenwood and Gibb [62]. The Mössbauer effect is based on the recoil-free emission and absorption of  $\gamma$ -rays. Since total momentum is conserved, a free atom would recoil after the emission of a  $\gamma$ -ray, and part of the energy of the nuclear transition would be lost to that recoil. In general this energy loss is sufficient to prevent the re-absorption of the  $\gamma$ -ray by a second, identical nucleus through the inverse transition. However, if the atom is bound in a solid or a viscous liquid, the recoil leads to the creation of a phonon. Since phonons are quantized states of the solid, a minimum energy is necessary for the creation of a phonon. If this energy is larger than the average recoil energy (as is true for  $E_\gamma < 150$  keV), there can be a significant probability for a zero-phonon event so that the  $\gamma$ -ray has the full energy of the nuclear transition. Such a photon can then be re-absorbed in a second, also recoilless, nuclear transition. This re-absorption is the basis of the Mössbauer effect, which is observed as an additional resonant contribution to the absorption of  $\gamma$ -rays by a solid.

The fraction of photons that are emitted or absorbed without recoil depends on the mean square vibrational displacement of the emitting nucleus. Thus the vibrational motion of the nucleus may be determined by the measurement of the recoil-free fraction.

To be suitable for Mössbauer spectroscopy the excited state of a nuclear transition must be sufficiently long lived for the energy distribution of the re-absorbed photons to be narrow, so that the nuclear hyperfine splitting, caused by the interaction of the nucleus with the electron shell of the atom, can be resolved. The most common experimental configuration, which we use here, employs a single line source, i.e. one where the hyperfine levels are degenerate. The energy of the emitted photons may be varied by moving the source, typically at a rate of a few millimeters per second, and therefore superimposing a Doppler shift to the photon energy. This

allows us to scan the energy of the emitted  $\gamma$ -rays over the hyperfine levels of the sample, which then appears as absorption lines in a velocity spectrum.

The local structure influences on the energy levels of the nucleus, mainly through the interaction of the  $s$ -electrons with the nucleus. Specifically, the energy levels of a nucleus are influenced by the electric monopole interaction, which gives rise to the isomer shift,  $\delta_{ISO}$ , the magnetic dipole interaction and the electric quadrupole interaction, which determines the electric quadrupole splitting,  $Q$ . In this study we are only interested in paramagnetic samples, so that we will be concerned with  $Q$  and  $\delta_{ISO}$ . These quantities will be discussed in more detail below.

The nuclear transition most commonly employed is the 14.4125 keV transition in  $^{57}\text{Fe}$ , which we have used here. The excited state is populated from the decay of  $^{57}\text{Co}$  by electron capture and the emission of a 121.9 keV  $\gamma$ -ray. 11 % of the decays of  $^{57}\text{Co}$  occur directly towards the ground state of  $^{57}\text{Fe}$  with the emission of 136.32 keV  $\gamma$ -rays. About 90 % of the 14.4 keV  $\gamma$ -rays are lost because they transfer their energy to internal conversion electrons. The excited state of  $^{57}\text{Fe}$  has a half life of 98 ns. and a nuclear spin quantum number  $I = \frac{3}{2}$ , while the the ground state has  $I = \frac{1}{2}$ .

The Mössbauer spectroscopy measurements were made in the standard absorption configuration at room temperature and at elevated temperatures.

### 2.6.1 The Recoil-Free Fraction

Any emission of phonons lowers the energy of the  $\gamma$ -ray and makes resonant absorption impossible. The probability for a zero-phonon process is  $f = \exp(-k^2\langle x^2 \rangle)$ , where  $k$  is the wave-number of the  $\gamma$ -ray and  $x$  is the amplitude of vibration of the nucleus (see e.g. [62]). In the framework of the Debye model one obtains in the limit of high temperatures ( $T \geq \theta_D/2$ ):

$$f = \exp\left(\frac{-6E_r T}{k_B \theta_D^2}\right). \quad (2.5)$$

Here  $E_r$  is the recoil energy of the nucleus, which is  $1.95 \times 10^{-3}$  eV for the 14.4 keV transition in  $^{57}\text{Fe}$ . The Debye temperature is of the order of 300 K for most solids.

## 2.6.2 The Center Shift

The center shift  $\delta$  is determined by two quantities, the isomer shift (IS) and the second order Doppler shift (SOD):  $\delta = \delta_{IS} + \delta_{SOD}$ . It is the shift in the centroid of the absorption spectrum, measured with respect to a standard, which is in this case an  $\alpha$ -Fe foil at room temperature.

The isomer shift corresponds to the electric monopole interaction between the nucleus and the  $s$ -electrons of the atom, which have a finite probability density at the nucleus. The nuclear volume changes during the transition from the excited state to the ground state, and in consequence does work against the electronic charge. Since the size effect scales with the charge density at the nucleus, the energy of the photon is shifted by an amount that depends on the environment of the atom.

The SOD is caused by the dependence of the frequency of the photon on the velocity of the nucleus, which in the full relativistic treatment is given by:

$$\nu' = \nu \left(1 - \frac{v}{c}\right) \left(1 - \frac{v^2}{c^2}\right)^{-1/2} \approx \nu \left(1 - \frac{v}{c}\right) \left(1 + \frac{v^2}{2c^2}\right)$$

The linear term is the classical Doppler shift of the frequency, and the quadratic term is the relativistic time dilation effect on the frequency. During the lifetime of the excited nuclear state of the order of  $10^6$  atomic vibrations occur. The velocity averages to zero, and in consequence the classical, linear Doppler shift is also zero. Thus we obtain:

$$\delta_{SOD} = -\frac{\langle v^2 \rangle E_\gamma}{2c^2}.$$

In the classical limit, which generally applies for temperatures larger than  $\theta_D/2$ ,  $\frac{M}{2}\langle v^2 \rangle = \frac{3}{2}RT$ . Here  $M$  is the nuclear mass and  $R$  the molar gas constant. Thus:

$$\delta_{SOD} = -\frac{3RTE_\gamma}{2Mc^2}.$$

## 2.6.3 The Quadrupole Splitting

Any nucleus with a spin quantum number greater than  $\frac{1}{2}$  has a non-spherical charge distribution, which, if expanded as a series of multipoles, contains a quadrupole term.

The interaction between this quadrupole moment and the electric field gradient (EFG) of the charge distribution outside the nucleus lifts the degeneracy of the levels of the nucleus, and the strength of this interaction determines the splitting of the absorption lines.

If  $V$  is the potential produced by the charges external to the nucleus, then the elements of the EFG tensor at the nucleus caused by the electronic charge are:

$$V_{ij} = - \left. \frac{\partial^2 V}{\partial x_i \partial x_j} \right|_{\vec{x}=0}.$$

For example the components  $V_{ik}$  of the EFG tensor caused by an assembly of discrete charges  $q_n$  (with Cartesian coordinates  $x_i^{(n)}$ , polar coordinates  $r_n, \theta_n, \phi_n$ ) at a nucleus (whose position defines the origin of the coordinate system) are given by

$$V_{ik} = \sum_n q_n (3x_i^{(n)} x_k^{(n)} - r_n^2 \delta_{ik}) r_n^{-5}. \quad (2.6)$$

$V_{ik}$  is a symmetric  $3 \times 3$  tensor ( $V_{ki} = V_{ik}$ ). By the definition above it has no source at  $\vec{x} = 0$  and in consequence zero trace ( $\sum_i V_{ii} = 0$ ). Thus it is determined by five independent quantities. It can be diagonalized, and the principal axes may be chosen such that the diagonal elements  $V_{xx}, V_{yy}, V_{zz}$  are ordered  $|V_{zz}| \geq |V_{yy}| \geq |V_{xx}|$ .

The degeneracy of the excited state with  $I = \frac{3}{2}$  is partially lifted to two states with  $I_z = \pm \frac{3}{2}$  and  $I_z = \pm \frac{1}{2}$ . This corresponds to two different energies for the transition to the ground state with  $I = \frac{1}{2}$ . The energy difference between these levels, called the quadrupole splitting, is given by:

$$Q_{\pm} = \pm \frac{eV_{zz}}{4} q \sqrt{1 + \eta^2/3}, \quad (2.7)$$

where  $\eta = (V_{xx} - V_{yy})/V_{zz}$ ,  $e$  is the electron charge and  $q$  the nuclear quadrupole moment. After diagonalization the five degrees of freedom in  $V_{ik}$  can be looked upon as  $V_{zz}$ ,  $\eta$  and the three Euler angles  $\alpha, \beta, \gamma$  defining the orientation of its main axes. Since the positions of the two lines give only the energy difference between the levels, it is not possible, in the absence of a magnetic field, to determine which of the lines corresponds to  $Q_+$  and  $Q_-$ . Thus the sign of  $V_{zz}$  cannot be determined. For an amorphous solid a mixture of positive and negative values of  $V_{zz}$  is expected [44],

although some experimental evidence for amorphous  $\text{Fe}_{24}\text{Zr}_{76}$  suggests that most values of  $V_{zz}$  are positive [63].

The value of  $Q$  increases with the deviation of the local charge distribution from spherical symmetry. In the case of axial symmetry, which means  $V_{xx} = V_{yy} = -V_{zz}/2$  ( $\eta = 0$ ), the case of  $V_{zz} > 0$  corresponds to a prolate symmetry, and the case  $V_{zz} < 0$  to an oblate symmetry. The results of the measurements will be interpreted in this sense.

#### 2.6.4 System Configuration

The Mössbauer absorption spectrometer consists of a radioactive source mounted on a drive, an absorber (the sample), the detector and the data acquisition system. A 1 GBq  $^{57}\text{CoRh}$  single line source was mounted on a constant acceleration drive which varied the source velocity between  $-2$  and  $+2$  mm/s, superimposing a Doppler energy shift to the emission line.<sup>3</sup> A proportional counter filled with a mixture of xenon and 3 %  $\text{CO}_2$  at the pressure of  $10^5$  Pa (1 atmosphere) was used as a detector. It was equipped with a beryllium entry window to maximize the sensitivity for the resonant 14.4 keV  $\gamma$ -rays and an exit window to minimize the scatter of the 122 and 136 keV radiation. Further signal discrimination was provided by a pulse height analyzer. During the experiment the sample is moved back and forth, while the velocity is scanned. In a complete cycle of motion, the source is at the same velocity twice. For this reason the data, collected into 512 channels, contain the absorption spectrum and its mirror image. These two spectra were compounded into a single spectrum of 256 channels by folding the initial spectrum about a point close to the center. The exact folding point as well as the velocity and isomer shift calibration numbers were obtained from the spectrum of an  $\alpha$ -Fe foil recorded at room temperature in the same measuring geometry. The width of the absorption lines observed using this foil was  $0.116 \text{ mm s}^{-1}$ , which is close to the natural linewidth

---

<sup>3</sup>It is convenient to express all energy shifts as velocities. A velocity of 1 mm/s corresponds to an energy shift of  $0.048 \mu\text{eV}$ .

of the transition,  $0.097 \text{ mm s}^{-1}$  [62].

### **2.6.5 Room Temperature Measurements**

For room temperature measurements, pieces of ribbon were glued with adhesive tape onto a lead ring with a 11 mm diameter hole, and placed in front of the detector. It was important to cover the whole area, otherwise there would have been a large background due to radiation passing unattenuated through the holes. The total resonant absorption by the samples mounted in this fashion reduced the transmitted intensity on resonance by about 15%. The geometry was kept the same for all measurements, the distance between source and detector being 12 cm. In order to obtain data of sufficient quality the counting time was approximately 24 h which gave  $\approx 10^6$  counts per channel. This results in statistical fluctuations of the order of 0.1%. Changes in the absorption of about 0.01% can be detected since the number of counts per channel is doubled by the folding procedure and the absorption peaks have a half-width of about sixty channels.

### **2.6.6 Mössbauer Furnace and High Temperature Measurements**

Since the samples deteriorate rapidly at elevated temperatures, the high temperature measurements required high count-rates to obtain good spectra in a short time. A furnace with a short beam-path, good temperature stability and a small temperature gradient over the sample was therefore designed and built. The basic design features have been adapted from [64], including the use of a heated radiation shield to reduce the thermal gradients close to the sample. A cross-section of the design is given in Figure 2.6, and photographs are shown in Figure 2.7, 2.8 and 2.9.

The sample space can be accessed easily by removing the front plate of the furnace and the radiation shield covers. The necessary electrical connections are brought in from the opposite side. The the outside container of the furnace, made

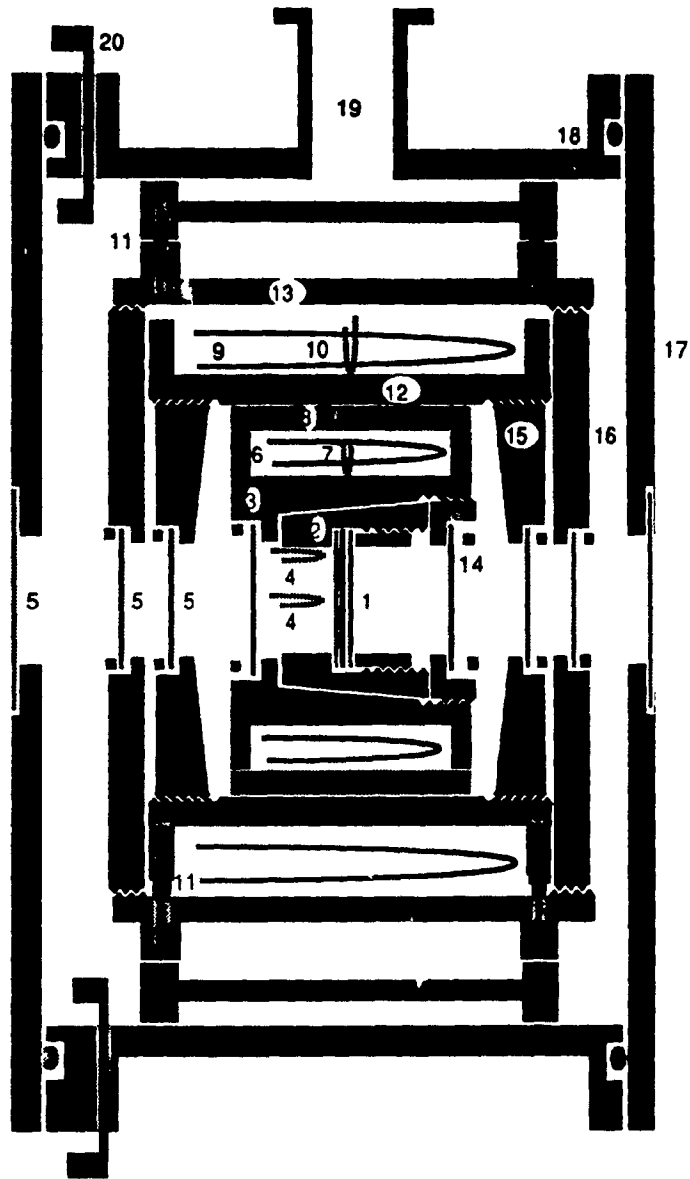


Figure 2.6: Schematic cross section of the Mössbauer furnace.

- |    |   |    |  |
|----|---|----|--|
| 1  | sample, clamped between two beryllium disks                       | 3  | body of the inner furnace                                      |
| 2  | removable sample holder   | 6  | heating coil of the inner furnace                              |
| 4  | two thermocouples placed at the center and the edge of the sample | 7  | controlling thermocouple of the inner furnace                  |
| 5  | beryllium windows   | 8  | ceramic tube (thermal insulation of the inner furnace)         |
| 9  | heating coil of the heated radiation shield                       | 11 | ceramic rods (thermal insulation of the two radiation shields) |
| 10 | controlling thermocouple of the heated radiation shield           | 12 | body of the heated radiation shield                            |
| 14 | cover of the inside furnace                                       | 15 | cover of the heated radiation shield                           |
| 16 | cover of the outer radiation shield                               | 17 | cover of the vacuum can  |
| 18 | O-ring seal   | 19 | vacuum connection  |
| 20 | insulated electrical feedthrough                                  |    |  |

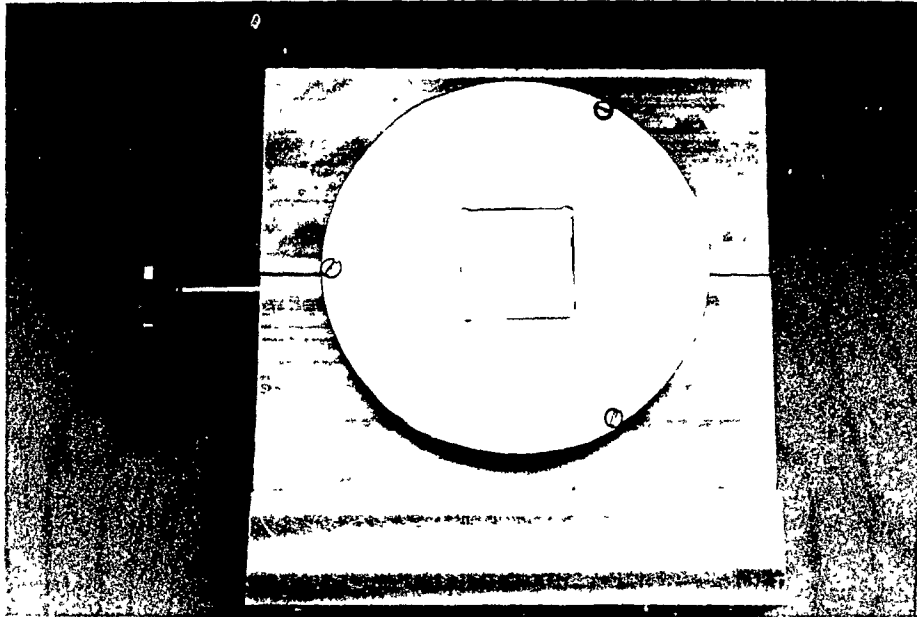


Figure 2.7: Photograph of the Mössbauer furnace (front view). The furnace is shown mounted in its aluminium holder. One of the square beryllium vacuum windows is at the center of the furnace. Removing the three screws allows to access the sample space. The vacuum connection is at the left side.

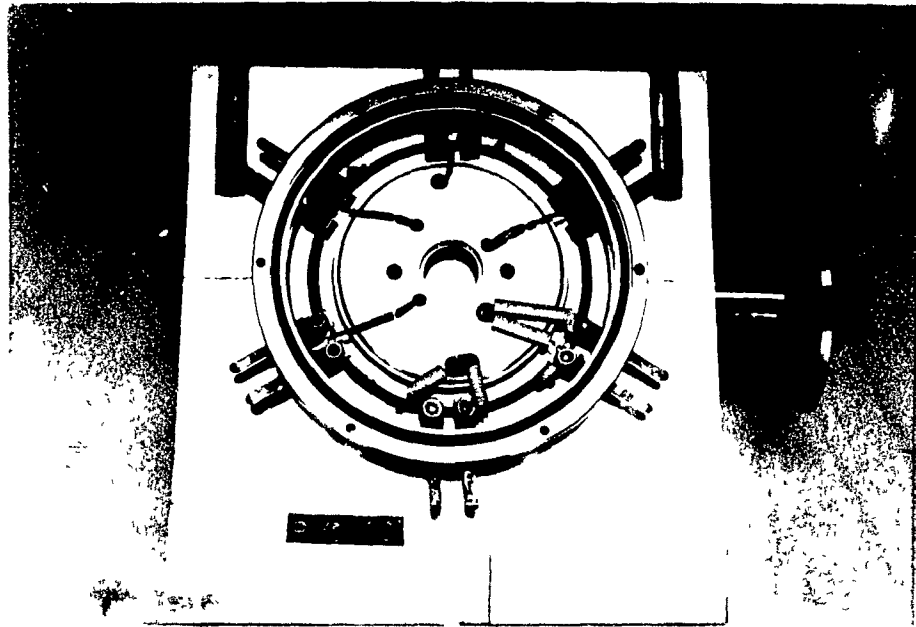


Figure 2.8: Photograph of the Mössbauer furnace (rear view). The back cover of the vacuum can is removed to show the electrical connections. The circular beryllium window of the radiation shield is at the center. The thin wires lead to the four thermocouples, and the thick leads are the power connections for the heated radiation shield (bottom) and the inside heater (bottom right).

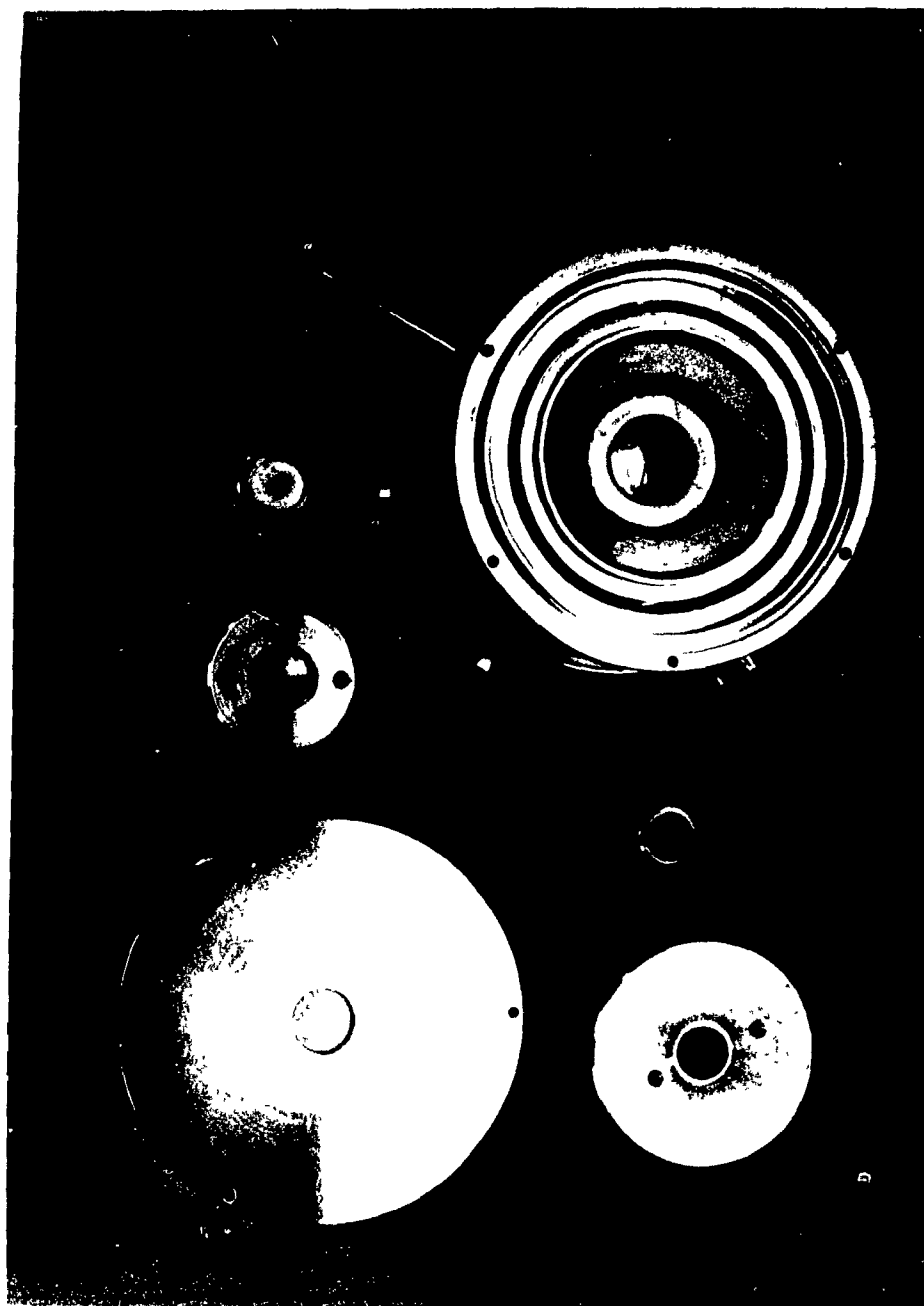


Figure 2.9: Photograph of the disassembled Mössbauer furnace (front view). The furnace (top right) is shown without the aluminum holder. The thin wires in the sample space are the two thermocouples. The sample holder, a conical tube, is shown below the furnace (center right). The ring left to it holds the sample. A beryllium window (top left) closes the sample space. The cover of the heated radiation shield is shown at the center left, and the cover of the outer radiation shield at the bottom right. The vacuum can is sealed with its cover (bottom left).

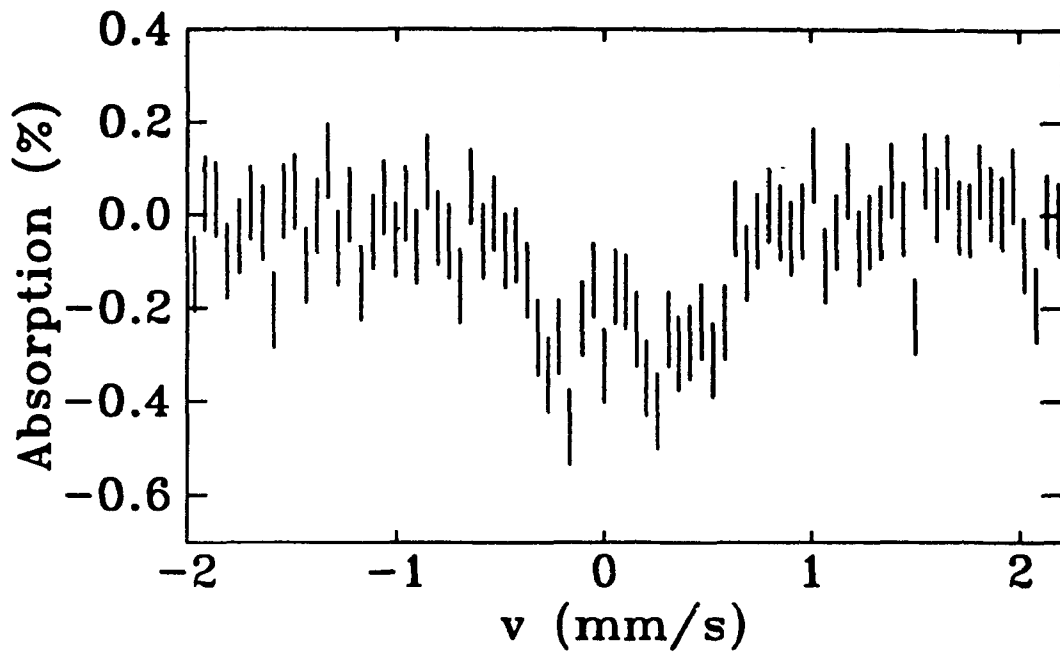


Figure 2.10: Resonant absorption by the beryllium windows of the Mössbauer furnace.

of nickel-electroplated brass, can be evacuated. Beryllium has a very low cross section for x- and  $\gamma$ -rays. Here beryllium foils were used as windows to the vacuum can and as radiation shields along the beam path inside the furnace. The traces of iron in the beryllium windows caused only a very small amount of resonant absorption (shown in Figure 2.10), which was neglected in the analysis of the data. O-rings sealed the front and the back cover of the furnace. Epoxy was used as a vacuum seal between the beryllium windows and the vacuum can, and provided the insulated electrical feedthroughs for the heating coils and four chromel-alumel thermocouples into the vacuum. Inside the vacuum container was a radiation shield made of nickel-electroplated copper. The high thermal conductivity of the copper smoothed out temperature gradients, and the electroplating protects against oxidation, which would reduce the reflectivity of the radiation shield. The shield is held in place by twelve ceramic rods each of diameter 1.7 mm. These beryllium windows, as with all the other ones inside the vacuum container, are kept in place by small rings. Twelve ceramic rods hold the heated radiation shield, made out of stainless steel.

The heating element consists of two parallel coils, each made of 2.6 m of 0.25 mm thick Kanthal<sup>TM</sup> wire. The coils are wound non-inductively (so that the furnace can also be used for the measurement of magnetic samples) in a double layer around the radiation shield. The wire was positioned by feeding it through four-lead ceramic rods, which were then cemented into place. A thermocouple was placed between the heating coils and the body of the radiation shield to measure the temperature. Inside the radiation shield is the sample mount and heater, constructed similarly to the radiation shield with 1.9 m of heating wire and equipped with a sensing thermocouple. The sample holder can be removed to change the sample. The sample is placed between two beryllium disks, which are kept in place by a screw. Thermocouples located both at the center and at the edge of the sample allow measurement of average sample temperature and estimation of temperature gradients.

The temperature of the heated radiation shield and the sample holder are controlled by two separate commercial controllers (Omega<sup>TM</sup> CN9000 and CN5000 respectively). The sample temperature and the temperature gradient are monitored simultaneously. The furnace was operated with argon. In the temperature regime of interest the outside of the furnace remained below 70°C. Typical operating conditions are given in Table 2.3.

In combination with the 1 GBq source the very high count-rate of 8400 s<sup>-1</sup> was achieved. Usable data were obtained with counting times as short as 20 min.

### 2.6.7 Data Fitting Procedures

As stated above, Mössbauer spectroscopy is sensitive to three parameters related to the chemical environment of the nucleus: the magnetic dipole field, the electric quadrupole field and the charge density. Since Pd<sub>40</sub>Ni<sub>40</sub>P<sub>20</sub> is paramagnetic, only the latter two parameters appear here. The measured spectra (see Figure 2.11) are broad asymmetric quadrupole-split doublets. The breadth of the lines is about twice the instrumental linewidth and is a result of the range of atomic environments present in the amorphous solid.

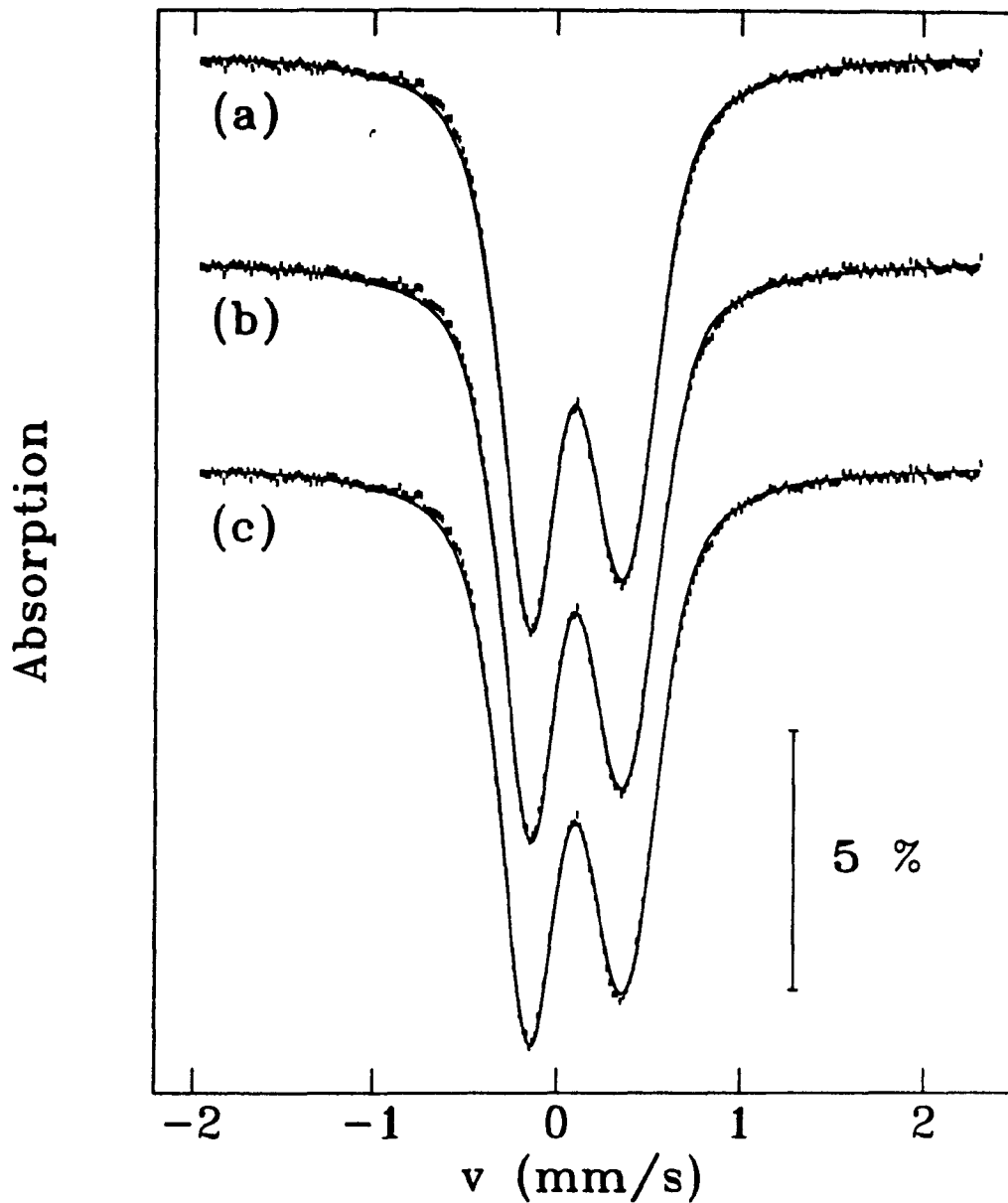


Figure 2.11: Mössbauer spectrum of an as-quenched  $\text{Pd}_{40}\text{Ni}_{40}\text{P}_{20}$  sample. The solid lines are fits to the data, where the quadrupole field distribution was fitted in three different ways: (a) by a histogram, (b) by a Fourier series and (c) by a Gaussian (see Figure 2.12).

Table 2.3: Operating conditions of the Mössbauer furnace. The values given for the thermal gradients are an upper limit since they were measured outside the sample body. The operating voltages were chosen so that the power was switched on by the controlling circuits about half the time (50 % duty cycle).

Backfill Pressure		$3 \times 10^{-3}$ Pa	$2 \times 10^4$ Pa	$2 \times 10^4$ Pa
Sample:	Temperature	$635 \text{ K} \pm 1 \text{ K}$	603 K	471 K
	Temperature-Gradient	$2.8 \text{ K} \pm 0.1 \text{ K}$	1.2 K	0.9 K
Heated Shield:	Temperature	666 K	610 K	482 K
	Applied Voltage	28 V	37 V	22 V
	Power	17 W	34 W	12.1 W
Sample Mount:	Temperature	638 K	603 K	470 K
	Applied Voltage	4 V	8 V	6 V
	Power	0.3 W	1.1 W	0.6 W

The spectrum of a single atomic site in a crystalline material would appear as two Lorentzian lines of equal intensity, separated by a quadrupole splitting  $Q$  – with its centroid shifted by  $\delta_{ISO}$ , which is determined for a this site by the electron density at the nucleus and the temperature. The width of the Lorentzian lines depends on the natural linewidth of the transition and the resolution of the instrument.

The measured spectrum in a glass is the statistical average over the different atomic sites. Each site has a specific  $Q$  and  $\delta_{ISO}$ , and Mössbauer spectrum of the glass is determined by the distributions of the values of  $Q$  and  $\delta_{ISO}$ . Although each site of the glass contributes a symmetric pair of lines, the observed spectra are asymmetric. This apparent asymmetry in the line intensities must result from a correlation in the statistical distribution of  $Q$  and  $\delta_{ISO}$ . This is not unexpected because both  $Q$  and  $\delta_{ISO}$  depend on the local distribution of electric charges.

A general model should allow two correlated distributions of  $\delta_{ISO}$  and  $Q$ . Unfortunately, the effects on the fitted spectrum of a distribution of  $\delta_{ISO}$  and a distribution of  $Q$  are too similar to be extracted from the measured spectrum. Thus we

only allow a one-dimensional distribution of atomic sites, such that the value of  $\delta_{ISO}$  is linked to the value of  $Q$ . For the correlation between the two values, we assumed the simplest, linear case:

$$\delta_{ISO} = \langle \delta_{ISO} \rangle + a(Q - \langle Q \rangle). \quad (2.8)$$

The inclusion of higher order terms in this expansion has been tried, but did not improve the quality of the fit enough to justify the inclusion of another variable parameter.

Two methods are generally used for handling general distributions of hyperfine fields in Mössbauer spectroscopy. The first describes the distribution by a histogram (this technique has first been used by Hesse and Rübartsch, 1974 [65]), while the other expands it in a Fourier series (Window, 1970 [66]). Both methods have been implemented and employed in conjunction with a least squares fitting routine. The fits for an as-quenched sample are shown in Figure 2.11, and the corresponding distributions in Figure 2.12. The quadrupole field distributions are nearly Gaussian. The spectrum in Figure 2.11, for an as-quenched sample, deviates most from that shape. To constrain the fitting procedure further and to stabilize the fitted parameters the distribution was forced to be Gaussian, with a mean value  $\langle Q \rangle$  and a width  $\sigma = \langle Q^2 - \langle Q \rangle^2 \rangle$ . The resulting fit and distribution is shown in Figure 2.12.c. This method was used for most of the Mössbauer data analysis.

Apart from the hyperfine-field values two further parameters describe a measured spectrum. The baseline  $B$  is the average number of counts per channel far away from the Mössbauer resonance, and thus dependent only on the counting time and sample thickness. The absorption  $A$  depends on the number of resonant nuclei, their distribution in the absorber and the temperature dependent recoil-free fraction.

The exact form of the expression used for fitting the transmitted intensities,

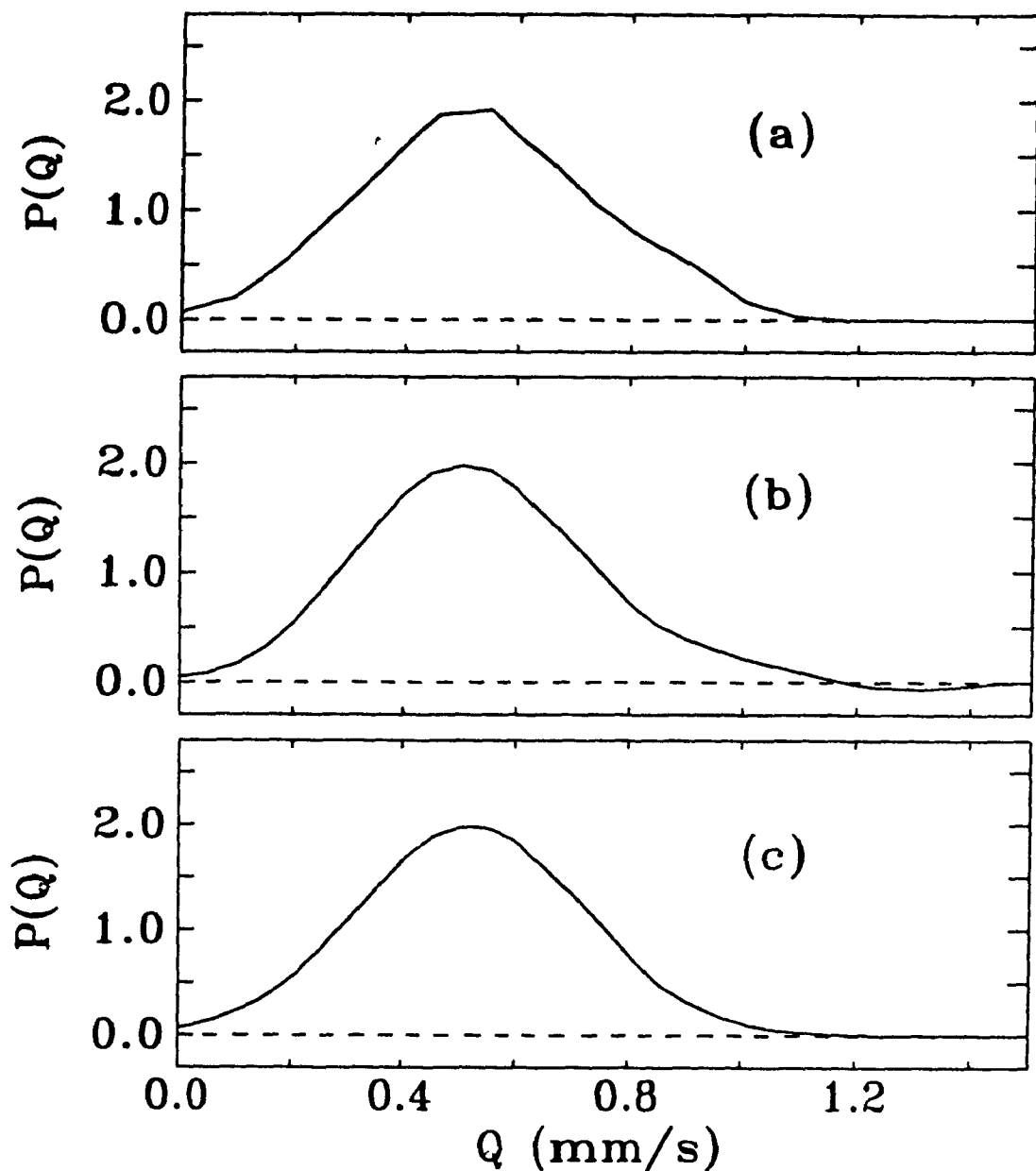


Figure 2.12: The quadrupole splitting distributions obtained by three fitting methods. (a) approximation of the quadrupole field distribution as a histogram with twelve contributions. The resulting histogram has been smoothed with a three-point binomial weighting to remove oscillations arising in  $P(Q)$  from the instability of the fit. (b) Expansion of  $P(Q)$  in as a Fourier series with six terms. (c) Fit of  $P(Q)$  to a Gaussian.

$C$ , as a function of the source velocity  $v$ , is:

$$C(v) = B \left\{ 1 - \frac{A\sigma}{\sqrt{2\pi}} \int_0^{\infty} \exp \left[ -\frac{[Q - \langle Q \rangle]^2}{2\sigma^2} \right] (L_+(v, Q) + L_-(v, Q)) dQ \right\} \quad (2.9)$$

with the Lorentzian lineshape:

$$L_{\pm}(v, Q) = \frac{\Gamma^2}{[v \pm Q/2 + \langle \delta \rangle + a(Q - \langle Q \rangle)]^2 + \Gamma^2}. \quad (2.10)$$

The maxima of the two Lorentzian lines are at the two quadrupole resonances  $\pm Q/2$ , which are both shifted by the same isomer shift (Equation 2.8). The Gaussian term weights the contributions for the different values of  $Q$  to the spectrum.

The solid line in Figure 2.11.c is the fit to the absorption spectrum according to Equation 2.9, which describes the measured spectrum very well. Nonetheless some systematic deviations between the fit and the data do exist. The residual error, as the difference between the data and the fitted curve in Figure 2.11.c, is shown in Figure 2.13. The reasons for the deviations are (1) the dependence of the line shape on the absorption due to saturation effects [67], (2) variations of the sample thickness in the absorber and (3) the approximations made in the model, namely no independent distribution for the center shift, only a linear correlation between the quadrupole splitting and the center shift, and no non-gaussian components in the quadrupole field distribution. The differences between the spectra are of the same order as the difference between the fit and the data. Nonetheless the spectra can be analyzed using the fitting procedure described above because the residual error is small and approximately the same for all the data sets.

The temperature dependence of the Mössbauer spectrum was measured on the same sample *in situ*. Therefore no other parameters varied, and the areas of the spectra were proportional to the recoil-free fraction  $f$ . The areas were calculated as the difference between the fitted baseline and the average number of counts per channel.

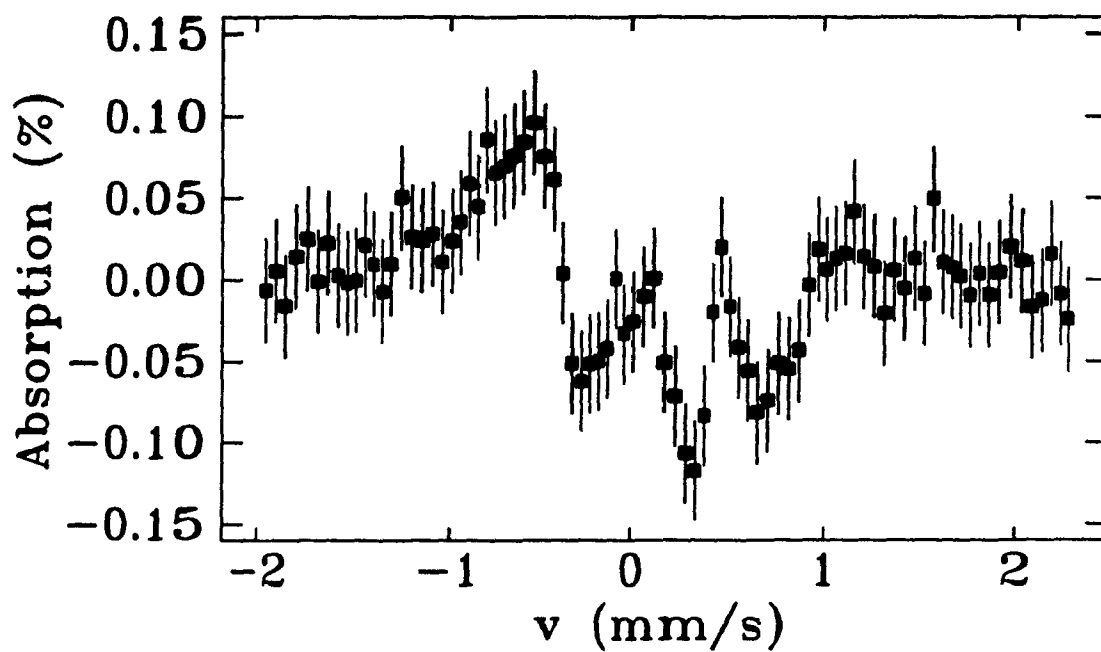


Figure 2.13: The residual error in fitting the Mössbauer spectra. Plotted is the difference between the data and the fit in Figure 2.11.c. Each three neighboring points have been averaged for clarity.

## Chapter 3

# Structural Relaxation

### 3.1 Introductory Remarks

In Chapter 1 reasons were given why Differential scanning calorimetry (DSC) is probably the best macroscopic technique for detecting and characterizing structural relaxation. This technique has been used to determine the dependence of relaxation effects on the composition, the preparation conditions and the thermal history of the glasses, as well as the kinetics of structural changes. Changes of the density of the sample were measured directly to provide both a second macroscopic parameter and a consistency check.

These data are the starting point for *direct* measurements of the local structural changes. X-ray diffraction, sensitive to the radial distribution of the atoms, and Mössbauer spectroscopy, giving information on to the local site symmetry, were used as complementary probes of the local atomic structure. These results will be related to and scaled with the calorimetric data.

## 3.2 Calorimetry

In this section the enthalpy and enthalpy flow for the liquid, the crystal and the glass are described schematically to explain the origin of the calorimetric signals that we are going to use to parameterize structural relaxation. The considerations that follow were originally based on work on conventional glasses, and antedate the production of metallic glasses (more detail can be found in the review articles by Kauzmann (1948) [68], Davies and Jones (1953) [69] and the book by Feltz [70]), but they apply equally to all glasses.

Figure 3.1 (top) sketches how the enthalpy of the liquid, the crystal and the glass vary with temperature upon heating and cooling. Figure 3.1 (bottom) displays the resulting specific heat. Upon slow cooling the liquid crystallizes at  $T_m$ , the melting point, and the enthalpy follows the crystal line. The line AB indicates the metastable equilibrium (supercooled liquid), which is reached upon cooling the liquid rapidly below  $T_m$ . The deviation from AB marks the transition from the supercooled liquid to the structurally frozen glass (line AD, or AC for even faster cooling), and the point of deviation is the glass transition temperature. The line AC might for example correspond to the rapid cooling typical for the manufacture of a metallic glass, and the line AD to relatively slow cooling at about 1 K/s. Irreversible relaxation corresponds to the evolution of the glass between a state along the line LK to a state along the line DA. The hysteresis indicated for heating and cooling along AD gives rise to an endothermic peak, the signature of the glass transition in calorimetry. The specific heat of the supercooled liquid is markedly higher than the specific heat of the glass, which differs only very little from the specific heat of the crystal. The line AB indicates the metastable equilibrium for the supercooled liquid. The glass, cooled along AD, evolves upon annealing at  $T_a$  along the line FG. For some temperature range the glass equilibrates on laboratory time scale, *i.e.* it reaches the line AB. As the glass is heated again, it moves along the line EA, and a sharp endothermic peak in the heat flow appears, as shown in Figure 3.1 (bottom). The glass may be cycled repeatedly along the closed loop FGAF, which represents

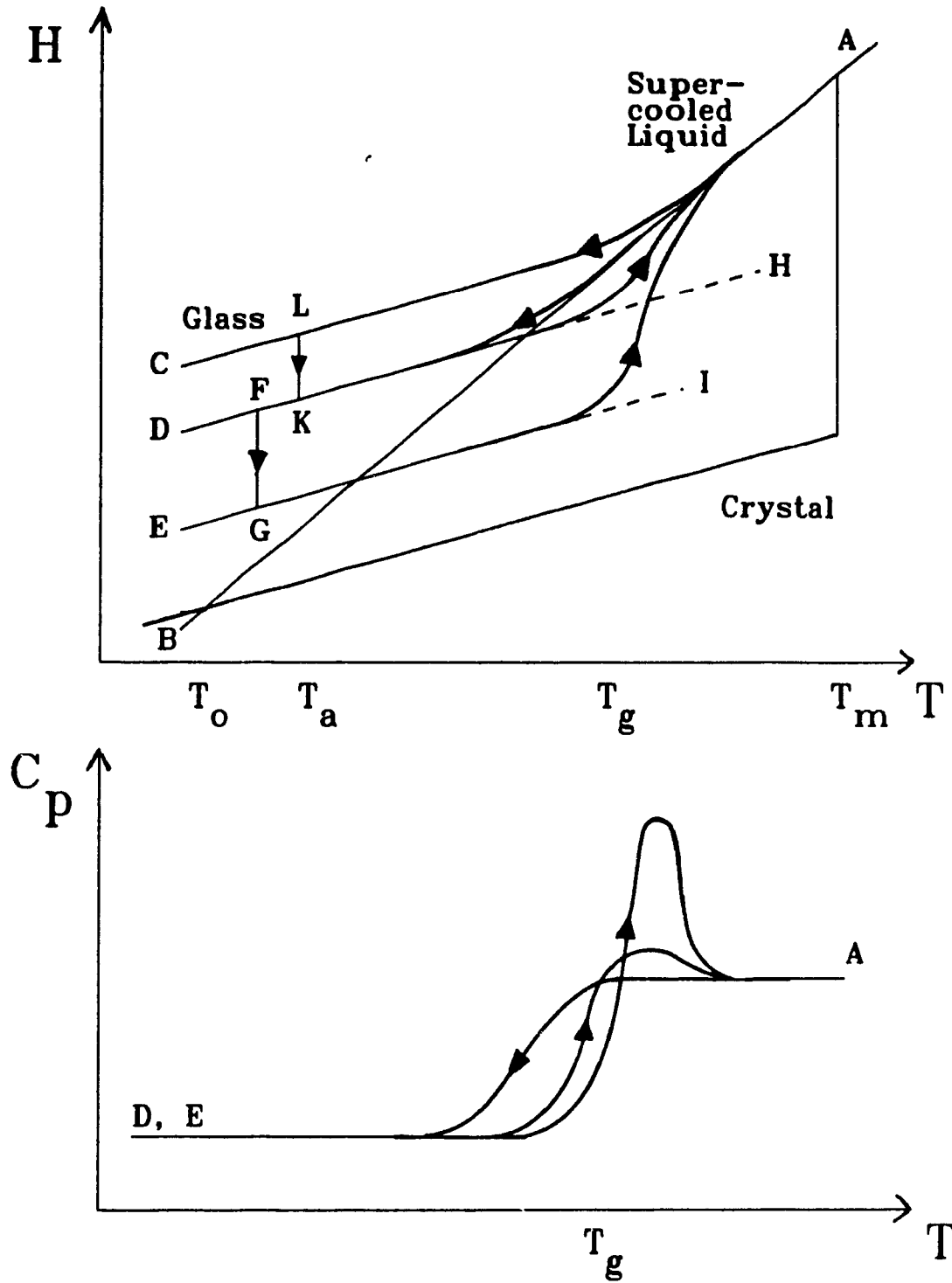


Figure 3.1: Schematic diagram of the dependence of the enthalpy (top) and the specific heat (bottom) on the temperature and the thermal history.

reversible relaxation. Upon fast heating the glass moves through isoconfigurational states (Spaepen and Turnbull, see e.g. [6,26]), such as along DH or EI. To parameterize the state of the glass Tool introduced the fictive temperature,  $\bar{T}$ , where the glass would be in metastable equilibrium (line AB) upon an instantaneous and thus isoconfigurational temperature change (Tool, 1946 [71]).

As already mentioned in Chapter 1, structural relaxation involves processes with a wide range of activation energies. Annealing at low temperature also changes the enthalpy of the glass, but the appearance of the processes is different. The heating curve of a glass which has been annealed at 425 K, far below  $T_g$ , is shown in Figure 2.2, compared to a glass that has been cooled at the same rate, but not annealed (indicated by the extrapolated baseline). The endothermic peak of a glass annealed at low temperature is much wider than the signature observed close to  $T_g$ , which was discussed above. As a consequence, two glasses of the same composition, cooled at slightly different rates, may still have the same enthalpy if the more rapidly cooled glass is subsequently annealed at a low temperature. Still their states are clearly different and distinguishable. The description of the state of the glass by a single parameter such as the fictive temperature, and in consequence a diagram like Figure 3.1, is therefore only valid for temperatures close to  $T_g$ .

### 3.2.1 Crystallization and Glass Transition

Irreversible relaxation processes occur only upon the first heating to  $T_g$  after manufacture. Because at the glass transition the system is in thermodynamic equilibrium, all effects due to the thermal history of the glass are removed. In consequence reaching  $T_g$  allows us to define a glassy state which is independent of the preparation conditions and only depends on the composition of the glass. This *reference state* shall be defined as the state obtained by cooling the sample through the glass transition at a slow rate, approximately 1 K/s, or, if the sample crystallizes below  $T_g$ , by heating the sample to just below the onset of crystallization and cooling it slowly. By the very nature of the reference state every amorphous sample can always be

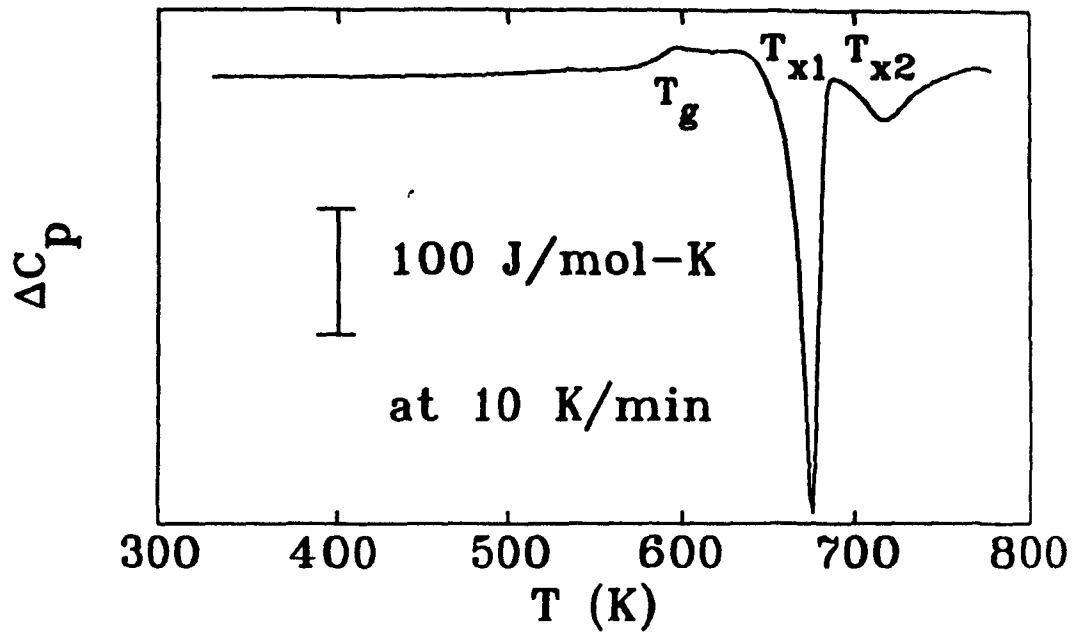


Figure 3.2: DSC trace of the glass transition and crystallization in Pd<sub>40</sub>Ni<sub>40</sub>P<sub>20</sub>. The difference between the heat flow of the sample in the reference state and the heat flow of the crystallized sample is shown.

reset to it. All other states of the sample will be compared to this state.

As an illustration of a DSC trace Figure 3.2 gives the heat flow for Pd<sub>40</sub>Ni<sub>40</sub>P<sub>20</sub>, measured at a heating rate of 40 K/min. Before the measurement the sample had been brought to the reference state by heating to 620 K and then cooling at 40 K/min to room temperature. The small endothermic peak at 570 K is characteristic of the glass transition. The large exothermic peak at 660 K is due to crystallization, and the second exothermic peak is due to a crystal-crystal transformation.<sup>1</sup> The background heat flow of the same crystallized Pd<sub>40</sub>Ni<sub>40</sub>P<sub>20</sub> sample, measured *in situ*, was subtracted from the trace in Figure 3.2. The absolute specific heat of Pd<sub>40</sub>Ni<sub>40</sub>P<sub>20</sub> was measured by Kui and Turnbull [72].

The crystallization temperature,  $T_x$ , depends on the heating rate since the nucleation and growth of crystals in the supercooled liquid or the glass takes some

<sup>1</sup>A detailed description of the crystallization process, the crystallization products and the glass forming range in the (Pd<sub>0.5</sub>Ni<sub>0.5</sub>)<sub>1-x</sub>P<sub>x</sub> was given by Wachtel *et al* [46].

time.  $T_g$  also depends on the cooling rate, although more weakly. Gronert *et al.* found that  $T_g$  only changed by 130 K in a Pd-Cu-Si glass for a difference in cooling rates of more than seven orders of magnitude [73]. These considerations will become important in Chapter 4, which reports an isothermal measurement of the glass transition. To gain a better understanding of the kinetics of the glass transition, crystallization and structural relaxation the activation energies for these various processes were determined. Processes are called activated if they follow Arrhenius kinetics. In order for a process to occur, a fluctuation in the local free energy must be sufficient to overcome a barrier, the activation energy  $E_a$ . The rate of change of the reacted fraction,  $x$ , depends on the amount of material that is left to react. Thus:

$$\frac{dx}{dt} = \nu_0 (1 - x)^n \exp\left(\frac{-E_a}{k_B T}\right),$$

where  $n$  is the order of the reaction, which describes autocatalytic effects, and  $\nu_0$  some characteristic vibration frequency close to the Debye frequency ( $\approx 10^{13}$  Hz). For isothermal conditions, the time it takes until the reaction is completed may be approximated by:  $\tau = \nu_0 \exp E_a/k_B T$ . In many cases it is experimentally more convenient to heat the sample at a constant rate (so-called isochronal) and to record the temperature of transformation for various heating rates  $\Phi$ . Kissinger showed that the expression then translates into a linear dependence of  $\ln(\Phi T^{-2})$  against  $T^{-1}$ , where  $T$  is the temperature of the peak of the thermal signature [74]. The activation energy is then proportional to the slope of the line and  $\nu_0$  is related to the offset. This is shown in Figure 3.3 for the crystallization and the glass transition in  $\text{Pd}_{40}\text{Ni}_{40}\text{P}_{20}$ . Table 3.1 gives the activation energies found for the various processes calculated from the slopes in Figure 3.3. The trial frequencies calculated for the glass transition and the endotherm after annealing at 545 K are unphysically high. This is a reflection of the fact that the Arrhenius model was used for processes where it does not strictly apply: the glass transition has, from the point of view of its kinetics, more the character of a phase transition which occurs at a fixed temperature independent of the heating rate. Phase transitions are characterized by long range coherence in

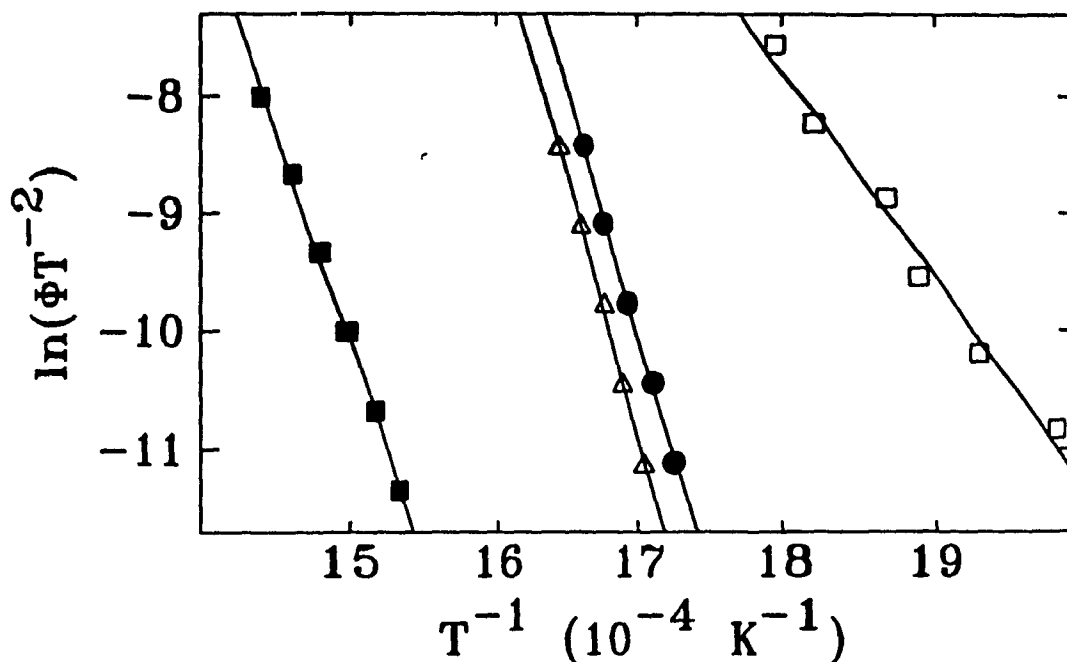


Figure 3.3: Heating rate dependence of various processes in  $\text{Pd}_{40}\text{Ni}_{40}\text{P}_{20}$ . The heating rates  $\Phi$  are between 5 and 160 K/min, and the units of  $\Phi T^{-2}$  are  $\text{K}^{-1}\text{min}^{-1}$ . The symbols correspond to:  $\blacksquare$  crystallization,  $\bullet$  glass transition,  $\square$  reversible relaxation  $T_a = 450$  K and  $\triangle$  reversible relaxation  $T_a = 545$  K. The results for reversible relaxation will be discussed in Section 3.2.3.

Table 3.1: The activation energies  $E_a$  and the trial frequencies  $\nu_0$  for various processes. The results for reversible relaxation will be discussed in Section 3.2.3.

Process	$E_a$ (eV)	$\nu_0$ ( $\text{s}^{-1}$ )
Crystallization	3.16	$1 \times 10^{21}$
Glass Transition	3.53	$2 \times 10^{27}$
Reversible Relaxation:		
$T_a = 450$ K	1.49	$2 \times 10^{11}$
$T_a = 545$ K	3.73	$8 \times 10^{31}$

the physical system, which is irreconcilable with the notion of localized activated processes. Even for crystallization, which is usually looked upon as an activated process, the trial frequency is still much higher than the Debye frequency, although significantly lower than the value obtained for the glass transition. Nonetheless this description provides a useful parameterization, as the straight lines in the Kissinger plot fit the data quite well. This allows to extrapolate to estimate the reaction times at lower temperature. One can see that for even lower heating rates than accessible by DSC, or even lower than feasible on experimental time scales, one would expect  $\text{Pd}_{40}\text{Ni}_{40}\text{P}_{20}$  to crystallize before reaching the glass transition.

### 3.2.2 Irreversible Relaxation

As a metallic glass is heated for the first time after manufacture, processes are activated which optimize the structure and allow the glass to reach a state of lower internal energy.<sup>2</sup> Calorimetry detects the energy released in these processes. Figure 3.4.a shows the difference in enthalpy flow between the first temperature scan of an as-made sample and the reference state for a  $\text{Pd}_{40}\text{Ni}_{40}\text{P}_{20}$  sample. It is very sensitive to the quench condition and the thermal history of the sample. This is well illustrated in Figure 3.5, (taken from Altounian, 1987 [75]), which shows an increase in the total enthalpy change  $\Delta H_{irr}$  with quench rate (wheel speed). An even more dramatic example, the dependence of  $\Delta H_{irr}$  on the method of amorphization is shown in Figure 3.6. Here a melt-spun sample and one amorphized by mechanically alloying are compared. (Mechanical alloying refers to strong mechanical working, for example by ball milling (see e.g. [76]), during which suitable crystalline starting materials may react via interdiffusion to give an amorphous product [77].) Immediately after preparation, the mechanically alloyed sample<sup>3</sup> exhibits a very large irreversible endotherm, beginning at about 340 K. Presumably this is caused by

---

<sup>2</sup>It must be stressed that in this study we are only concerned with processes within the glassy regime, i.e. without the occurrence of crystallization

<sup>3</sup>The sample was provided by Ludwig Schultz, Siemens Central Research, Erlangen

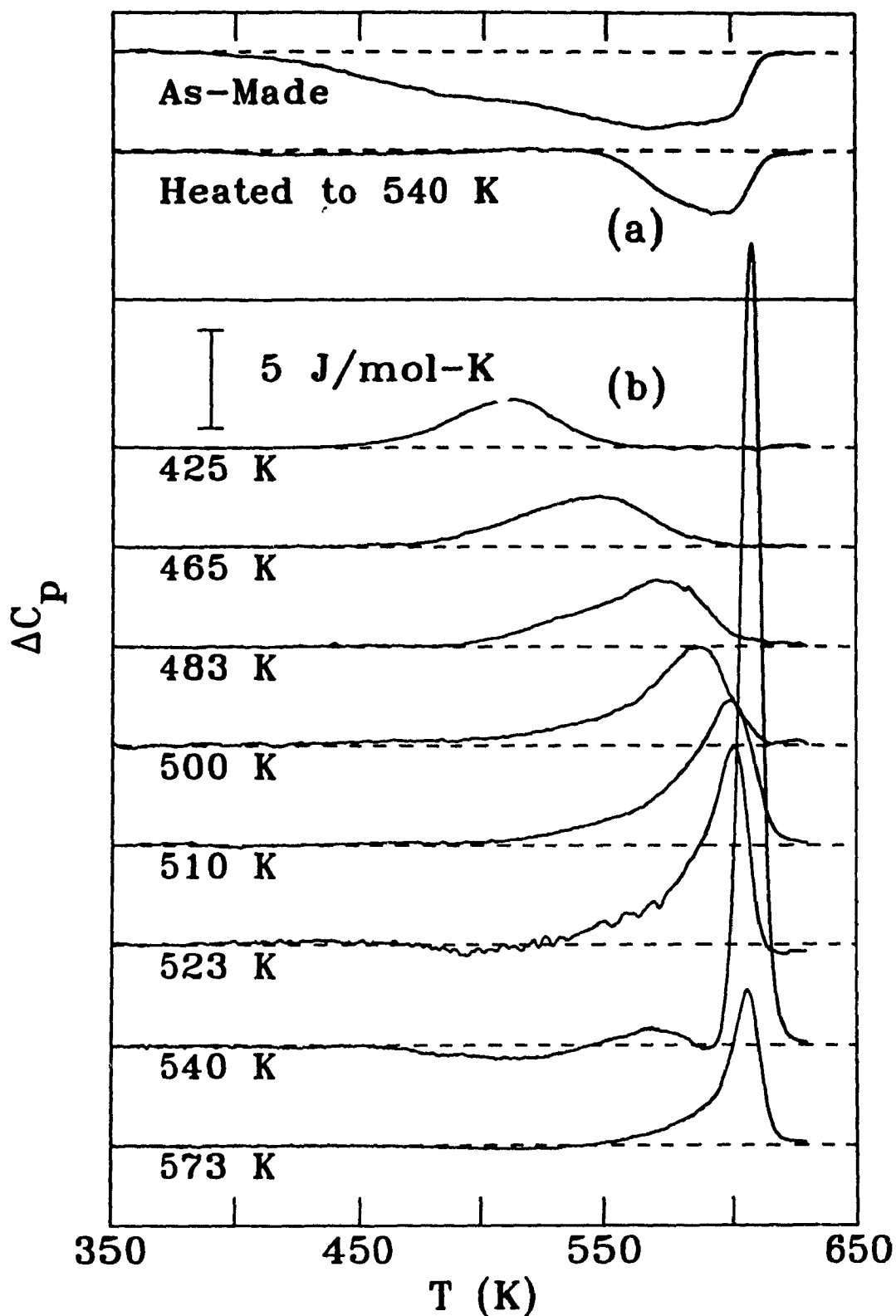


Figure 3.4: Heat flow during irreversible (a) and reversible structural relaxation (b) in  $\text{Pd}_{40}\text{Ni}_{40}\text{P}_{20}$ . For the measurements of reversible relaxation the samples were annealed for 20 h at the temperatures indicated.

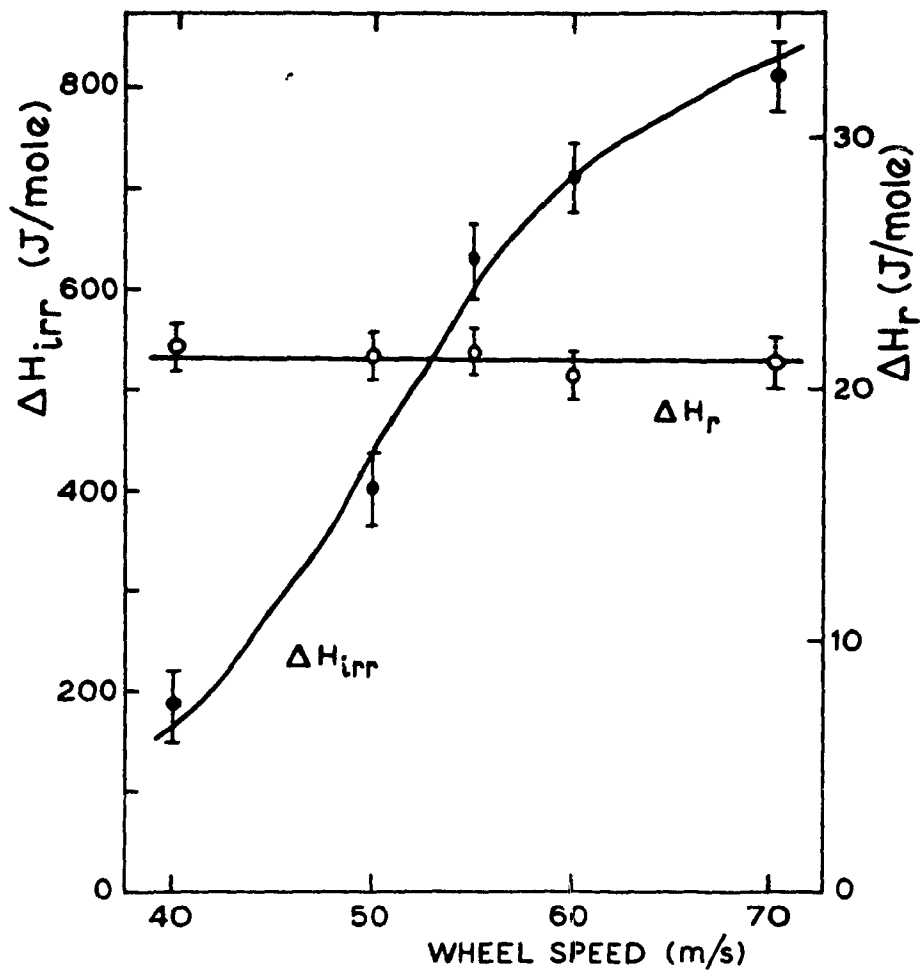


Figure 3.5: Irreversible and reversible relaxation enthalpies as a function of quench rate for  $Fe_{82.5}B_{17.5}$ . For  $\Delta H_{rev}$  the samples were annealed at 500 K for 1 h.

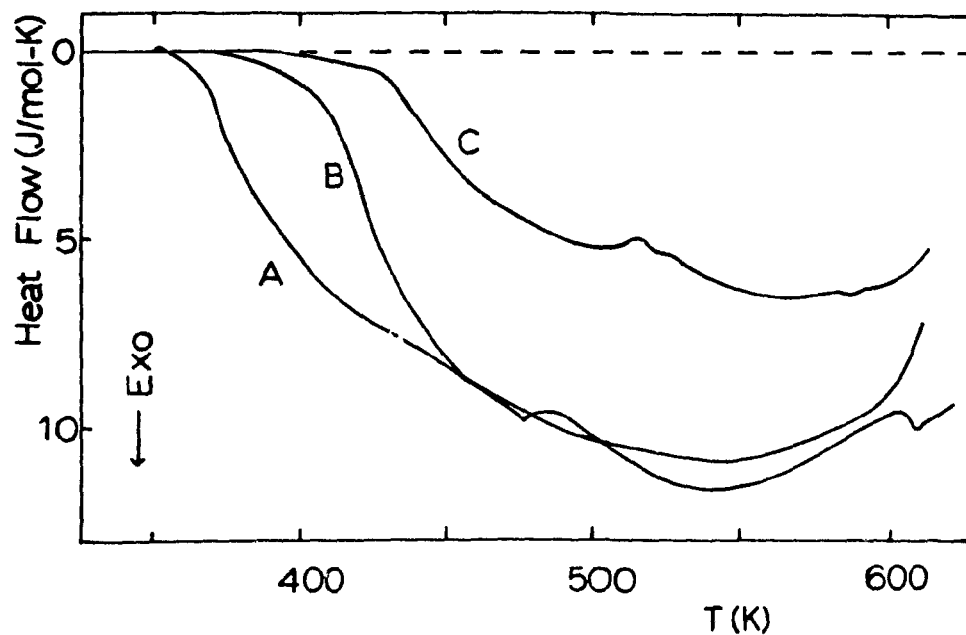


Figure 3.6: Dependence of irreversible relaxation on the method of amorphization. The DSC scans show the irreversible relaxation in  $\text{Ni}_{33}\text{Zr}_{66}$ : (A) mechanically alloyed, just after ball-milling; (B) mechanically alloyed, after storing at room temperature for three months; (C) melt spun.

the large number of defects introduced by the ball milling process. The onset temperature of the exotherm is so low that the alloy may be effectively annealed at room temperature; a repeated measurement a few months later on part of the same sample shows that the onset has moved by about 50 K to higher temperatures. A melt-spun glass of the same composition shows the onset of irreversible relaxation at even higher temperature and in general a smaller exotherm.

For constant preparation conditions, irreversible relaxation depends only very little on composition (see R. Brüning, 1986 [53]). Thus, as one would expect, irreversible relaxation is not an intrinsic property of the glass, but dependent on its thermal history.

### 3.2.3 Reversible Relaxation

The change induced by annealing a sample previously prepared in the reference state appears in scanning calorimetry as an endotherm which begins above the annealing temperature  $T_a$ . Such measurements have been reported first by Chen for Fe-Ni metalloid glasses (Chen, 1981 [8]), as well as extensive measurements on the glass  $\text{Pd}_{48}\text{Ni}_{32}\text{P}_{20}$  [78]. Other measurements have been made by Inoue *et al.* [79] on Cu-Zr glasses, Suzuki and Shingu on PdAuSi glasses [80] and Brüning on FeNiBSi glasses [20,53].

Several steps are involved in measuring reversible enthalpy changes by DSC. In what follows the procedure of measurement that was adopted here is described. We assume that, like for  $\text{Pd}_{40}\text{Ni}_{40}\text{P}_{20}$  the glass may be heated to above  $T_g$  without crystallizing it. If that it is not the case, the maximum temperature that the sample is heated to is a suitable temperature below  $T_x$ .

1. The glass is brought to the reference state by heating it to above  $T_g$ , and then cooling it at 320 K/min to room temperature.
2. The sample is heated to the annealing temperature  $T_a$ , and it is held at that temperature for the annealing time  $t_a$ .

3. The glass is cooled to room temperature at 320 K/min.
4. The heat flow is measured while the glass is heated to above  $T_g$  at 40 K/min.
5. The glass is cooled to room temperature at 320 K/min. The sample has been brought back to the reference state.
6. The heat flow is measured while the glass is heated to above  $T_g$  at 40 K/min. This provides the background measurement which is the sum of the baseline of the calorimeter and the heat flow of the sample in the reference state.
7. The glass is cooled to room temperature at 320 K/min.
8. The background heat flow (step 6) is subtracted from the heat flow of the annealed sample (step 4), which gives the difference in heat flow caused by the annealing procedure.
9. Another measurement may be made by repeating the procedure from step 2 onwards, since the sample is again in the reference state.

The susceptibility to reversible relaxation processes is an intrinsic property of the glass, and does not depend on the preparation conditions. This is obviously true for materials like  $\text{Pd}_{40}\text{Ni}_{40}\text{P}_{20}$  which may be brought to internal equilibrium by heating above  $T_g$ , which erases all traces of the thermal history. But it is also true for glasses that do not show a glass transition below the crystallization temperature, as may be seen in Figure 3.5 for  $\text{Fe}_{82.5}\text{B}_{17.5}$ : the relaxation enthalpy observed upon identical annealing conditions is independent of the quench rate used to prepare the glass.

Figure 3.4.b shows the changes in the specific heat induced by annealing a  $\text{Pd}_{40}\text{Ni}_{40}\text{P}_{20}$  sample in the reference state for  $\approx 20$  h at various temperatures. These changes are reversible, and the onset of the signal is seen only when the sample is heated for the first time above the annealing temperature  $T_a$ .<sup>4</sup> A temperature scan

---

<sup>4</sup>In the case of the measurements on the very stable glass  $\text{Pd}_{40}\text{Ni}_{40}\text{P}_{20}$  we have to be more

that follows a low temperature anneal (below  $\approx 470$  K) shows an endotherm which is about 120 K wide. For higher annealing temperature the endotherm is sharper and stops at 620 K, the temperature where the system reaches internal equilibrium at a heating rate of 40 K/min. This effect has already observed by Chen [78].

The time and temperature dependence of reversible relaxation in  $\text{Pd}_{40}\text{Ni}_{40}\text{P}_{20}$  are illustrated in Figure 3.7, which shows the total reversible enthalpy change with respect to the reference state for various annealing temperatures on a logarithmic time scale. It can be seen clearly that annealing above 550 K, close to  $T_g$ , allows the sample to come to internal equilibrium at  $T_a$  on experimental time scales. The maximum enthalpy change decreases upon annealing above 550 K since the equilibrium state at those temperature becomes closer to the reference state. On the other hand kinetics are more favorable at high temperatures, causing the curves to cross each other.

The activation energies determined by measuring the dependence of the endothermic peak on the scan rate are given in Table 3.1 for the annealing temperature 450 and 545 K. They agree well with previous data [78]. For 450 K the values of  $\nu_0$  of  $2 \times 10^{11} \text{ s}^{-1}$  indicates that reversible relaxation induced by low temperature annealing is well described as an activated process, implying local, non-cooperative changes. This is supported by the order of reaction (see Section 3.2.1), which is close to unity (Brüning, 1986 [53] and Brüning *et al.*, 1987 [20]). Furthermore it has been shown by two different methods that the activation energies for the endothermic precise in the definition of irreversible and reversible relaxation. Annealing near or above  $T_g$  is possible without causing the sample to crystallize. "Irreversible" means here changes that can only be restored by a heat and quench cycle similar to the original manufacturing conditions, and "reversible" to changes induced by annealing below  $T_g$ . One might consider it tautological to apply the term "reversible" to processes that only may be reversed by bringing the glass to internal equilibrium. Prior convention did not consider these cases, since most glasses crystallize upon annealing close to  $T_g$  and implicitly used "reversible" only for processes which may be reversed below  $T_g$ . In the present case this would restrict us to annealing temperatures at or below 520 K. However all effects are a smooth function of annealing temperature, and such a restriction is artificial, which justifies the use of "reversible" as defined above.

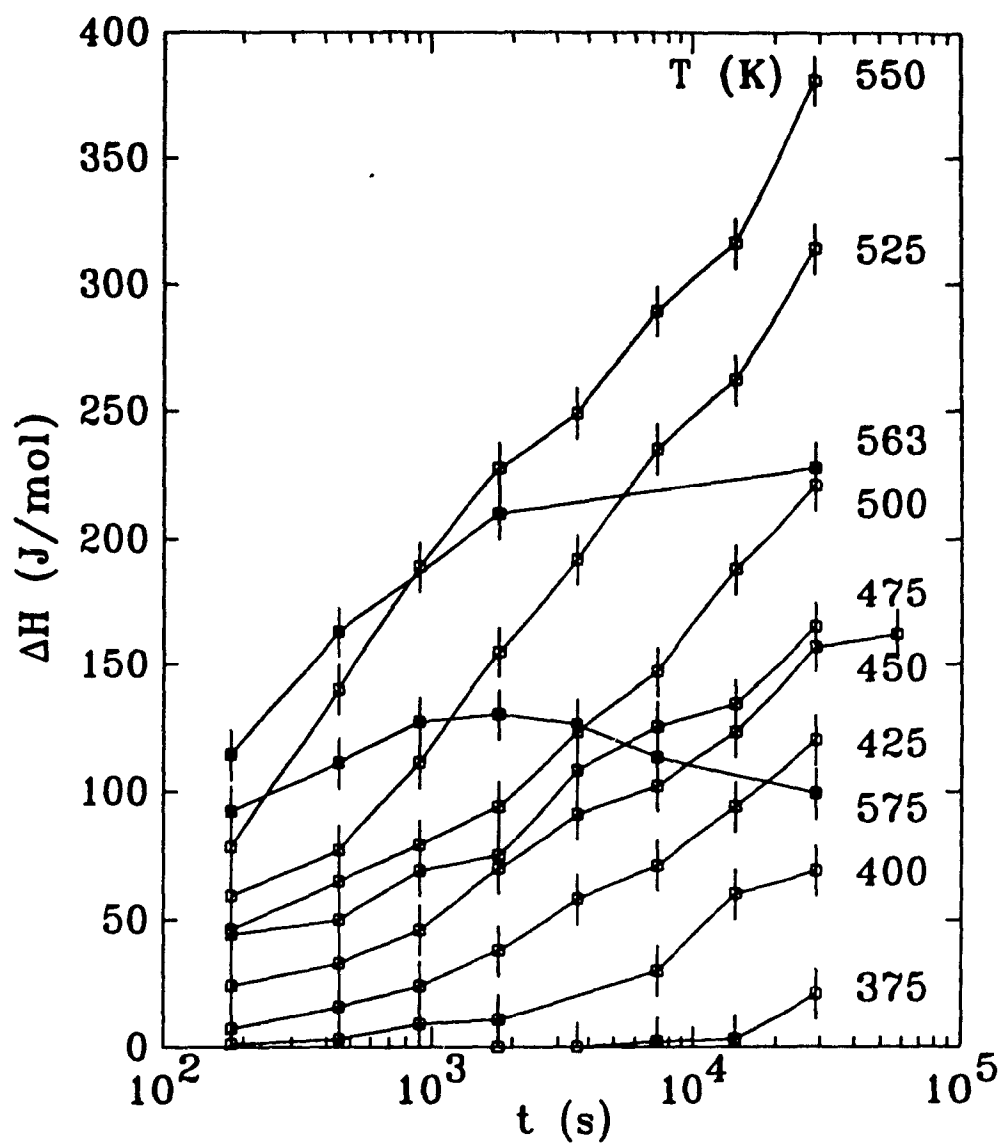


Figure 3.7: Reversible enthalpy change as a function of  $T_a$  and  $t_a$ . Note that  $\Delta H_{ref}$  saturates for  $T_a > 550$  K, showing that the sample reaches internal equilibrium during the experiment.

and the exothermic part of the reversible relaxation cycle agree (Chen, 1981 [78], Brüning, 1986 [20,53]).

Since we may assume localized structural changes as the origin of low temperature reversible relaxation, we can go one step further. Upon heating the glass the endothermic part of the reversible relaxation cycle occurs, because local structural changes occur which take up energy according to Boltzmann statistics. Furthermore the glass reaches internal equilibrium with respect to these structural degrees of freedom, since the endotherm ends before  $T_g$ . The energy taken up by each degree of freedom has to be of the order of  $k_B T$  for a process to be reversible at that temperature. A more careful estimate shows it has to be between  $k_B T$  and  $4k_B T$  (R. Brüning, [20,53]). In combination with the total enthalpy change one may estimate that there is typically one structural change for every 50 atoms, which again is consistent with a picture of localized structural changes.

The situation is quite different for the reversible structural changes close to  $T_g$ . The trial frequency obtained from the heating rate dependence of the endotherm near  $T_g$  shows an even higher value of  $\nu_0$  than for the glass transition (Table 3.1). During the anneal the structure of the glass is optimized, so that the glass finds itself in a deeper local minimum of the free energy than the unannealed glass. This enhances the hysteresis at  $T_g$ , as discussed above, and the transition between the glass and the supercooled liquid is more abrupt. Together, those results imply that reversible changes at high temperatures must be highly cooperative atomic processes rather than localized transitions.

We now turn to the composition dependence of reversible relaxation. In what follows we will only be concerned with the effects of low temperature annealing, since the alloys under consideration may not be heated to above  $T_g$  without crystallization. It was already mentioned above that the susceptibility to reversible relaxation is an intrinsic property of the glass. By studying its composition dependence, it is possible to obtain some qualitative information about the nature of structural relaxation processes. In metallic glasses that contain metalloids, such as  $\text{Pd}_{40}\text{Ni}_{40}\text{P}_{20}$ , reversible

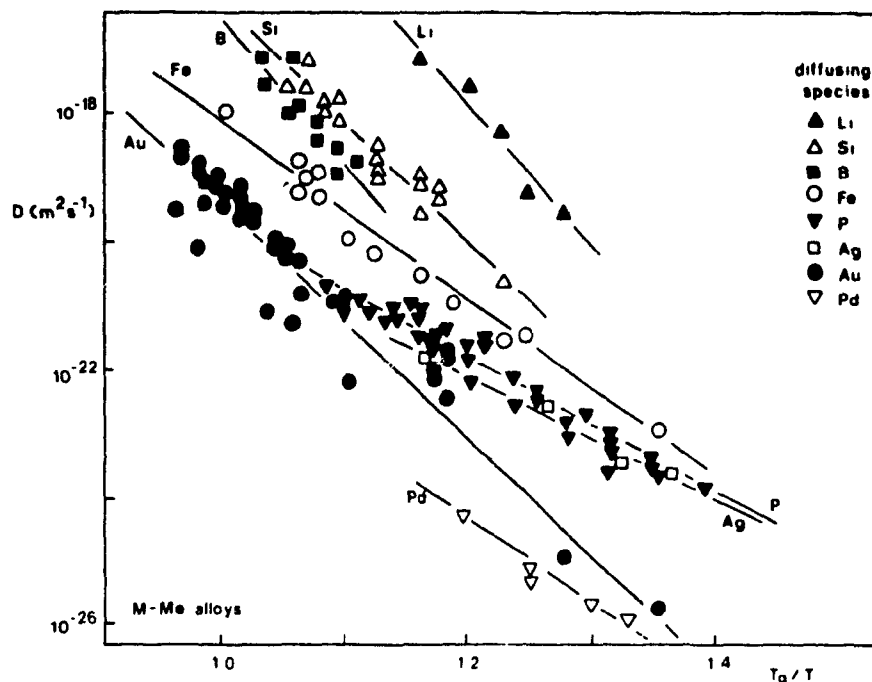


Figure 3.8: Arrhenius graph of measured diffusion coefficients in metal-metalloid amorphous alloys (reproduced from [81]). The temperature is normalized with the glass transition temperature.

relaxation increases monotonically with the concentration of the more mobile atom. An example is the system  $(\text{Fe}_{1-x}\text{Ni}_x)_{80}\text{B}_{10}\text{Si}_{10}$ , where nickel most likely diffuses faster than iron. Unfortunately no direct data on nickel diffusion are available to verify this assumption (see Figure 3.8, which shows data that have been compiled by Cantor and Cahn [81]). CSRO does not seem to have any influence on reversible relaxation in this glass, since a maximum of the effect near the composition  $\text{Fe}_{40}\text{Ni}_{40}\text{B}_{20}$  would then be expected [20,53].

In fact the simplest characterization of reversible relaxation within all metal-metalloid alloy systems is a scaling with the glass transition temperature  $T_g$ . This is clearly illustrated in Figure 3.9 where we plot the maximum specific heat,  $\Delta C_p^{max}$ , as a function of  $T_a/T_x$ . Relaxation, glass transition and crystallization are processes that all depend on interatomic diffusion. It can be expected that rescaling the temperatures in such a way should cancel the effects of diffusion controlled kinetics.

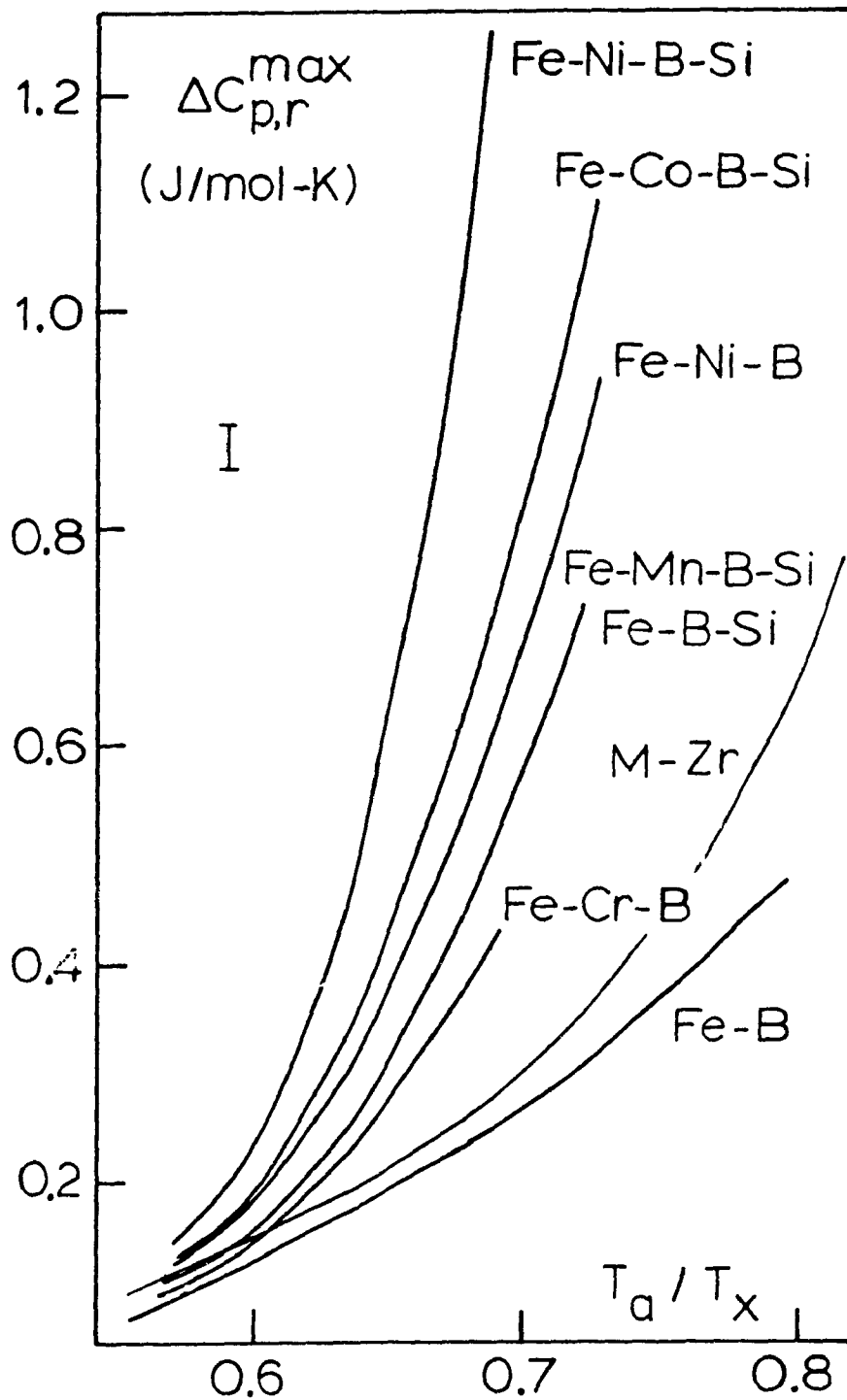


Figure 3.9: Reversible relaxation in metal-metalloid and binary metal-metal glasses ( $M \equiv \text{Cu, Ni, Fe}$ ). For each sample system, such as  $(\text{Fe}_{1-x}\text{Ni}_x)_{80}\text{B}_{10}\text{Si}_{10}$ , the reversible change is independent of composition and annealing temperature if the annealing temperature is scaled with the crystallization temperature (see also [20]).

Thus the susceptibility to reversible relaxation can be more directly compared between different glasses. It is apparent that within a specific alloy system, such as  $(\text{Fe}_{1-x}\text{Ni}_x)_{80}\text{B}_{10}\text{Si}_{10}$ , reversible relaxation is independent of composition. This result suggests that in metal-metalloid glasses, CSRO effects are outweighed by diffusion effects. Boron and in particular silicon diffuse very easily in metalloid glasses (see Figure 3.8).

Very similar results are found for binary metallic glasses of the type  $\text{Cu}_{100-x}\text{Zr}_x$ . In fact these glasses show only a small change with composition, and the overall effect is comparable with that in  $\text{Fe}_{100-x}\text{B}_x$  (see Figure 3.9).

However, the situation changes rather dramatically when we examine ternary glasses  $(\text{M}^a_{1-x}\text{M}^b_x)_{33}\text{Zr}_{67}$ ,  $\text{M}^a, \text{M}^b = \text{Fe}, \text{Co}, \text{Ni}, \text{Cu}$ . These alloys exhibit a very pronounced maximum as a function of composition, as shown in Figure 3.10. The crystallization temperature varies much less, for example between 655 K and 678 K for Fe-Ni-Zr. Also other physical parameters, like electrical resistivity and superconducting transition temperature are approximately constant. It has been verified by x-ray diffraction that the samples did not crystallize during the measurements, which shows that the maximum is not an artifact. From this we conclude that this behavior is intrinsic to the thermal relaxation process.

The data may be described by a linear extrapolation between the end points together with a term proportional to  $x(1-x)$ . One should expect this from the configuration entropy contribution from changes in CSRO. The term represents the number of unequal nearest neighbor atoms, which can potentially switch their places - which are distinguishable in the glass - and thus give rise to a change in the enthalpy. The fit is shown in Figure 3.10.

From this discussion a condition for CSRO changes becomes apparent. Two atoms can only exchange their places if they are similar in size. If the two atoms are quite different, such as example Ni with a radius of 1.24 Å and Zr with a radius of 1.60 Å, few changes in the structure are to be expected, as observed in the binary Ni-Zr glass. The 3-d elements Fe, Co, Ni and Cu have similar atomic radii, so that

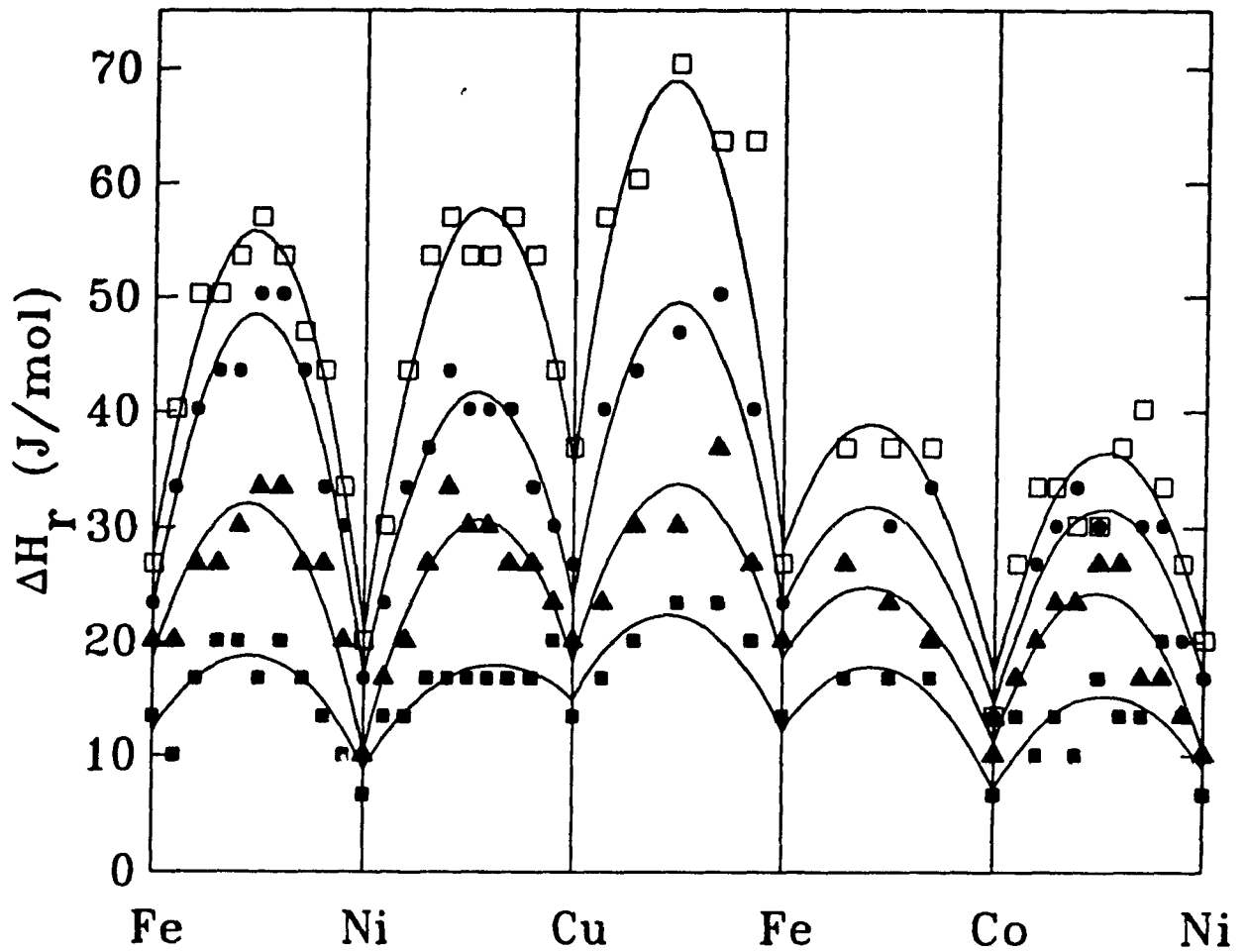


Figure 3.10: Composition dependence of reversible relaxation in ternary metal-metal glasses. The composition varies according to  $(M^a_{1-x}M^b_x)_{33}Zr_{67}$  between each pair of vertical lines, where  $M^a, M^b = Fe, Co, Ni, Cu$ . The symbols correspond to different annealing temperatures:  $\blacksquare T_a = 440$  K,  $\blacktriangle T_a = 460$  K,  $\bullet T_a = 480$  K and  $\square T_a = 500$  K. The annealing time was 1 h for all data points. The errors are  $\pm 3$  J/mol - K. The lines are best fits of parabolas to the data points.

a combination of two such elements promotes interatomic exchanges. Furthermore, the chemical rearrangement of the two atoms would also affect the topological short range order (TSRO), so that changes in CSRO and TSRO could not be separated any more. This shows that the separation of structural relaxation effects into processes which change either CSRO or TSRO, invoked often without further justification [13,29,30], is only applicable in selected cases.

It is worth noting here another difference between metal-metal and metal-metalloid glasses. Atomic order is stronger and of longer range in metal-metalloid systems than in metal-metal glasses. This is in particular true for the chemical order, as a comparison of the partial radial distribution functions shows. In metal-metalloid glasses no metalloid atoms are nearest neighbors (see Lamparter and Steeb, 1984 [82]), while there is no such preference of nearest neighbor atoms in metal-metal glasses (see Maret *et al.*, 1987 [83]). This implies that metal-metal glasses have more degrees of freedom in the arrangement of nearest neighbor atoms, and a change may occur within the nearest neighbor shell by the displacement of atoms over a very small distance. Therefore the diffusivity of the atoms is not a serious restriction to reversible relaxation, and instead the number of unlike permutations of the nearest neighbor atoms may come into play. In metal-metalloid glasses there are fewer degrees of freedom for the choice of the nearest neighbor atoms, and atoms have to diffuse over longer distances to change the structure. Thus the diffusivity of the atoms is more likely to limit the magnitude of reversible relaxation, which masks the effects of chemical reordering.

### 3.2.4 Summary of the DSC Results

We have seen that the different structural relaxation processes can be characterized by the temperature dependence and the shape of the enthalpy changes that accompany them. Irreversible structural relaxation, reversible structural relaxation induced by annealing at low temperatures ( $\lesssim 470$  K for  $\text{Pd}_{40}\text{Ni}_{40}\text{P}_{20}$ ) and reversible structural relaxation induced by annealing close to  $T_g$  can be clearly distinguished

from each other, and the latter two appear even more different when the corresponding kinetics are taken into consideration. This enables us to use the calorimetric results as a point of reference and a calibrant for the direct measurements of the microscopic structure, which will be discussed in the remainder of this Chapter. All the measurements on the microscopic structure will be on  $\text{Pd}_{40}\text{Ni}_{40}\text{P}_{20}$ , and it must therefore be stressed that they may only be fully generalized to glasses of this type.

In general the susceptibility to reversible relaxation depends on the diffusivity of the elements making up the glass, although in ternary metal-only glasses evidence of configurational effects is seen.

### 3.3 X-Ray Diffraction

$\text{Pd}_{40}\text{Ni}_{40}\text{P}_{20}$  was selected as the system for the study of the microscopic aspects of structural relaxation by x-ray diffraction, for the following reasons:

- Under given annealing conditions the calorimetric signals are larger than in most other metallic glasses, which suggests that the atomic displacements occurring during relaxation are larger.
- The glass is very stable so that relaxation processes can be taken much further without risk of crystallization. This is important because even small amounts of crystalline contaminants have a severe effect on structural relaxation [20,53]; furthermore they would also tend to dominate the x-ray diffraction pattern.
- The x-ray signal can be approximated by a single structure factor.

The last point follows because the high atomic scattering factors for palladium and nickel ensure that the average structure factor is mainly determined in our sample by metal-metal correlations, which in the relevant region contribute 89 % of the total signal. (Metal-metalloid correlations contribute 10 % and metalloid-metalloid correlations less than 1 %.) Furthermore the two metal atoms are similar both

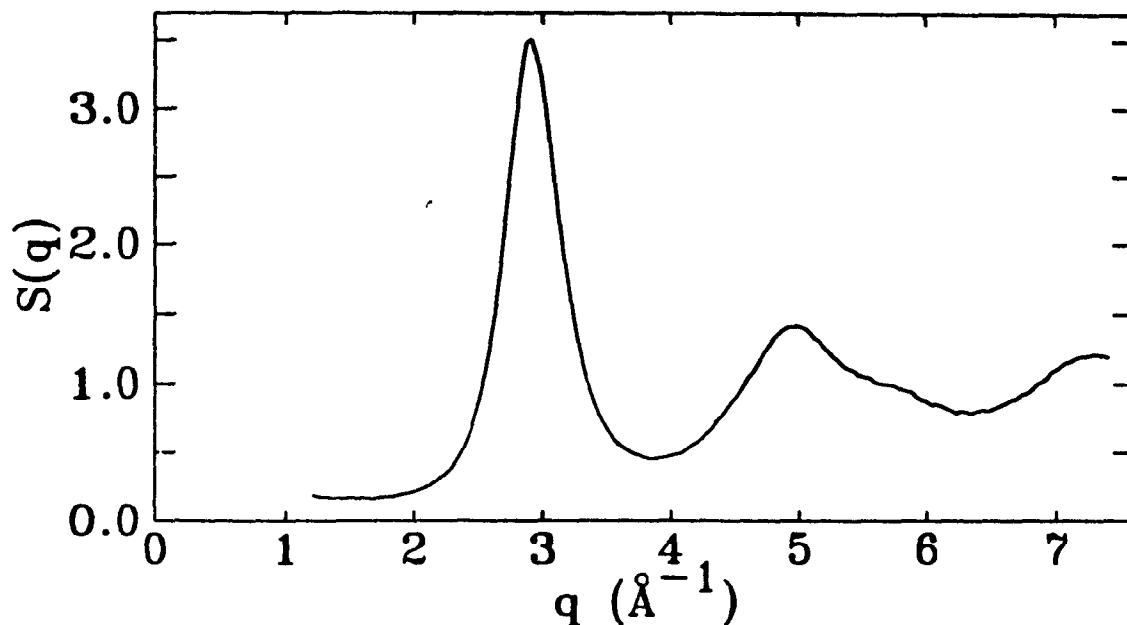


Figure 3.11: Structure factor of  $\text{Pd}_{40}\text{Ni}_{40}\text{P}_{20}$ . The upper limit of  $q$  is determined by the the wavelength of the  $\text{CuK}\alpha$  radiation.

chemically and in size, and so may to a fair approximation be treated as the same atom. Thus in the analysis that follows we assume that the observed  $S(q)$  comes from the radial distribution function  $\rho(r)$  of a single atom type.

The diffractometer designed to fulfill the specific requirements of the measurement was described in Section 2.5.1. The procedure to obtain the structure factor from the experimental data and to calculate the radial distribution function was described in Section 2.5.2. In what follows the data are presented (Section 3.3.1), followed by the description and application of the method developed to analyze the structural changes (Section 3.3.2).

### 3.3.1 The Data

The structure factor  $S(q)$  of a sample in the reference state is shown in Figure 3.11. Figure 3.12 gives the radial distribution function,  $\rho(r)$ , and the average density,  $\rho_0$ , weighted with  $4\pi r^2$ .

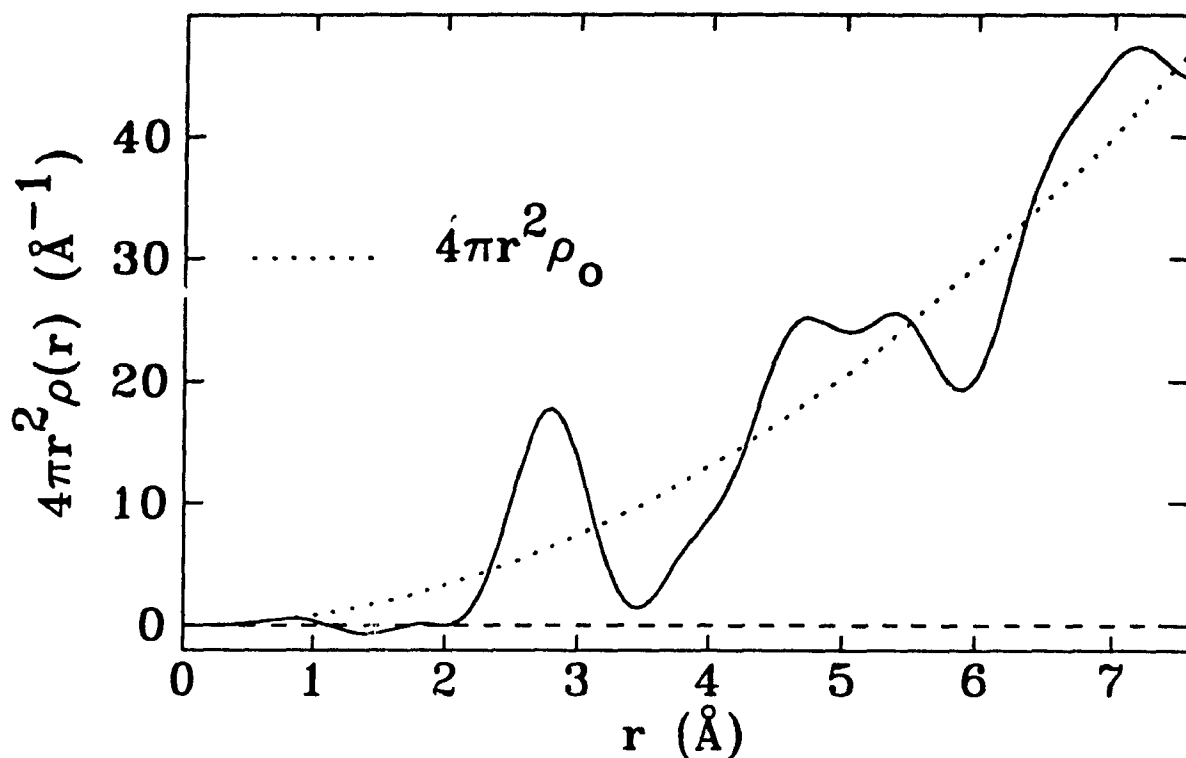


Figure 3.12: Radial distribution function of  $\text{Pd}_{40}\text{Ni}_{40}\text{P}_{20}$ . The oscillations in below  $r = 2 \text{ \AA}$  are due to the cutoff in  $S(q)$  at  $7.4 \text{ \AA}^{-1}$ .

Figure 3.13 shows the changes in the structure factor sample induced by different annealing processes. Since all the changes in  $S(q)$  are small compared to  $S(q)$  itself (typically of the order of 1%) they are shown here as differences, the structure factor of reference state,  $S_r(q)$ , being subtracted. The structure factor of the reference state is given for comparison in Figure 3.13.a. The changes of  $S(q)$  due to irreversible relaxation are shown in Figure 3.13.b, and Figure 3.13.c gives the effects of reversible relaxation. The samples were brought to the reference state, and then annealed for 20 h at the temperatures indicated. These changes in the structure factor can be completely reversed by reheating the sample to above  $T_g$ , which was used as a measure of the reproducibility of the data (Figure 3.14). It should be stressed that, so far as we know, these figures represent the first observation by x-ray diffraction of reversible structural changes in metallic glasses.

Some conclusions can be drawn directly from the data without further analysis. The structure factor becomes narrower as the as-made sample is annealed

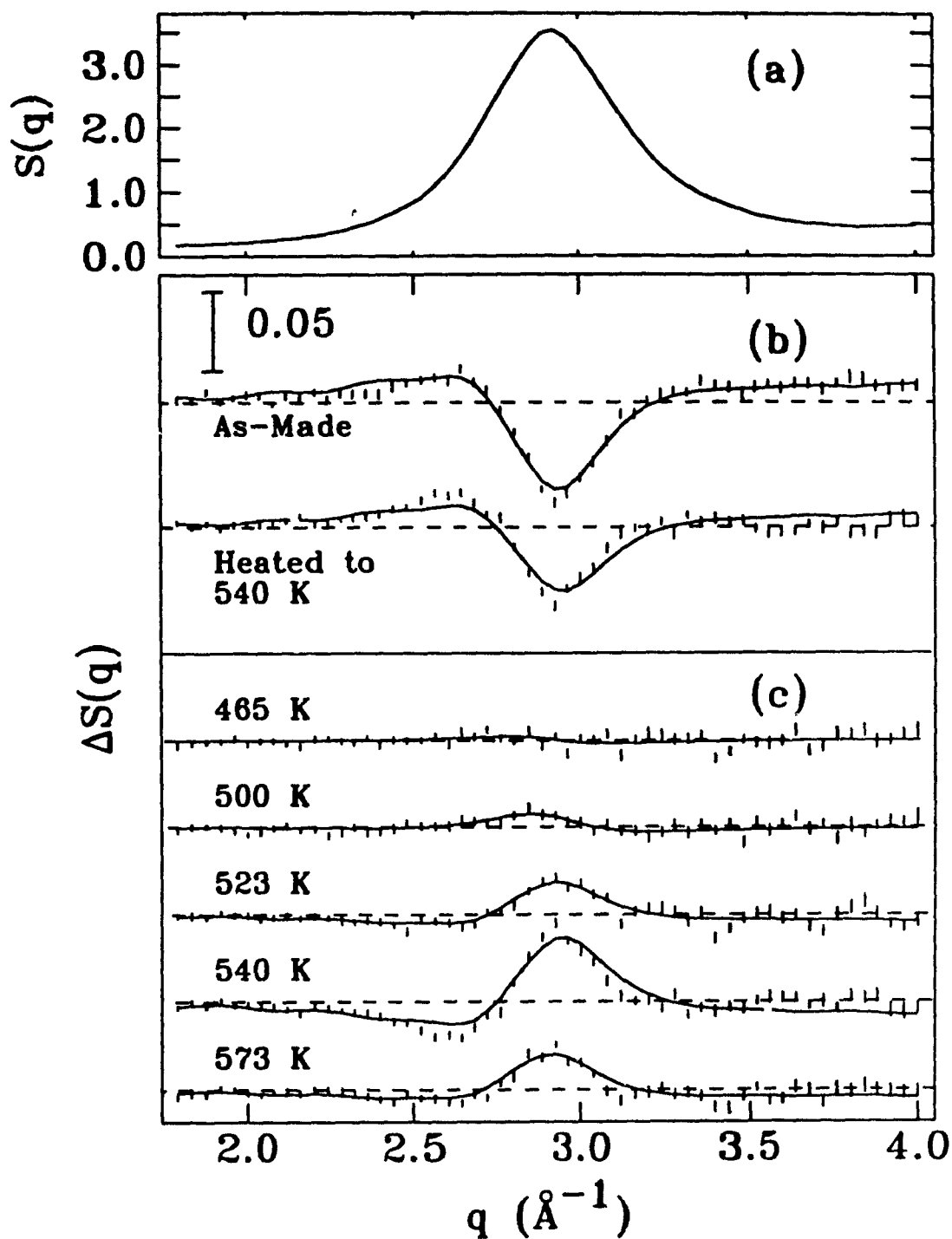


Figure 3.13: Irreversible and reversible changes in  $S(q)$ . The changes of  $S(q)$  are shown as differences with the structure factor of the reference state,  $S_r(q)$ , subtracted. (a) the structure factor of the reference state; (b) irreversible changes; (c) reversible changes, induced by annealing for 20 h at the temperatures indicated. The error bars were calculated from the variations in the signal between the subsamples (see Section 2.5.1). The solid lines show the fit to the changes of  $S(q)$  (see Section 3.3.2).

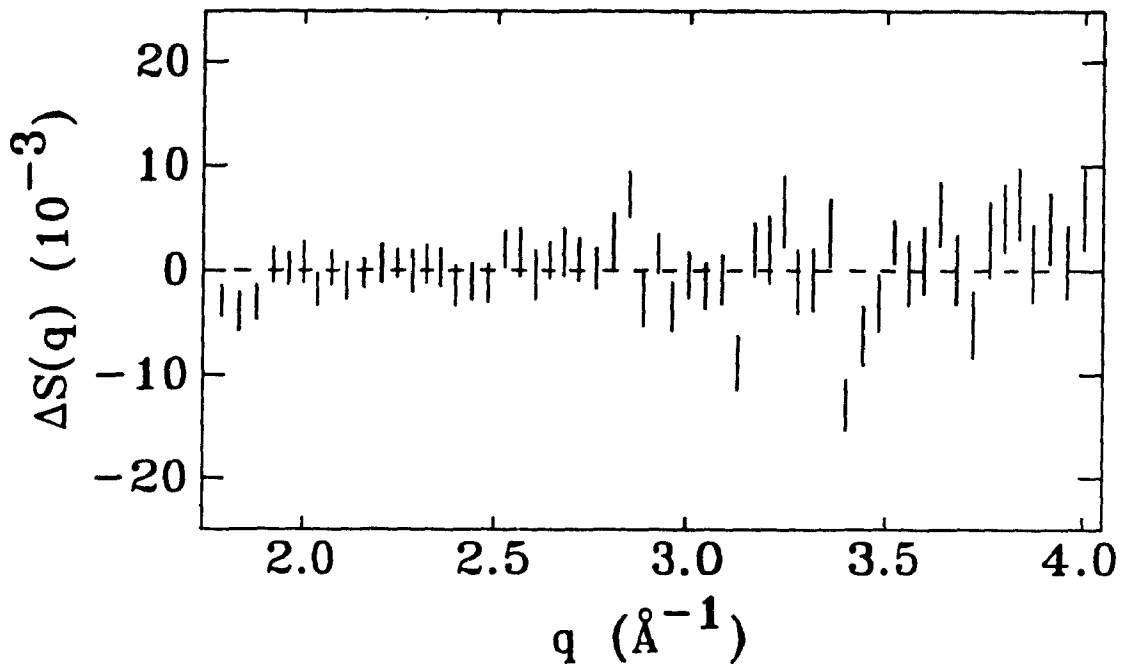


Figure 3.14: Reversibility of structural changes measured by x-ray diffraction. The structure factor of a sample in the reference state was measured before the sample was annealed at 540 K. The difference between these two structure factors is shown in Figure 3.13.c. The structure factor was measured again after the sample was then heated to 620 K, and the structure factor of the sample in the initial reference state was subtracted. The result is shown here. The initial sample state has been entirely recovered. Residual variations indicate the reproducibility of the data.

and thus brought to the reference state (Figure 3.13.b), which indicates that the atomic ordering increases during irreversible relaxation. The narrowing continues as the sample is annealed further (reversible relaxation, Figure 3.13.c). However, no effects of annealing the reference state below 500 K may be seen, even though quite substantial enthalpy changes (see Figure 3.4.b) and changes of the Mössbauer spectra, discussed in Section 3.4.1, are still visible. Hence we may deduce that the processes involved in low temperature reversible relaxation do not affect the radial distribution of the metal atoms. This agrees well with the assumption of localized structural changes deduced from the calorimetric results above. On the other hand, irreversible relaxation, as well as reversible relaxation caused by annealing close to  $T_g$ , changes the distribution of the metal atoms.

The data on irreversible relaxation are very similar in their appearance to the results of Egami [31], Waseda and Egami [32] Chason *et al* [34] and Schaal *et al.* [35] on glasses of similar composition. Some of these results are reprinted in the Figures 3.15, 3.16 and 3.17 to allow a direct comparison with the results obtained here. The maximum change of the structure factor measured by Egami is 2.5%, Waseda and Egami found 2.2%, Chason *et al.* found 1.0%, all of which are similar to the change of 1.8% seen here; because irreversible relaxation depends on the preparation conditions, the amounts may vary. Mizoguchi *et al* [33] obtained changes in the  $S(q)$  of the order of 4.2% for MgZn. Most of the changes in the structure factor, which were measured by neutron diffraction by Schaal *et al.* are much larger. The changes that they observed at the lowest temperature and short times are consistent with the results mentioned above. The other measurements were carried out by annealing close to or above the glass transition temperature, where no irreversible relaxation effects occur. Thus the large signals observed instead must be caused by the first stages of crystallization and cannot be compared to the data here. All of these measurements agree in so far as the most prominent change caused by irreversible relaxation is a decrease in the width of the first peak of  $S(q)$ ,  $\Delta S(q)$  has about half the width of  $S(q)$ . The only data that differ in this respect are the

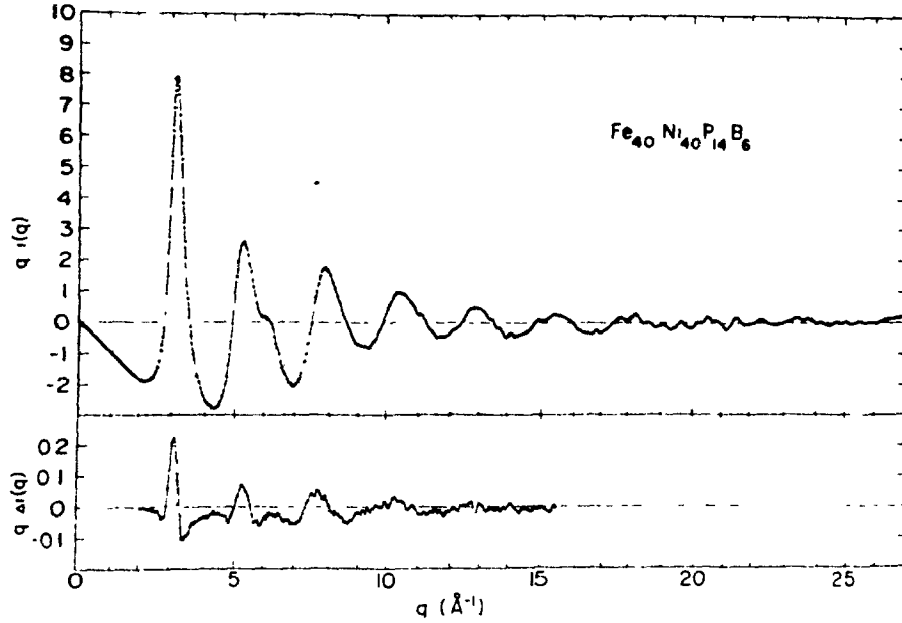


Figure 3.15: Irreversible change of the interference function of  $\text{Fe}_{40}\text{Ni}_{40}\text{P}_{14}\text{B}_6$  measured by Egami [31]. The interference function  $i(q)$  is related to the structure factor  $S(q)$  by:  $i(q) = S(q) - 1$ . The sample was annealed at 350 K for 30 min.

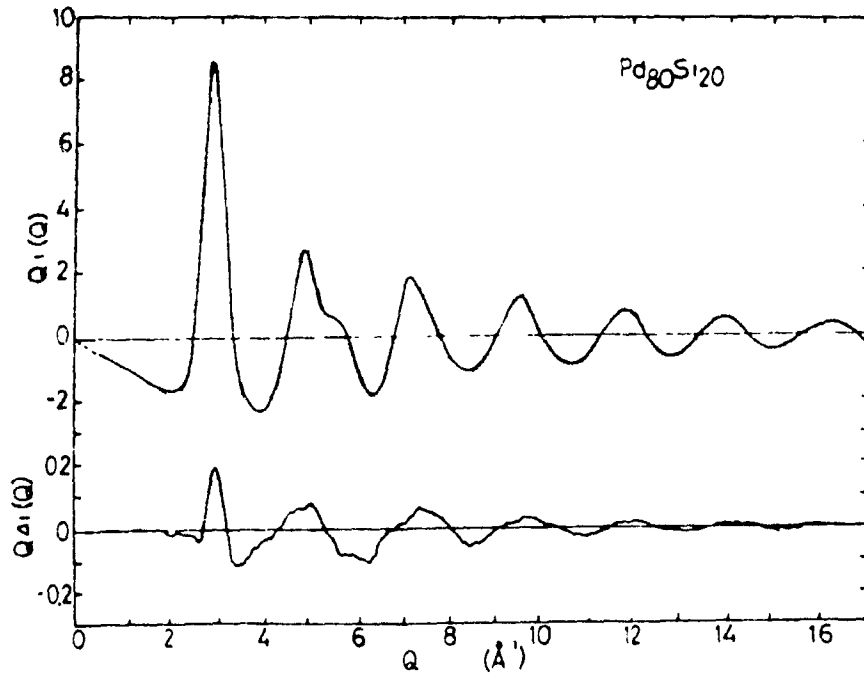


Figure 3.16: Irreversible change of the interference function of  $\text{Pd}_{80}\text{Si}_{20}$  measured by Waseda and Egami [32]. The sample was annealed at 270 K for 30 min.

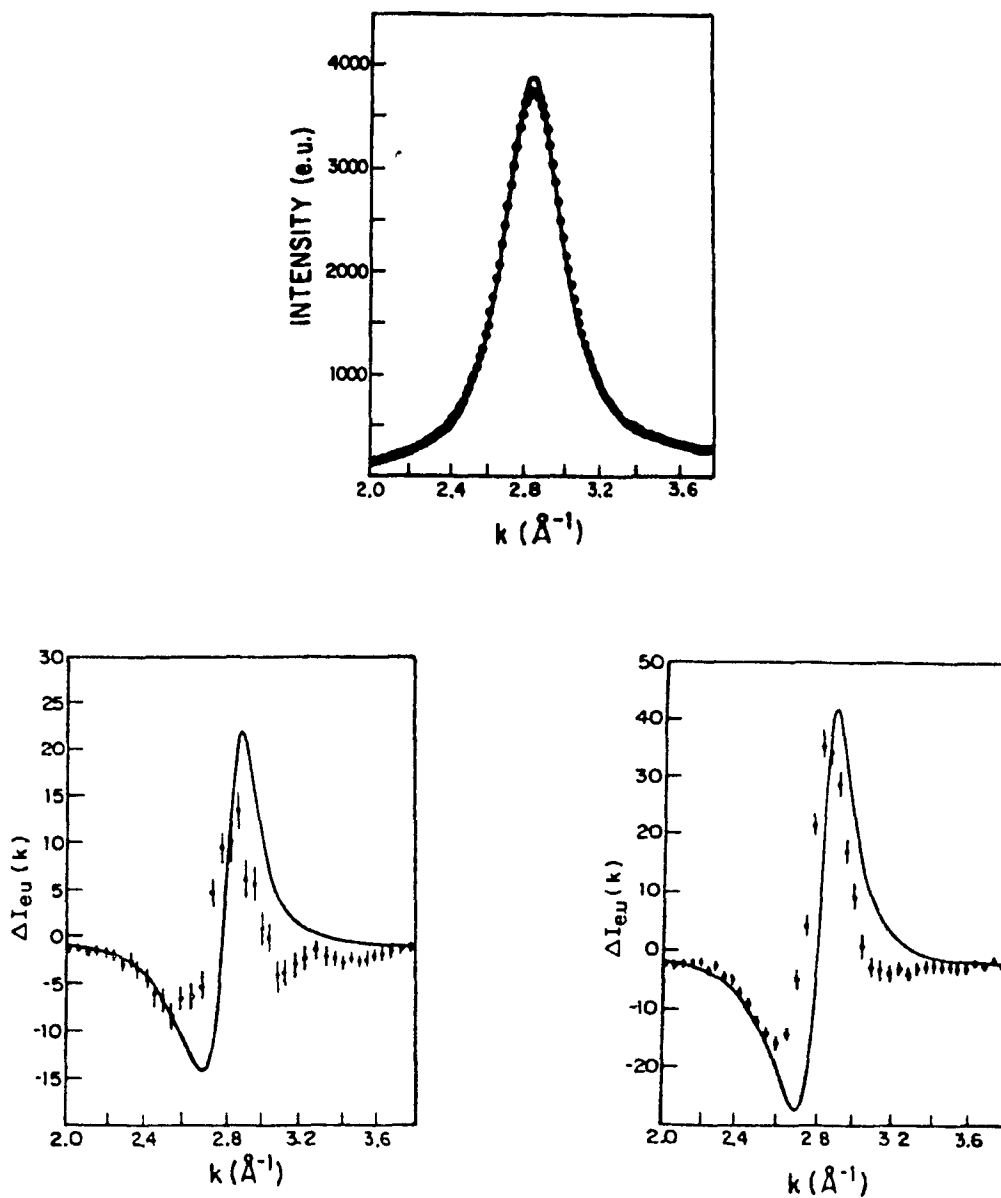


Figure 3.17: Irreversible changes of the distribution of the scattered intensity,  $\Delta I$ , from  $\text{Pd}_{82}\text{Si}_{18}$  measured by Chason *et al.* [34]. Note that  $k = q$ . Shown are the scattered intensity of the unannealed sample (top), the change induced by annealing for 15 min at 514 K (bottom left), and the change induced by annealing for 40 min at 539 K (bottom right). The solid lines represent a fit of the data to the Percus-Yevick model (see Section 3.3.2).

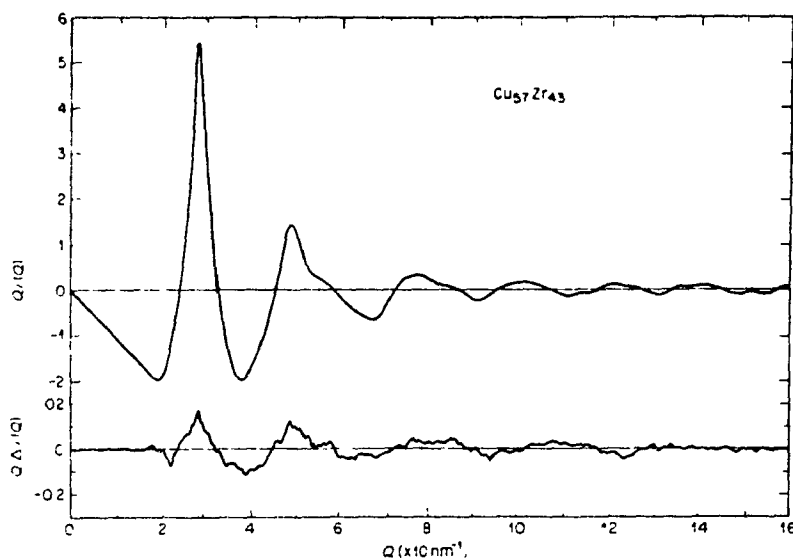


Figure 3.18: Irreversible change of the interference function of  $\text{Cu}_{57}\text{Zr}_{43}$  measured by Chen *et al.* [84]. The sample was annealed at 575 K for 50 min.

data obtained by Chen *et al.* on CuZr [84], who report a changes in the structure factor which are very similar to the structure factor itself: the amplitude of the oscillations in  $S(q)$  increased without a sharpening of the peaks. These data are shown in Figure 3.18. Possible reasons why this result is different will be discussed below.

### 3.3.2 Method of Analysis

Relating the experimentally determined  $S(q)$  to microscopic changes of structure requires modeling. Several models for structural changes have been developed. Chason *et al.* [34] in their analysis of irreversible changes in amorphous  $\text{Pd}_{82}\text{Si}_{18}$  used the Percus-Yevick hard sphere model [85] to produce analytical expressions for the effects of structural relaxation. This approach, which describes mainly changes of density, has some deficiencies, as can be seen in Figure 3.17. Srolovitz *et al.* (1981) [86] proposed an expression relating irreversible changes in the reduced radial distribution  $G(r) = 4\pi[\rho(r) - \rho_0]$  to the second derivative of this function, i.e.  $\Delta G(r) \propto \partial^2 G(r) / \partial r^2$ . This functional form successfully reproduced the experimen-

tal data obtained by Egami [31], and later Mizoguchi *et al.* [33] analyzed their data on amorphous  $\text{Mg}_{70}\text{Zn}_{30}$  with this expression. Suzuki *et al.* [87] (1987) gave an expression for changes of the structure factor as part of an analysis of changes induced by anisotropic stress. We shall see that it has the form that one would expect for a change in density alone.

In what follows we derive expressions for two independent contributions to changes in  $S(q)$ . The first term describes the result of a change in density without any change in the atomic order. The second term leaves the density constant, but modifies the atomic order. While the first term is exactly defined, there are many ways to construct an expression for the latter. Here we start from a quite general procedure, which then will be refined with respect to the experimental data. The main idea is to base the possible changes of  $S(q)$  on the information already contained in  $S(q)$  itself, *i.e.* to calculate changes of the atomic positions based on where the atoms are initially.

### Change in Density

A change of density without a change in the relative arrangements of the atoms may be accomplished by changing the length scale from  $r$  to  $r(1 + \epsilon)$ . To see the effect of this change on the structure factor we observe that it is equivalent to changing  $q$  to  $q/(1 + \epsilon)$ . To first order in  $\epsilon$  this leads to a change in  $S(q)$  of  $\delta S_1(q)$  where

$$\delta S_1(q) = S(q/[1 + \epsilon]) - S(q) = q\epsilon \frac{dS}{dq} = -\frac{q}{3} \frac{dS}{dq} \frac{\delta\rho_0}{\rho_0} \quad (3.1)$$

with  $\delta\rho_0/\rho_0$  being the fractional change in density  $\rho_0 = \lim_{r \rightarrow \infty} \rho(r)$ .

This result can also be obtained by performing the more lengthy calculation in the radial domain. A change in length scale from  $r$  to  $(1 + \epsilon)r$  changes the radial distribution function from  $\rho(r)$  to  $\rho(r) + \delta\rho_1(r)$ , where

$$\int_{\tilde{r}=0}^r \rho(\tilde{r}) d^3\tilde{r} = \int_{\tilde{r}=0}^{(1+\epsilon)r} (\rho(\tilde{r}) + \delta\rho_1(\tilde{r})) d^3\tilde{r}$$

for all values of  $r$ . Differentiating this equation with respect to  $r$  and expanding to lowest order in  $\epsilon$  gives

$$\delta\rho_1(r) = -3\epsilon\rho(r) - \epsilon r \frac{d}{dr}\rho(r). \quad (3.2)$$

At large distances  $\rho(r) \rightarrow \rho_0$ , a constant, so that  $\delta\rho_0 = -3\epsilon\rho_0$ . This is substituted into Equation 2.1, which is the relation between  $S(q)$  and  $\rho(r)$ . The change,  $\delta S_1(q)$ , due to length rescaling is

$$\delta S_1(q) = \int_{r=0}^{\infty} 4\pi r^2 (\delta\rho_1(r) - \delta\rho_0) \frac{\sin(qr)}{qr} dr.$$

Substituting from Equation 3.2 and using the fact that away from the central scattering at small angles (see e.g. [60])

$$\int_{r=0}^{\infty} 4\pi r^2 \rho_0 \frac{\sin(qr)}{qr} dr = 0$$

we find

$$\delta S_1(q) = -4\pi\epsilon \int_{r=0}^{\infty} \frac{\sin(qr)}{qr} \frac{d}{dr} (r^3 \rho(r)) dr$$

which may be integrated by parts with a convergence factor and the Equation 2.1 to give the result in Equation 3.1.

One precaution is necessary at this point. We assume that the sample, or at least the changes, are isotropic. Suzuki *et al.* [87] showed that anisotropy introduced by annealing amorphous ribbons under tension can be detected by x-ray diffraction. Cahn *et al.* [11] reported anisotropic length changes during irreversible relaxation of amorphous ribbons, which shows that the preparation of the glass may give rise to anisotropy. For an anisotropic sample the structure factor depends on the direction of  $\vec{q}$ , and it should be written as  $S(\vec{q})$  [87]. Because in our case the scattering experiment was done in reflection geometry,  $\vec{q}$ , which represents the momentum transfer, was always perpendicular to the ribbon surface. This implies that it is impossible to determine from a single scattering measurement whether the changes in  $S(q)$  correspond to a real density change (*i.e.* isotropic strain), or just a change in the sample anisotropy. This is why we measured the density independently; the results will be compared in Section 3.3.3.

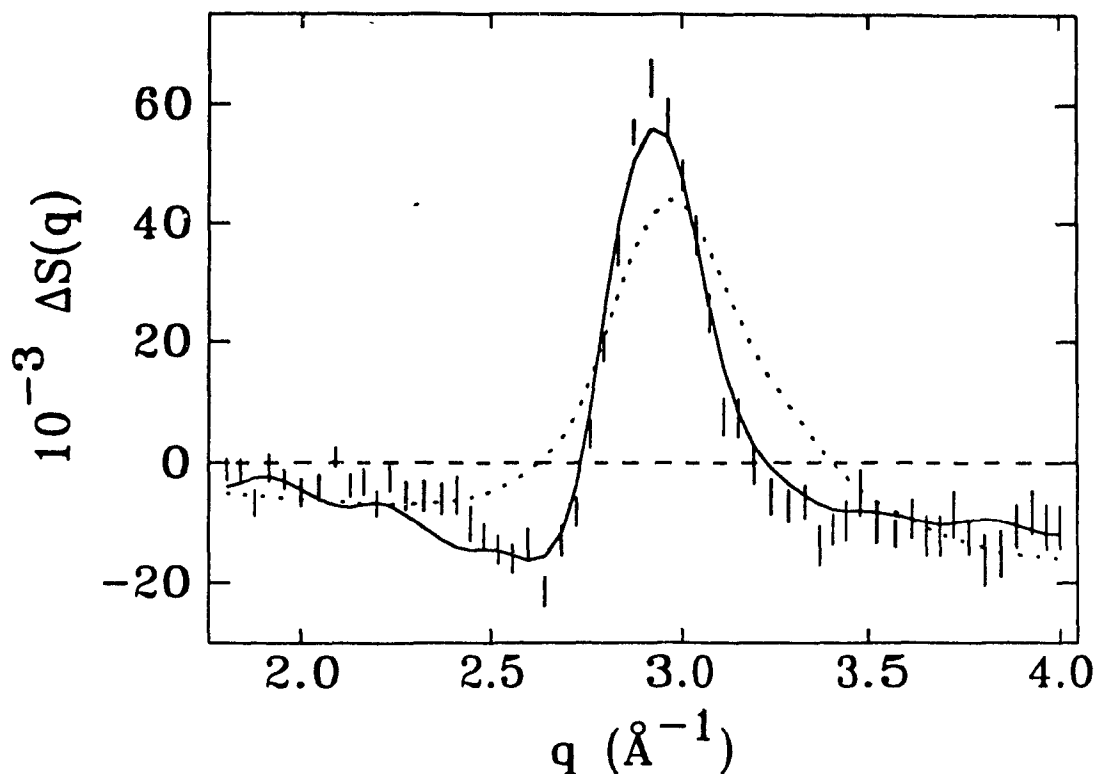


Figure 3.19: Fitting of the changes in the structure factor. The dotted line is the best fit using the form predicted by Equation 3.6. The solid line is the best fit using the form predicted by Equation 3.8, which follows the data very well.

### Change of Atomic Order

During reversible and irreversible structural relaxation the main change is a sharpening of the first peak of the structure factor (Figure 3.13 and Figure 3.19) which implies, since the first peak in  $S(q)$  represents the distribution of nearest neighbor distances, that the oscillations in the radial distribution function must become more regular and extend over longer distances.

Since we wish to obtain information about local structural processes, we will describe these changes by local displacements of atoms, with the constraint that the overall density of the glass is conserved.

To begin, it is easy to imagine how the order in a glass may decrease. (We see later how the resulting procedure can be inverted.) To increase the disorder, every

atom is displaced in a *random direction* by a *some random distance* less than  $\eta$ , the maximum distance by which the atoms are displaced during structural relaxation. This is the parameter which we want to determine by this analysis. This leads to a new radial distribution function,  $\rho_2(r)$ , which is the average of  $\rho(r)$  over the small spherical volume of radius  $\eta$  centered at  $\vec{r}$ :

$$\rho_2(\vec{r}) = \frac{\int_0^\eta \rho(\vec{r} + \vec{s}) d^3s}{\int_0^\eta d^3s} \quad (3.3)$$

where the integral is taken over the sphere. The averaging procedure results in a smoothing of  $\rho(r)$ , so that  $\rho(r)$  will increase at its minima and decrease at its maxima. Choosing polar coordinates  $(s, \theta, \phi)$  with the center at  $\vec{r}$  and the axes along  $\vec{r}$ , one can expand:

$$\rho(\vec{r} + \vec{s}) = \rho(|\vec{r} + \vec{s}|) = \rho(r) + \left( s \cos \theta + \frac{s^2 \sin^2 \theta}{2r} \right) \frac{d\rho}{dr} + \frac{s^2 \cos^2 \theta}{2} \frac{d^2\rho}{dr^2} + O(s^3).$$

By substituting this in Equation 3.3 and performing the integration one obtains:

$$\delta\rho_2(r) = \rho_2(r) - \rho(r) = \frac{\eta^2}{10r^2} \frac{d}{dr} \left( r^2 \frac{d\rho}{dr} \right) = \frac{\langle \eta^2 \rangle}{6r^2} \frac{d}{dr} \left( r^2 \frac{d\rho}{dr} \right), \quad (3.4)$$

where  $\langle \eta^2 \rangle$ , the mean square displacement of atoms in the sphere relative to the origin, is:

$$\langle \eta^2 \rangle = \int_0^\eta s^2 d^3s \left[ \int_0^\eta d^3s \right]^{-1} = \frac{3}{5} \eta^2.$$

Note that as  $r \rightarrow \infty$ ,  $\delta\rho_2 \rightarrow 0$  since  $d\rho/dr \rightarrow 0$ . This expression describes a smoothing out of  $\rho(r)$ . However, from a broadened  $\rho(r)$  the original unbroadened distribution may be reconstructed by inverting Equation 3.4:

$$\rho(r) = \rho_2(r) - \frac{\langle \eta^2 \rangle}{6r^2} \frac{d}{dr} \left( r^2 \frac{d\rho_2}{dr} \right),$$

where, as an approximation which is valid for  $\delta\rho_2 \ll \rho$ , the derivative  $d\rho/dr$  has been replaced by  $d\rho_2/dr$ . Therefore, if the changes are small, Equation 3.4 may also be used to describe an increase in atomic order simply by changing the sign of the right-hand side of Equation 3.4. By substituting into Equation 2.1 the change in

$S(q)$  can be determined:

$$\delta S_2(q) = \frac{4\pi}{6} \int_{r=0}^{\infty} \langle \eta^2 \rangle \frac{\sin(qr)}{qr} \frac{d}{dr} \left( r^2 \frac{d\rho}{dr} \right) dr. \quad (3.5)$$

Equation 3.5 may be integrated, again with convergence factors. The result is:

$$\delta S_2(q) = -\frac{1}{6} q^2 (S(q) - 1) \langle \eta^2 \rangle. \quad (3.6)$$

This form has been fitted to the measured change in  $S(q)$ . The best fit is shown by the dotted line in Figure 3.19. The fit is very poor, and the changes of  $S(q)$  predicted by Equation 3.6 are about twice as broad as in fact observed.

The reason why the simple model described so far fails to reproduce more closely the features of the data is that we neglected an important physical constraint in the relative motion of the atoms. We assumed that the relative motion of all atoms was independent of whether they were near or distant neighbors. However, distant neighbors have much more topological freedom to negotiate a change in their relative position than near neighbors, which tend to be displaced in the same direction and by similar distances so as to keep the interatomic spacing constant. As an illustration, one might think of the motion of particles which are embedded in a viscous liquid. When the liquid is stirred in some random way, distant particles move nearly independently, while the viscous forces correlate the motion of particles that are close together so that they move in the same direction. Egami already observed that the relative displacement of near neighbors is much smaller than that of more distant neighbors during irreversible structural relaxation [31].

In Equation 3.3,  $\eta$  has been introduced as the average strain of an atom measured relative to the position of the central atom,  $\vec{r}$ . To discuss the effect of correlations we have to take the displacement of the central atom into account. In a coordinate system that is fixed in space, the displacement of the atoms can be described by a strain field  $\vec{u}(\vec{r})$ . The effect of the correlation in the atomic motions is that  $\eta$  in the Equation 3.4 depends on distance, i.e.:  $\eta = \eta(r)$ . The change  $\delta\rho_2(r) = \rho_2(r) - \rho(r)$  depends to lowest order only on the mean square relative strain

$\langle \eta^2(r) \rangle = \langle (\vec{u}(\vec{r}) - \vec{u}(\vec{0}))^2 \rangle$  between the atoms at  $\vec{r}$  and at the origin. The requirement that during relaxation near neighbor atoms must redistribute in a correlated fashion can be effected by simply correlating the strains over some distance  $\xi$  by writing:

$$\langle \vec{u}(\vec{r})\vec{u}(\vec{0}) \rangle = e^{-\frac{r}{\xi}} \langle \vec{u}^2(\vec{0}) \rangle,$$

which in turn gives:

$$\langle \eta^2(r) \rangle = 2 \left( 1 - e^{-\frac{r}{\xi}} \right) \langle \vec{u}^2(\vec{0}) \rangle. \quad (3.7)$$

Equation 3.7 expresses the fact that while nearby atoms move very little with respect to each other, the freedom for relative displacement increases with  $r$ . As the absolute displacements become uncorrelated at large lengths, the relative displacements saturate to a value of twice the mean square displacement of the individual atoms. Unfortunately this form for  $\langle \eta^2(r) \rangle$  does not yield a simple analytic expression for  $\delta S_2(q)$ . However from an *experimentally* determined  $\rho(r)$  (see Figure 3.20) we can calculate  $\delta S_2(q)$  numerically for a given value of  $\xi$ . When these changes are fitted to measured data we find that  $\xi > 7 \text{ \AA}$ , which is in fact consistent with the length scale of fluctuations seen by small angle neutron scattering in metal-metalloid glasses (Lamparter and Steeb *et al.* [39]). Now  $\rho(r)$  converges rapidly to  $\rho_0$  with increasing  $r$ , the envelope of  $\rho(r)$  and its derivatives decaying roughly exponentially over a characteristic length of about  $2 \text{ \AA}$  (see Figure 3.20). Therefore the fitting procedure may be further simplified by expanding Equation 3.7 to low  $r$  and then eliminating  $\xi$  explicitly by referring all relative strains to those in the first-neighbor shell. Thus we write:

$$\langle \eta^2(r) \rangle \simeq \frac{r}{r_0} \langle \eta^2(r_0) \rangle,$$

with  $r_0$  being the radius of the first shell (taken as  $2.75 \text{ \AA}$ ). We define the fractional strain field as

$$\zeta^2(r) = \frac{\langle \eta^2(r) \rangle}{r_0^2}.$$

The result reads, with the definition  $\zeta_0 = \zeta(r_0)$ :

$$\Delta S_2(q) = \zeta_0^2 \frac{2\pi r_0}{3q} \int_{r=0}^{\infty} \frac{d}{dr} \left( r^2 \frac{d\rho_r}{dr} \right) \sin(qr) dr. \quad (3.8)$$

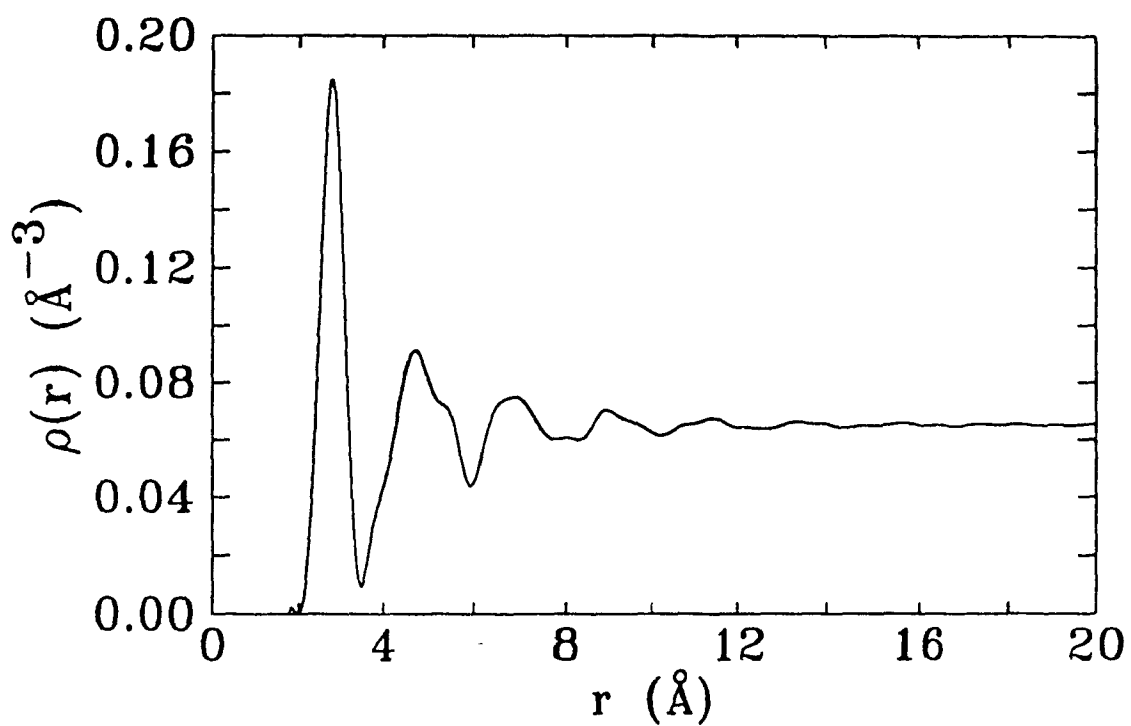


Figure 3.20: The radial distribution function of  $\text{Pd}_{10}\text{Ni}_{40}\text{P}_{20}$  in the reference state. The non-physical fluctuations of  $\rho(r)$  below  $2 \text{ \AA}$  that arise from the cutoff in  $q$  have been omitted from the plot for clarity.

With these approximations this result is mathematically identical to the expression proposed by Srolovitz *et al.* [86], although these authors did not provide any motivation for it, nor explain how it was related to physical processes.

### The Fitting Expression

With the above approximations we may now write the change in the structure factor as:

$$\Delta S(q) = S(q) - S_r(q) = \alpha_r(q) \frac{\Delta \rho_0}{\rho_0} + \beta_r(q) \zeta_0^2. \quad (3.9)$$

$S_r(q)$  is the structure factor of the sample in the reference state, and the quantities  $\alpha_r(q)$  and  $\beta_r(q)$  are completely determined from the reference structure by means of Equations 3.1 and 3.8. Specifically,

$$\alpha_r(q) = -\frac{q}{3} \frac{dS_r}{dq} \quad (3.10)$$

and:

$$\beta_r(q) = \frac{2\pi r_0}{3q} \int_{r=0}^{\infty} \frac{d}{dr} \left( r^2 \frac{d\rho_r}{dr} \right) \sin(qr) dr, \quad (3.11)$$

where  $\rho_r(r)$  is obtained from  $S_r(q)$  through the relation 2.2 (see e.g. [60]).  $\alpha_r(q)$  and  $\beta_r(q)$  are nearly orthogonal functions of  $q$ , as is shown in Figure 3.21; their normalized folding integral over the range in Figure 3.21 yields a value of 0.20. This feature, due to the fact that they describe essentially orthogonal processes (compression vs. local shear), ensures that each contribution is independently determined when the experimental data are fitted.

### 3.3.3 Results

Equation 3.9 is now used to fit the measured changes of structure factor. The fitted curves are shown in Figure 3.13.b (for irreversible processes) and in Figure 3.13.c (for reversible processes). Several things have been achieved for the first time by this new method:

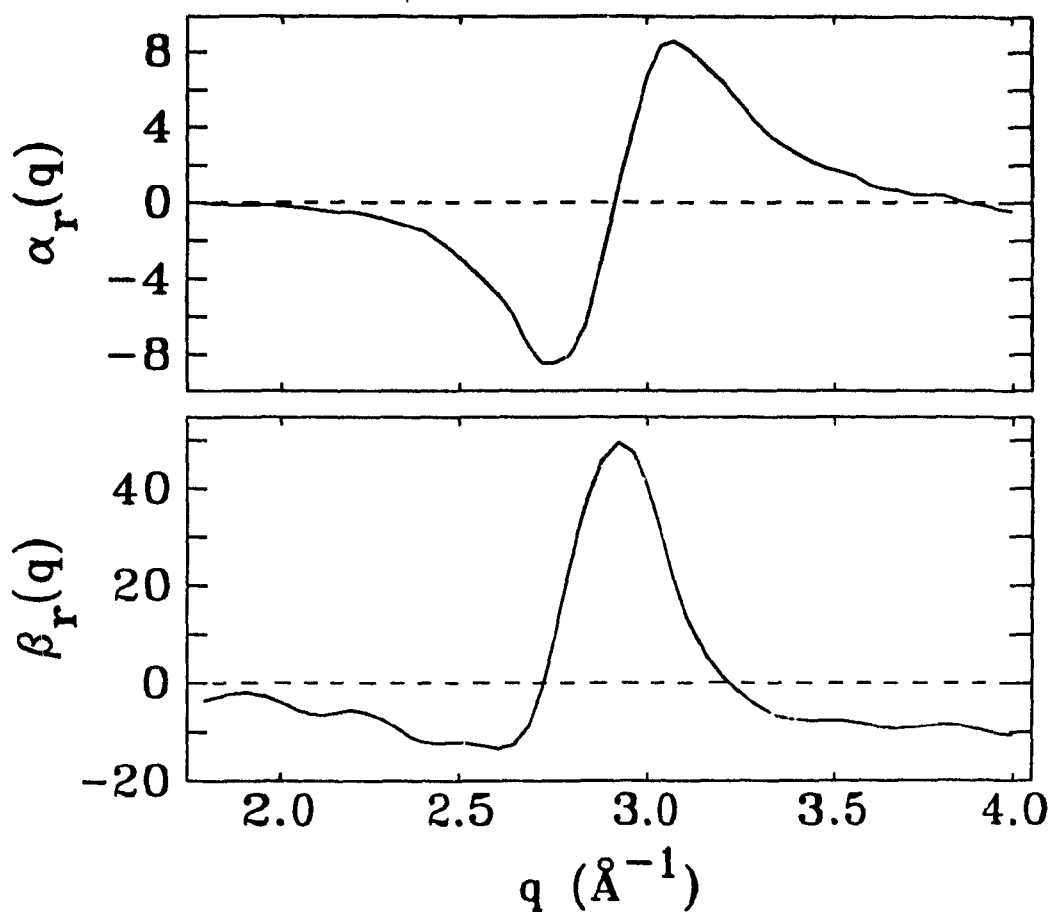


Figure 3.21: The fitting functions  $\alpha_r(q)$  and  $\beta_r(q)$  defined the Equations 3.10 and 3.11.

- the data are described very well, and better than by any previously published method;
- the fitting procedure is directly linked to a model which describes the atomic displacements;
- it distinguishes and resolves two different microscopic processes, which, as we shall see, relate to different kinds of macroscopic behavior;
- it is the first method which can extract changes in the x-ray density of amorphous metals in a reliable way;
- and it provides quantitative information about the length scale of atomic displacements.

The last points will become clearer as we turn to the analysis of the fitted parameters, the fractional change in density and the mean square relative strain. They are displayed in Table 3.2, which also shows enthalpy changes obtained by DSC and the density changes obtained by weighing (see Section 2.4.1). The sign after the value of  $\zeta_0^2$  describes whether the distribution function was sharper (−) or smoother (+) than the reference sample, as outlined above. The results in Table 3.2 are plotted in Figure 3.22. The changes of the parameters are shown with the reference state subtracted. The solid symbols indicate the parameters during irreversible relaxation, for which the temperature scale indicates the temperature to which the sample had been heated before the measurement. For consistency the as-made sample values are marked at 410 K, the temperature of the onset of the exotherm that marks irreversible relaxation (compare Figure 3.4.a), and the reference state is given by the rightmost points. The open symbols indicate the spectra obtained after annealing the reference state at the temperature  $T$  (reversible relaxation).

Several significant features emerge from these results. The density changes obtained from x-ray diffraction and weighing agree, although the slight differences in the values,  $(0.17 \pm 0.05)\%$  obtained from the direct measure of density (see Section 2.4.1) versus  $(0.23 \pm 0.05)\%$  deduced here from  $S(q)$ , might indicate some small

Table 3.2: Comparison of the X-ray Diffraction Results with Enthalpy and Density Measurements. Changes of the mean density  $\Delta\rho_0/\rho_0$ , measured by Archimedes method and x-ray diffraction, and the mean-square relative strain,  $\zeta_0^2$ . All differences are referred to a reference state obtained by heating the sample to 620 K at 40 K min<sup>-1</sup>, “+” in the column of  $\zeta_0^2$  refers to a broadening in  $\rho(r)$ , “-” to a sharpening.  $\Delta H$  was obtained by DSC measurements on simultaneously annealed reference samples.

Sample State	$\Delta H$ (J mol <sup>-1</sup> )	$10^{-2}\Delta\rho_0/\rho_0$ (Archimedes)	$10^{-2}\Delta\rho_0/\rho_0$ (X-ray)	$10^{-4}\zeta_0^2$
As-Made	470 ± 10	-0.17 ± 0.05	-0.23 ± 0.05	10.7 ± 0.3
Partial irreversible relaxation (Heated to 540 K)	120	-0.07	-0.06	6.1
Reference state (heated to 620 K)	0	0.00	0.00	0.0
Annealed 20 h at:				
440 K	-210	-	0.00	0.4
465 K	-160	-	-0.01	-0.2
483 K	-190	-	0.00	-0.1
490 K	-220	-	0.01	-1.7
500 K	-200	-	-0.06	-1.6
510 K	-260	-	-0.03	-2.5
523 K	-370	-	0.01	-4.1
540 K	-460	-	0.00	-8.4
573 K	-150	-	-0.01	-4.8

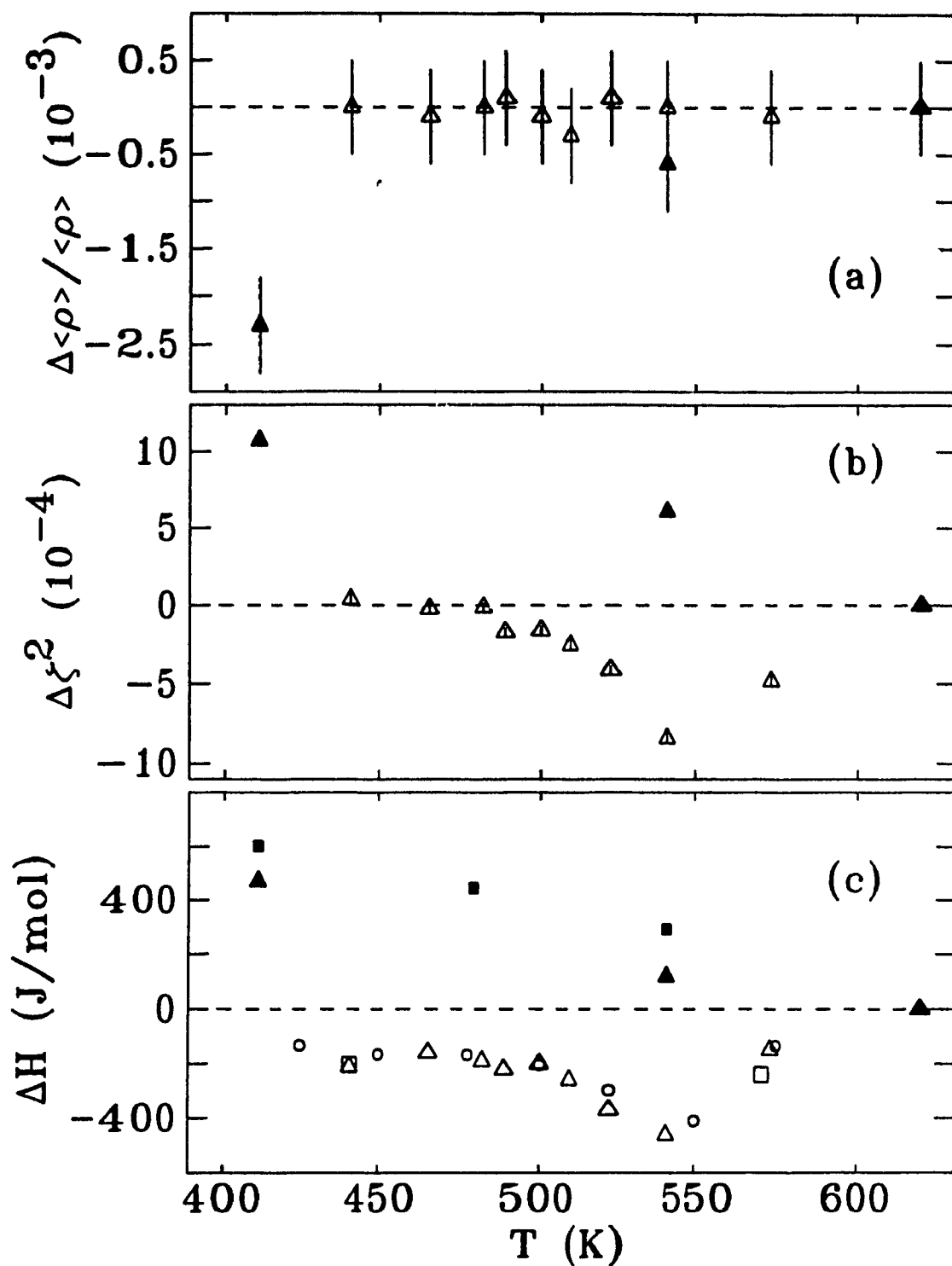


Figure 3.22: Changes in density and atomic ordering measured by x-ray diffraction: (a) density change, (b) change of atomic order, and (c) enthalpy changes. All changes are measured with respect to the reference state, which is marked by dashed lines. Solid symbols indicate irreversible relaxation and open symbols indicate reversible relaxation.

anisotropic length changes of the sample as reported by Cahn *et al.* [11]. Nonetheless, most of the signal arises from the isotropic densification during irreversible relaxation.

The x-ray density of a crystal is the density calculated from the lattice spacing of the atoms measured by x-ray diffraction. It gives in general a higher value than the real density because a crystal has some vacancies. For an amorphous material an x-ray density may not be obtained because the distribution of nearest neighbors is too wide, and the angular distribution of the atoms is not known. However, the method employed here allows for the first time to measure *changes* in the x-ray density of an amorphous material in a reliable way. (Chason *et al.* [34] obtained, by fitting to structure factors by the Percus-Yevick model, density changes which were in disagreement with the values obtained from x-ray absorption measurements).

Since we are able to extract the x-ray density changes, we may draw a second important conclusion from the density data: the density increase calculated by rescaling (diminishing) the interatomic distances indeed describes the microscopic process leading to the density change quite well, which implies that the voids that are eliminated during the density increase are much smaller than an atomic volume and are finely distributed in the glass. The alternative would be larger voids, like vacancies in a crystal, or even clusters of such vacancies. They may be ruled out because they would change the intensity of the scattered radiation, but not cause a shift of the diffraction pattern to larger angles.

However, a simple distance rescaling is not an adequate description of irreversible relaxation. Even if irreversible relaxation is regarded only as filling in of voids, such a process will inevitably involve some shifting in the relative arrangement of atoms; and indeed a process which could lower the energy by a simple length rescaling would occur spontaneously. Thus a change in density is only possible if it is accompanied by an additional structural change.

This additional structural change is a local shear-type motion which narrows the peaks in the radial distribution function. The fitted value for the asso-

ciated shear-motion corresponds to a root-mean-square-displacement of the atoms of 0.093 Å in the first atomic shell. This displacement is about a quarter of the width of the metal-metal nearest neighbor shell (0.39 Å for the Ni-Ni nearest neighbor shell in Ni<sub>80</sub>P<sub>20</sub>, see Lamparter and Steeb (1984), [82]). In Section 4.4.1 we will see that between room temperature and  $T_g$  the maximum displacement due to atomic vibrations is between 0.24 and 0.34 Å. This comparison shows that the change of peak width during structural relaxation processes is due to atomic displacements which are small compared to the width of the interatomic potential. This agrees with the fact that reversible changes of the structure factor occur; the magnitude of the reversible changes of  $\zeta_0^2$  are of same magnitude as the irreversible changes of  $\zeta_0^2$ . Since they are caused by annealing at different temperatures, which are typically only 100 K apart, they may only lead to small changes in the internal energy of the order of  $k_B\Delta T$ .

The decrease in the nearest neighbor distance calculated from the density increase during irreversible relaxation is 0.0026 Å. This value is very small compared to the displacement that gives rise to the narrowing of the radial distribution function and shows that a density change of the amorphous structure can only proceed along a long path in configuration space; i.e. the density cannot change without a considerable change of the overall structure of the glass. In particular, a decreased density can only be accomplished by rapid quenching of the melt.

For this reason no change of density occurs during reversible relaxation, only a sharpening or broadening of the radial distribution function. As is seen in table 3.2 it is easy to obtain an associated shear motion of the same order as in irreversible relaxation. However the density change in irreversible relaxation is linked to the low activation energy processes seen by DSC, where the irreversible endotherm starts just above room temperature (compare Figure 3.4.a). Its absence from reversible relaxation correlates nicely with the narrower range of activation energies there.

Our discussion does not address the question of whether reversible relaxation corresponds to changes in CSRO. Our analysis is written in terms of TSRO and would be equally valid for a single component glass such as amorphous silicon, so that the present results show that reversible changes can be understood solely in terms of TSRO, at least in  $\text{Pd}_{40}\text{Ni}_{40}\text{P}_{20}$ . This is a further indication beyond the DSC results that CSRO changes not of great importance to understand structural relaxation in metal-metalloid glasses.

However reversible relaxation is not a single type of phenomenon. Close to  $T_g$ , it involves substantial mean square relative displacements of the metal atoms, but these displacements fall off rapidly as the annealing temperature is lowered, and with it the atomic diffusivities. Indeed, as may be seen directly from Figure 3.22, no effects of reversible relaxation may be seen in the x-ray spectrum below about 500 K, even though quite substantial enthalpy changes are still visible. Whatever these changes are we conclude that they must be due to the displacement of the metalloid atoms alone, and to see those changes we must turn to a different technique. However before doing so, it is of interest to reexamine the data obtained by Waseda and Egami on  $\text{Pd}_{80}\text{Si}_{20}$  [32], and Chen, Aust and Waseda on  $\text{Cu}_{57}\text{Zr}_{43}$  [84] (see Figures 3.16 and 3.18) using the insight we have gained from our analysis of  $S(q)$ . For both studies the same experimental method was used, and the results on  $\text{Pd}_{80}\text{Si}_{20}$  agree well with the results of this thesis. But, although the authors write that the results on CuZr are "strikingly similar" to those on PdSi, closer inspection shows that the changes of the first peak of the structure factor are much broader in CuZr than in PdSi. In fact, the data on CuZr follow quite closely the expression  $\Delta S(q) \approx [S(q) - 1]$ , which was calculated for atomic rearrangements that are not impeded by any constraints (Figure 3.19), and corresponds to changes which affect the first nearest neighbor shell more strongly, which may also be seen from a comparison of the radial distribution function changes in [32] and [84]. At the end of Section 3.2.3 we commented that in metal-metal metallic glasses atomic long range order is less pronounced than in metalloid glasses. Making use of this additional piece of evidence it may be added

that it is also less susceptible to changes of long range TSRO during structural relaxation. This corroborates the assumption that changes in CSRO have been observed in purely metallic glasses.

### 3.4 Mössbauer Spectroscopy

As outlined in Chapter 1, Mössbauer spectroscopy is potentially important for studying structural relaxation because it provides information about changes in the local symmetry. One advantage of selecting  $\text{Pd}_{40}\text{Ni}_{40}\text{P}_{20}$  doped here with 0.5 at.%  $^{57}\text{Fe}$ , for the Mössbauer measurements of structural relaxation is the same as the one already mentioned in Section 3.3 for the x-ray diffraction experiment: the stability of the glass. An additional requirement is that the glass be paramagnetic, since changes in local symmetry directly affect only the quadrupole splitting. This is almost impossible to observe in a magnetic sample, where the quadrupole splitting averages to zero because of the random orientation of the electric field gradient with respect to the magnetic field and only results in a broadening of the lines. Moreover the line shifts (approximately 0.02 mm/s) which result from structural relaxation are significantly more difficult to detect on the wide velocity scale (approximately  $\pm 8$  mm/s) needed for collecting magnetic spectra, while the presence of another parameter with the broad distribution (the magnetic hyperfine field) would seriously reduce the significance of the fitting.  $\text{Pd}_{40}\text{Ni}_{40}\text{P}_{20}$  is paramagnetic, and at low concentration, the added iron causes no significant changes to the physical properties and, in particular, does not induce any transition to ferromagnetism, at least at room temperature. Naturally, what is going to be measured is the average environment of an iron atom in the amorphous  $\text{Pd}_{40}\text{Ni}_{40}\text{P}_{20}$  matrix. However, the information obtained for the iron atom should nonetheless be representative of the metal atom sites in the glass.

The Mössbauer spectrometer has been described in Sections 2.6.4 and 2.6.5. The data fitting procedures are described in Section 2.6.7.

### 3.4.1 The Data

Figure 3.23.a shows the Mössbauer spectrum for the sample in the reference state. The measured counts were converted to absorption by normalizing them with respect to the signal at high velocity. The spectrum is the broad, asymmetric, quadrupole-split doublet typical of a paramagnetic metallic glass. The effect of irreversible relaxation is shown in Figure 3.23.b. Spectra of the as-made sample and the partially relaxed sample are displayed with the reference-state spectrum subtracted to emphasize the changes. Figure 3.23.c shows the effects of reversible relaxation achieved by annealing the sample in the reference state for about 20 h at the temperatures indicated. Because the absorption varies by about 1.4 % from sample to sample, the spectra were normalized to the absorption of the reference spectrum before subtraction. To achieve a clearer presentation, the data points correspond to the average of three neighboring channels. The size of the error bars has been calculated based on Poisson statistics from the number of counts per data point.

To determine the parameters that underlie the spectra, the data must be fitted. As stated above the feature of most interest is the distribution of quadrupole splitting, and how it changes upon structural relaxation. This is shown in Figure 3.24 for three different annealing states obtained by fitting the quadrupole splitting distribution to a histogram (see Section 2.6.7). Irreversible relaxation sharpens the distribution, and the centroid shifts towards lower  $Q$ -values. This process continues during annealing at 545 K. While the distributions for the reference state and the sample subsequently annealed at 545 K are very well described by a Gaussian curve, the as-made quadrupole splitting distribution shows a small asymmetry, which is a non-Gaussian component in the distribution.

Putting this fine point aside for the moment, we proceed to fit the data with a Gaussian distribution of quadrupole splittings. The number of fitting parameters is reduced from sixteen (ten contributions to the histogram, the baseline,  $B$ , the absorption,  $A$ , the average center shift,  $\langle\delta\rangle$ , and the correlation between the center shift and the quadrupole field,  $a$ ) to six, which diminishes the uncertainty of the fitted pa-

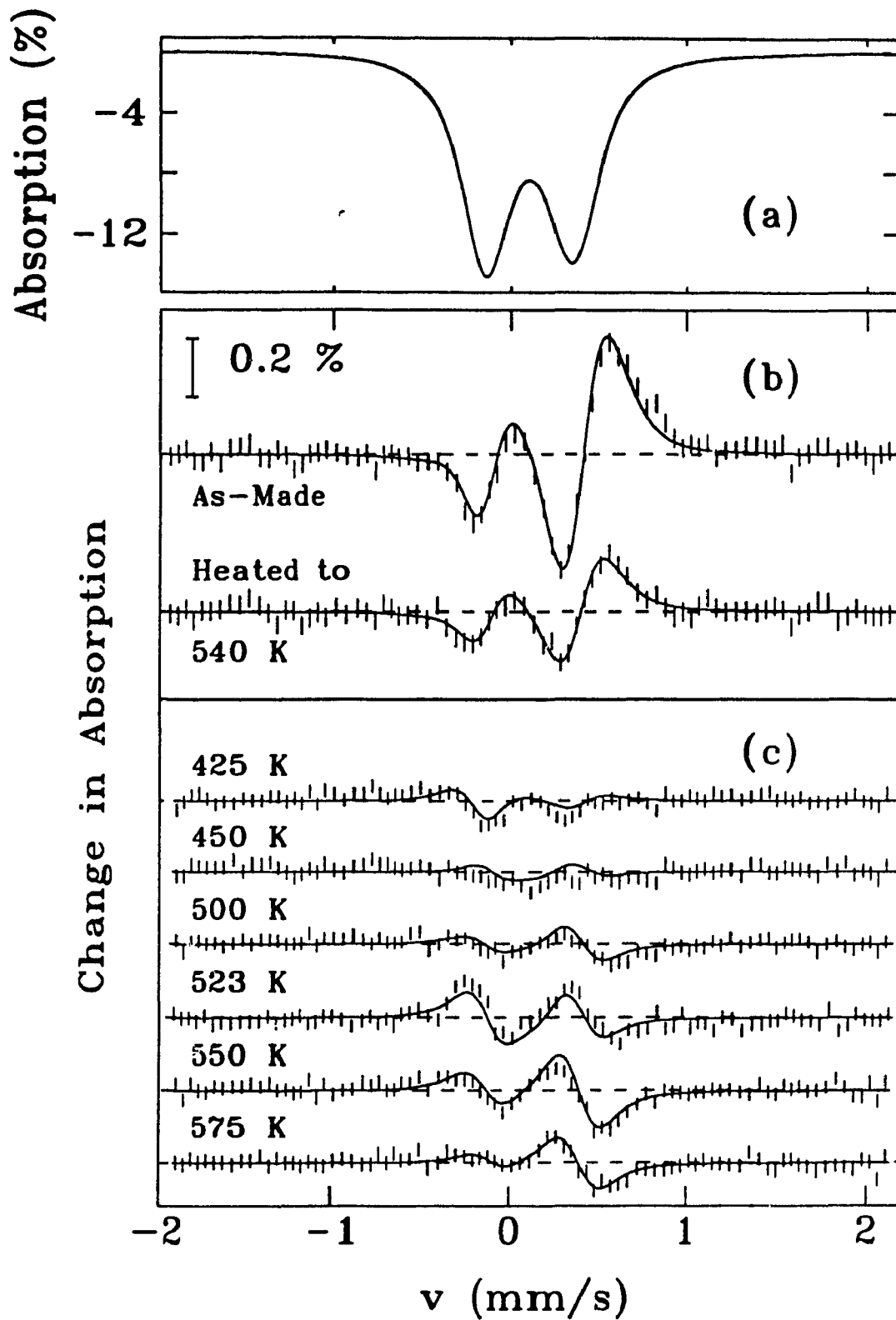


Figure 3.23: Changes of the Mössbauer spectrum caused by structural relaxation. (a) spectrum of the sample in the reference state, (b) irreversible relaxation: the difference between the spectrum of an as-made sample and the the reference state spectrum, and the difference between a partially relaxed sample and the reference spectrum; (c) the same for reversible relaxation, the samples were annealed for 20 h at the temperatures indicated. The solid lines show the differences between the fitted spectra.

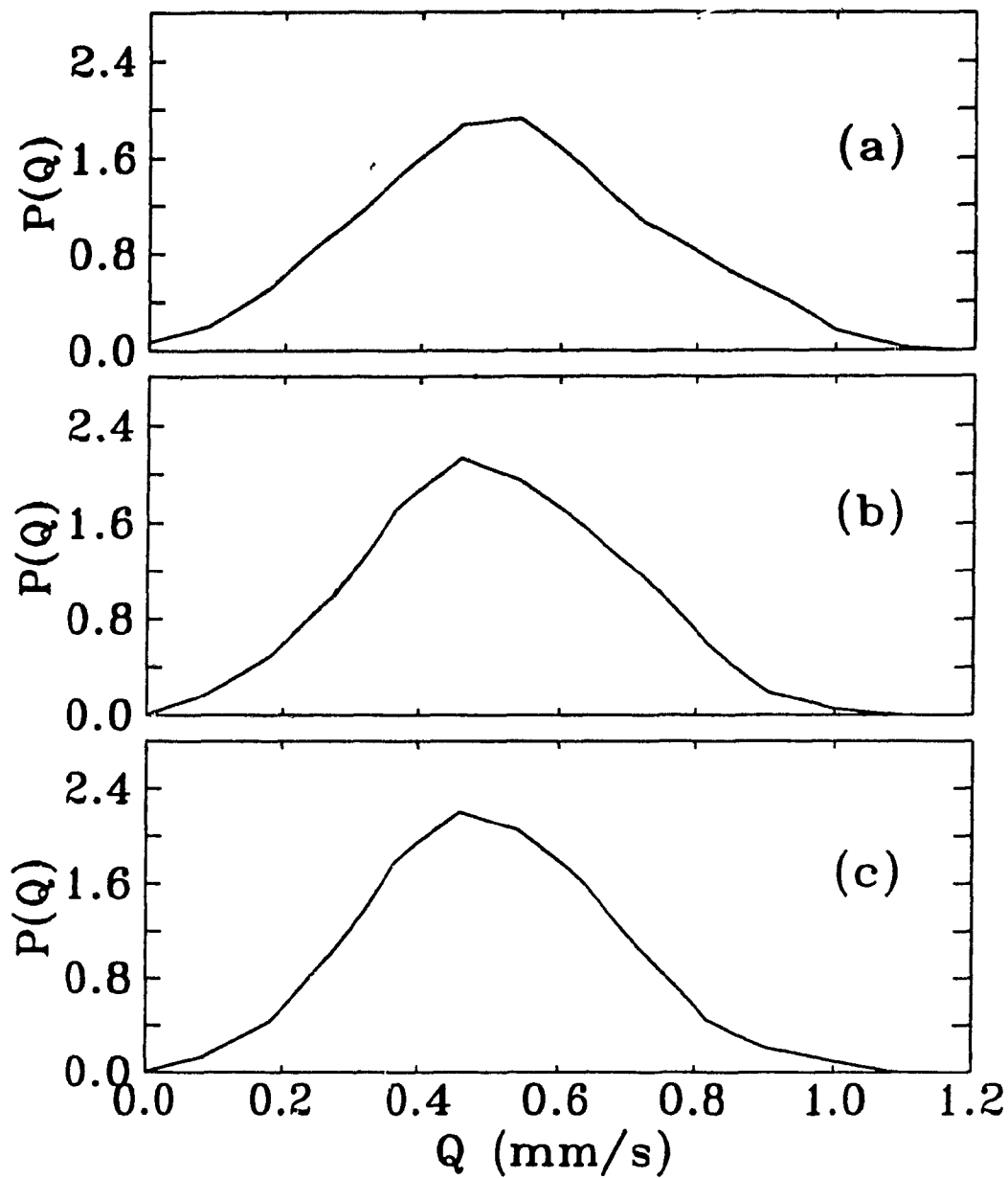


Figure 3.24: The quadrupole splitting distribution of for three different annealing states. The quadrupole distribution was fitted by a histogram: (a) for the as-made sample ; (b) for a sample in the reference state; (c) for a sample that was first brought to the reference state and then annealed for 24 h at 545 K (reversible relaxation). From (a) to (c) the distributions become narrower.

rameters significantly. The six parameters are the average quadrupole splitting ( $Q$ ), the width of the quadrupole distribution  $\sigma$ ,  $\delta$ ,  $a$ ,  $B$  and  $A$ . Figure 3.23.b and 3.23.c show the differences between the fitted curves, subtracted in the same way as data. Since the differences in the fit follow the differences in the data, the variations in the fitted parameters characterize the changes of the samples reliably. Figures 3.25 and 3.26 show  $\langle Q \rangle$ ,  $\sigma$ ,  $\delta$  and  $a$  for the various annealing states. The solid symbols indicate the parameters during irreversible relaxation, for which the temperature scale indicates the temperature to which the sample had been heated before the measurement. For consistency the as-made sample values are marked at 410 K, the temperature of the onset of the exotherm that marks irreversible relaxation (compare Figure 3.4.a), and the reference state is given by the rightmost points. The open symbols indicate the spectra obtained after annealing the reference state at the temperature  $T$ . Again, the observed changes can be reversed by resetting the sample to the reference state. The error bars represent the uncertainty in the fitted parameters. They were calculated from the dependence of  $\chi^2$ , the deviation of the fit from the data, on the fitting parameters. They depend on the statistical variations in the data points and are roughly of the same order as the scatter of the data. The additional scattering of the data is caused by small inconsistencies in mounting the samples.

### 3.4.2 Discussion

During irreversible relaxation  $\langle Q \rangle$ ,  $\sigma$ ,  $\delta$  and  $a$  decrease continuously as the sample reaches a more ordered state. This process continues until the sample has reached the reference state. Subsequent annealing causes changes that depend on the annealing temperature.  $\sigma$ ,  $\delta$  and  $a$  continue to decrease further at all temperatures.  $\langle Q \rangle$  also decreases upon annealing above 475 K, but increases if annealed below that temperature. This suggests that although low temperature annealing generates a more ordered state, the local symmetry actually decreases. We can interpret this surprising result further by using a model due to Czjzek *et al.* for the distribution

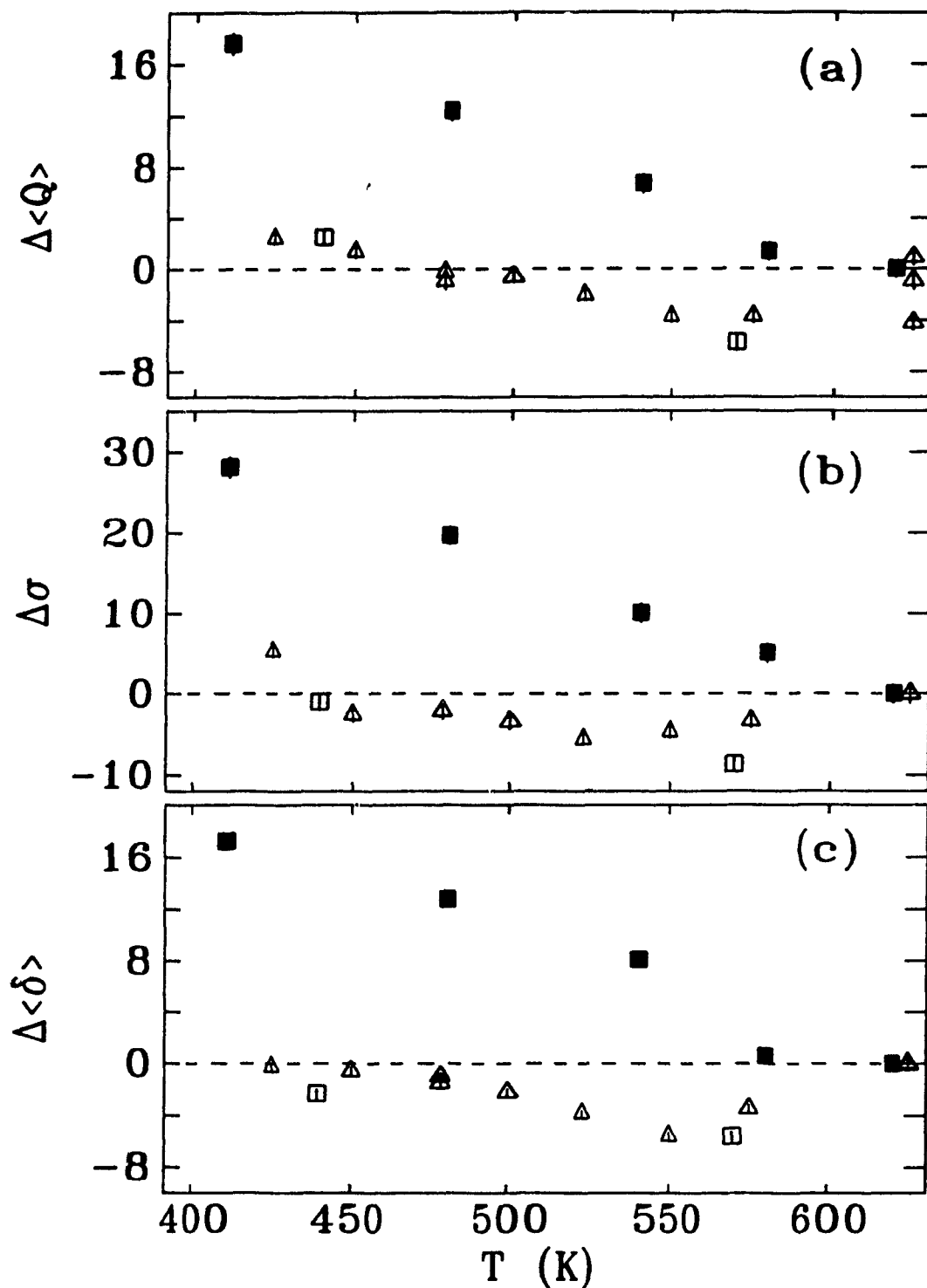


Figure 3.25: Change of the Mössbauer fitting parameters  $\langle Q \rangle$ ,  $\sigma$  and  $\langle \delta \rangle$  measured with respect to the reference state (dashed line). The units on the vertical scales are  $10^{-3}$  mm/s. The fitted values for the reference spectrum are  $\langle Q \rangle = 0.502$  mm/s,  $\sigma = 0.170$  mm/s, and  $\langle \delta \rangle = 0.100$  mm/s. Solid symbols indicate irreversible changes and open symbols indicate reversible changes. The data points marked by squares and triangles are from two separate series of measurements.

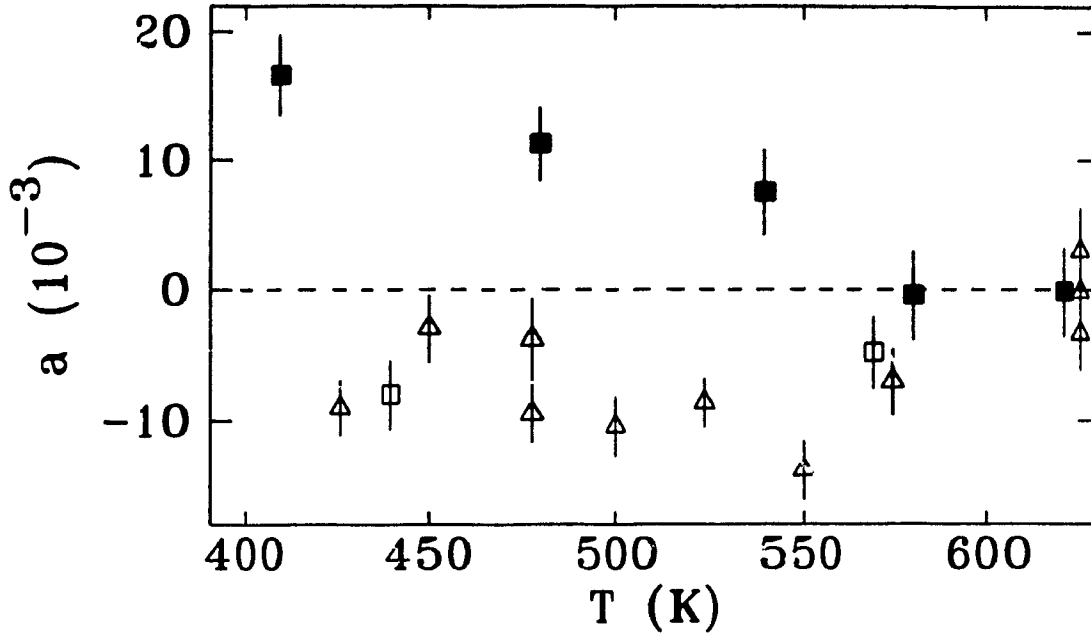


Figure 3.26: Change of the Mössbauer fitting  $\alpha$ , which describes the correlation between the distribution of  $Q$  and  $\delta$ .

of electric field gradients in an amorphous solid [44].

The model begins by writing the components  $V_{ik}$  (see Section 2.6.3) as linear combinations of five functions  $U_m$ , each of which is a linear combination of the spherical harmonics  $Y_m^l$ . (The explicit form for the  $U_m$  is given in [44] and is not needed here for the argument.) The quantities  $U_m$  are independent variables whereas the tensor components  $V_{ik}$  are constrained by the conditions of symmetry and vanishing trace. Since only the absolute value of  $Q$  can be observed, it is of interest to consider the behavior of  $Q^2$ :

$$(2Q/eq)^2 = V_{zz}^2(1 + \eta^2/3) = \frac{2}{3}(V_{xx}^2 + V_{yy}^2 + V_{zz}^2) = \frac{2}{3} \sum_{i,k} V_{ik}^2 = \sum_{m=0}^4 U_m^2 \quad (3.12)$$

where we have made use of the fact that  $V_{xx} + V_{yy} + V_{zz} = 0$ , that the sum of the diagonal elements squared of a symmetric matrix is constant under rotation and that the  $V_{ik}$  are linear combinations of the functions  $U_m$ . Equation 3.12 shows that  $Q$  has the character of a radial variable in the five-dimensional space spanned by the quantities  $U_m$ . The random arrangement of the atoms may then be approximated by assuming a Gaussian distribution of the variables  $U_m$  around zero ( $Q = 0$  represents

a spherically symmetric distribution). Then the volume element corresponding to a particular value of  $Q$  is proportional to the surface area of a five dimensional sphere, i.e.  $Q^4$ . On the other hand the width of the distribution is proportional to the radius of the sphere, given by the spread of the values of  $Q$ . The distribution of  $Q$  should therefore be given by:

$$P(Q) \propto \frac{Q^4}{\sigma_P^5} \exp\left(\frac{-Q^2}{2\sigma_P^2}\right). \quad (3.13)$$

Naturally,  $\sigma_P$  in Equation 3.13 is different from  $\sigma = \langle Q^2 - \langle Q \rangle^2 \rangle$ . The main conclusions from this result are:

- $\sigma_P$  is the only free parameter, and  $\langle Q \rangle$  can be calculated once it is determined.
- The ratio  $R$  between the width of the quadrupole distribution and its mean value is  $R = \sigma / \langle Q \rangle = 0.323$ .
- The shape of the distribution 3.13 is, to a very good approximation, a Gaussian distribution centered at  $\langle Q \rangle$ .
- $P(Q) = 0$  at  $Q = 0$ .

The value of  $R$  agrees well with the value obtained for the reference state, 0.325. Furthermore,  $P(0)$  is actually zero once irreversible relaxation is completed (Figure 3.24). The fixed ratio between  $\sigma$  and  $\langle Q \rangle$  predicted by Equation 3.13 agrees with the observation that in general the values of  $\langle Q \rangle$  and  $\sigma$  are correlated (Figure 3.25).

That there are contributions to  $P(Q)$  at  $Q = 0$  in the spectrum from the as-made sample, and that the value of  $R$  obtained is 0.368 rather than the value predicted by Czjzek's model, 0.323, may be understood by examining the effect of a distribution of isomer shifts in addition to the distribution of  $Q$  (Lines and Eibschütz, 1983 [88]). The influence of such an additional term can be appreciable in certain situations. By calculating how such an additional broadening would appear if it were attributed to quadrupole splitting distribution, Lines and Eibschütz found an effective distribution which is very similar to the one obtained here for the as-made

sample. Now an appreciable distribution of isomer shifts in the as-made sample is expected because of the free volume. We have seen that, once irreversible relaxation is complete, further annealing cannot alter the density of the sample, in agreement with the suggestion that the distribution of center shifts is only of importance for the as-quenched sample. If that is indeed the case <sup>5</sup>, then the increased value of  $R$  is a result of absorbing the additional distribution of the isomer shift into  $\sigma$ . Furthermore, since  $P(Q = 0) = 0$  in the relaxed samples, the width of the distribution of isomer shifts is negligible for them.

From the above we conclude that the reference state is very well described by a randomly packed structure as suggested by Czjzek *et al.*. We can now interpret small deviations from the distribution 3.13 during reversible relaxation. The changes of the parameters  $\langle Q \rangle$  and  $\sigma$  depend on the annealing temperature in different ways. While  $\sigma$  diminishes at all temperatures,  $\langle Q \rangle$  only decreases upon annealing above 475 K, while it increases when annealed below that temperature (Figure 3.25). The simultaneous decrease of both values corresponds to a increase in the atomic order, as one should expect. But if  $\langle Q \rangle$  increases while the  $\sigma$  decreases, as it is the case for low annealing temperatures, then a net decrease in the site symmetry has to be the cause, the local environments becoming on average more asymmetric. This result is *important* as it establishes a clear difference between the microscopic relaxation processes at high and low temperatures. It is well known that all physical

---

<sup>5</sup>A generalization of Equation 3.13, derived from the assumption that there are additional physical constraints in the charge distribution which reduce the number of free elements in  $V_{ij}$ , allows lower powers than four in the prefactor of  $P(Q)$  [83]. Then a power of three for example, which corresponds to one degree of freedom less, would give a value of  $R$  of 0.363. But still the deviation from  $P(Q) = 0$  remains, apart from the fact that an additional constraint can hardly be expected in an even more disordered state. A possible way to obtain  $P(0) \neq 0$  would be a structure that favors symmetric configurations [44]. Although with increasing temperature the local symmetry should increase, if one disregards the equally increasing randomness, a pole of the order of four at  $U_m = 0$  needed to give a contribution to  $P$  is improbable. So both these possibilities are rather unlikely, which leaves us with a distribution of isomer shifts as the only possible explanation.

systems tend to show symmetry breaking at low temperatures. In a crystalline system this would appear suddenly as a phase transition, while the glass evolves more continuously with temperature.

We turn now to the discussion of the changes of the center shift itself. All spectra were measured at room temperature, so that the second order Doppler shift is the same for all measurements. Thus all observed changes can be attributed to changes in the electron density at the nucleus. One obvious question is whether the change of the center shift by  $-0.017$  mm/s during irreversible relaxation can be attributed to the observed density increase of 0.2%, which gives for the logarithmic volume dependence:

$$\frac{\partial \langle \delta_{ISO} \rangle}{\partial \ln V} = 8.5 \frac{\text{mm}}{\text{s}}.$$

Williamson reports measurements of the dependence of  $\delta_{ISO}$  for  $^{57}\text{Fe}$  in crystalline metals on volume changes induced by high pressures [90], which gave the range:

$$0.5 \frac{\text{mm}}{\text{s}} \leq \frac{\partial \langle \delta_{ISO} \rangle}{\partial \ln V} \leq 1.8 \frac{\text{mm}}{\text{s}}.$$

A second estimate can be obtained from the temperature dependence of  $\langle \delta_{ISO} \rangle$  in  $\text{Pd}_{40}\text{Ni}_{40}\text{P}_{20}$ , (see in Section 4.4.2), which gives:

$$\frac{\partial \langle \delta_{ISO} \rangle}{\partial \ln V} = 2.8 \frac{\text{mm}}{\text{s}}.$$

These estimates for the volume dependence of  $\langle \delta_{ISO} \rangle$  obtained from varying the pressure and varying the volume agree quite well, but the value obtained from irreversible structural relaxation is substantially larger. In addition,  $\delta$  changes substantially, by about 0.006 mm/s, during reversible relaxation, upon which, as shown above in Section 3.3.3, the density does not change at all.

For these reasons it is clear that most changes in the isomer shift during irreversible structural relaxation, and all changes during reversible structural relaxation, must have a physical origin different from density changes. A comparison with the x-ray data shows that the decrease of the isomer shift agrees very well with the increased order of the metal atoms, measured by the parameter  $\zeta_0^2$ , although we

cannot quantify how this redistribution of the metal atoms influences the electron density.

The changes in the correlation coefficient  $a = \frac{\delta - \langle \delta \rangle}{Q - \langle Q \rangle}$  are measurable but small (see Figure 3.26). Since the origin of the correlation is not well understood [91] and so many parameters are involved, including changes of  $\langle \delta \rangle$  and  $\langle Q \rangle$ , it is impossible at this point to extract any information from it.

### 3.5 Summary

In this section the results of x-ray diffraction, Mössbauer spectroscopy and DSC are brought together in order to provide a complete picture.

Irreversible relaxation depends mainly on the quench conditions and the thermal history of the glass, much less on the composition of the glass. It is accompanied by a density increase of about 0.2% for the  $\text{Pd}_{40}\text{Ni}_{40}\text{P}_{20}$  glass studied here by x-ray diffraction. This glass reduces its enthalpy by about 500 J/mol while being heated to  $T_g$  for the first time. The disorder in the glass decreases as one would expect, as can be seen from the decrease of  $\sigma$ , the width of the quadrupole splitting distribution, and the decrease of  $\zeta_0^2$ , which corresponds to a sharpening in the metal-metal radial distribution functions. From the shape of the quadrupole field distribution an appreciable spread of isomer shifts has been inferred for the as-made state, which essentially vanishes after irreversible relaxation. This has been attributed to the large free volume present in the as-made state, which appears as fluctuations in the local structure. The observed value of  $\langle Q \rangle$  decreases. This is caused by the decrease in disorder, and is related to the decrease in  $\sigma$ .

Figure 3.27 and Figure 3.28 show the changes of the measured parameters rescaled with the enthalpy. All parameter changes are measured with respect to the reference state.  $\Delta Q/\Delta H$ ,  $\Delta\sigma/\Delta H$ ,  $\Delta\langle\delta\rangle/\Delta H$  and  $\Delta\rho/(\rho\Delta H)$  are independent of the temperature to which the as-made sample is scanned, which implies that the atomic processes involved are independent of activation energy. On the other hand

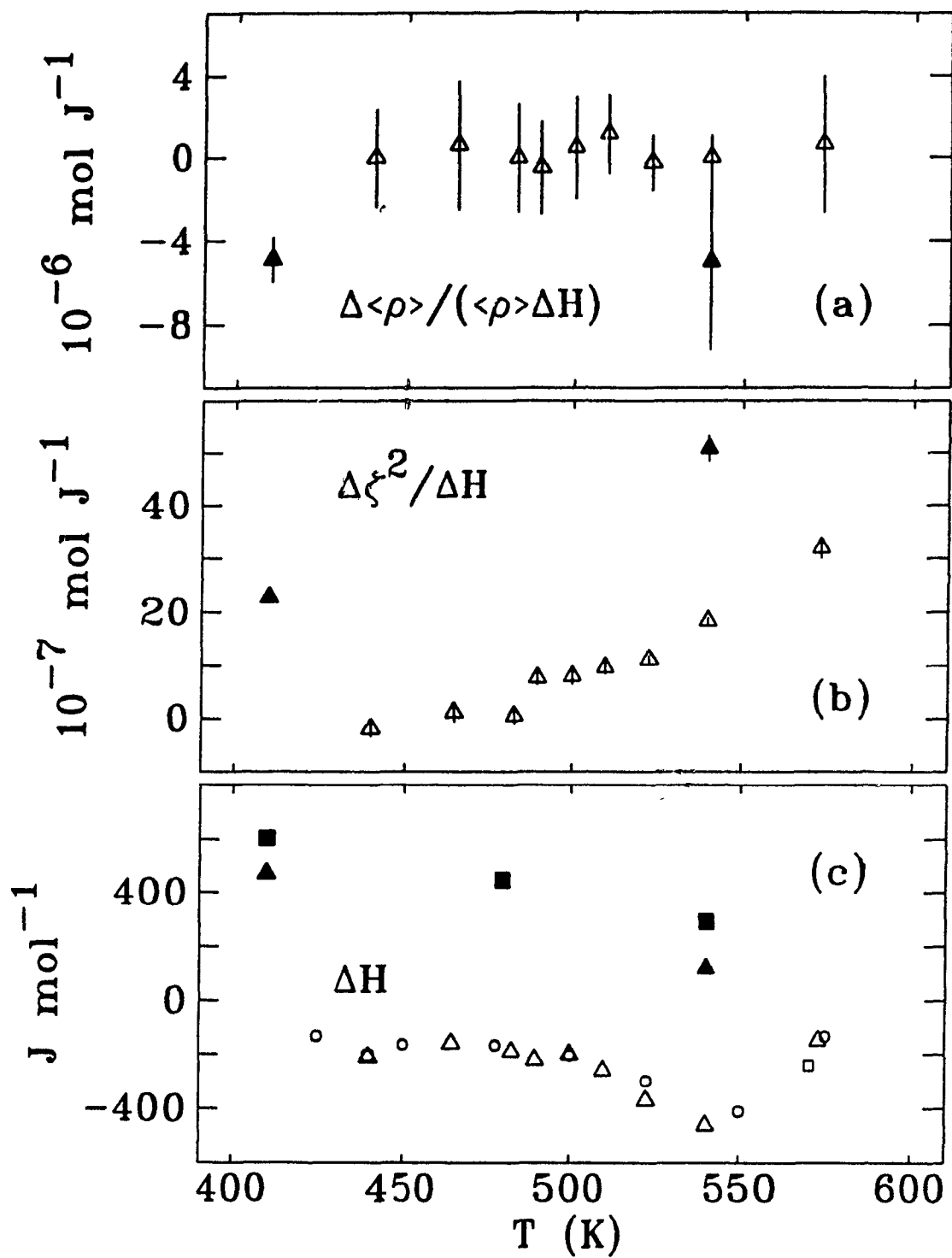


Figure 3.27: Changes of density (a) and atomic order (b) divided by the enthalpy changes. As a reference the enthalpy changes themselves are given once more in (c). Irreversible relaxation is marked by the solid symbols and reversible relaxation by the open symbols. Because the enthalpy changes upon reversible relaxation are negative, the sign of the scaled quantities is opposite to the sign of the unscaled quantities.

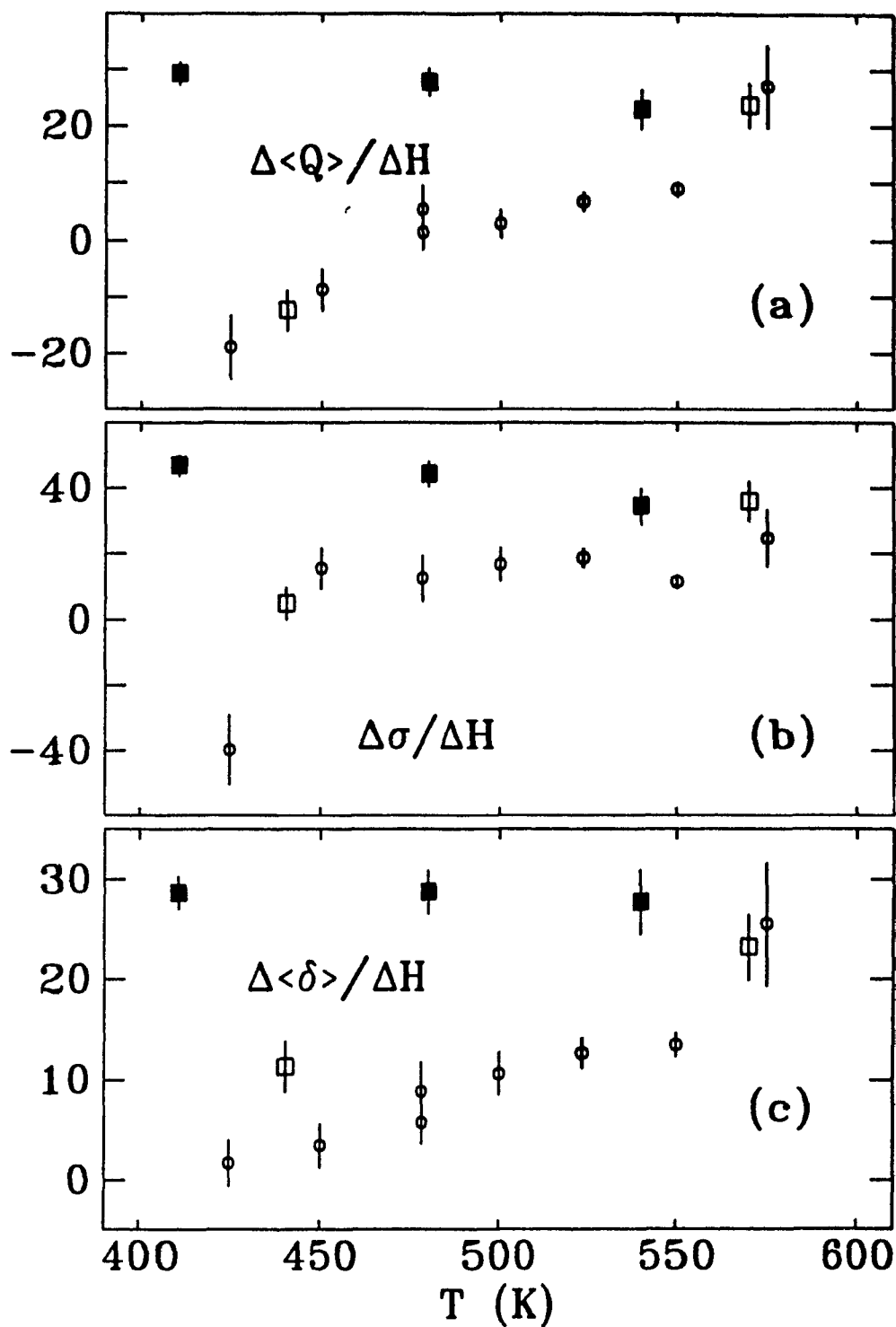


Figure 3.28: Changes of Mössbauer fitting parameters scaled to the enthalpy changes. (a) average quadrupole splitting; (b) width of the quadrupole splitting distribution; and (c) average isomer shift. The units on the vertical scales are  $10^{-6} \text{ mms}^{-1} \text{ mol J}^{-1}$ . Irreversible relaxation is marked by the solid symbols and reversible relaxation by the open symbols. Because the enthalpy changes upon reversible relaxation are negative, the sign of the scaled quantities is opposite to the sign of the unscaled quantities.

$\zeta_0^2/\Delta H$ , which corresponds to the rearrangement of the metal atoms, is smaller for lower annealing temperature, and hence lower activation energies. This correlates with the observation that reversible relaxation processes that involves the metal atoms (*i.e.* the processes detectable by x-ray diffraction) are also found to have high activation energies.

Now we turn to the results on reversible relaxation. These results are marked by the open symbols in the Figures 3.27 and 3.28. The Figures 3.27.b, 3.28.a, 3.28.b and 3.28.c show that  $\Delta\zeta^2/\Delta H$ ,  $\Delta Q/\Delta H$  and  $\Delta\sigma/\Delta H$ , the parameter changes per unit enthalpy change, converge at the right hand side of the temperature scale; it follows that reversible structural relaxation processes at high annealing temperatures - which are driven by cycling the glass through  $T_g$  - are of the same type as the irreversible structural relaxation processes. This is not surprising, since in both cases the glass is heated and cooled through  $T_g$ , although the cooling rates are very different.

So far we have observed a continuous evolution of the local atomic processes from irreversible relaxation to reversible relaxation. However there is one important exception in so far as the density remains constant during reversible relaxation. (Figure 3.27.a). Apparently a glassy state with a lower than optimal room temperature density may only be obtained by a very rapid quench.

The enthalpy changes during reversible relaxation are of the same order as the enthalpy changes due to irreversible relaxation (Figure 3.27.c), although the glass has already minimized its free volume. This means that substantial rearrangements at constant volume are possible in a glass, which we will examine in the following.

With decreasing annealing temperature the reversible processes change. The very substantial difference in activation energy was already mentioned above (see Table 3.1). While annealing at low temperature gives kinetic parameters which are indicative of localized processes that are well described by Arrhenian behavior, at high annealing temperature one obtains kinetic parameters that may only be understood by assuming a phase-transition-like behavior. Here, for the first time,

the temperature dependence of the corresponding microscopic processes has become accessible. Figures 3.27.b, 3.28.a and 3.28.c show a linear dependence of the normalized parameters – and therefore the type of the atomic processes – on the annealing temperature.<sup>6</sup>

Processes with high activation energy occur during annealing at 470 K and higher. At these temperatures the glass is more susceptible to thermal changes because of favorable kinetics and a large number of accessible structural degrees of freedom, and the glass may even reach internal thermal equilibrium. The most prominent part of the microscopic changes in this regime is a rearrangement of the metal atoms. This rearrangement narrows the radial distribution of the metal-metal atoms. The extent to which this occurs increases over the temperature range as shown by the dependence of  $\Delta\zeta_0^2/\Delta H$  (Figure 3.27 b). Changes of the isomer shift are highly correlated with these changes (Figure 3.28.c), but it is not clear at this point how and why these two quantities are related. The other parameter indicative of atomic order,  $\sigma$ , shows a trend to a smaller *random* distortions in the environment of the iron atoms. This effect decreases with temperature as well, but is detectable for all annealing temperatures (Figure 3.25.b). Rescaling with the corresponding enthalpy changes shows that the temperature dependence is only small (Figure 3.28.b). As shown in Section 3.4.2, the decrease of  $\langle Q \rangle$  (Figure 3.25.a) is linked to the decrease of  $\sigma$  and thus the decrease of random disorder.

Reversible relaxation processes caused by annealing at low temperature have of course lower activation energy and can be reset far below  $T_g$ . No changes in the average relative position of the metal atoms could be detected. As a consequence, the substantial enthalpy changes must be caused by a rearrangement of the metalloid atoms which leaves the distribution of metal atoms unaltered. This is supported by the known the diffusion coefficients, which show that at low temperatures the

---

<sup>6</sup>Note that it is necessary to scale the parameter changes with the enthalpy to obtain the linear temperature dependence. In Figures 3.22 b, 3.25 a and 3.25 c an additional temperature dependence appears which is entirely due to more or less favorable kinetics, which had to be eliminated here to see temperature dependence of the microscopic changes

phosphorus atoms diffuse fastest, as may be seen from Figure 3.8.

Although the scattering cross section of phosphorus for x-rays is too low to observe changes, the redistribution of the phosphorus atoms still affects the Mössbauer signal, particularly through the electric-field gradient, since the metal and phosphorus atoms are nearest neighbors. The Mössbauer spectroscopy results indicate a *net distortion* of the environment of the iron atoms away from spherical symmetry has been detected. This has already been discussed in Section 3.4.2. Here, after rescaling the the change of  $\langle Q \rangle$  with  $\Delta H$ , this may be seen even more clearly. Figure 3.28.b shows that  $\Delta\langle Q \rangle$  changes sign, while  $\sigma$  remains nearly constant (Figure 3.28.c).

We conclude that reversible changes due to annealing close to  $T_g$  mainly reduce random fluctuations in the structure and may in most aspects be regarded as a continuation of irreversible relaxation. As the annealing temperature is lowered, the nature of the reversible processes changes continuously, and eventually leads to an increases of the local site asymmetry. This behavior is reminiscent of phase transitions which reduce the symmetry in crystalline systems. However, in the glass we find a gradual variation of the metastable equilibrium state that the glass tries to reach rather than a sudden transition.

## Chapter 4

# Mössbauer Spectroscopy

## Measurement of the Glass

## Transition

### 4.1 Introduction

The preceding chapter discussed the microscopic structure of metallic glasses at room temperature and how it depends on the thermal history. This chapter is about the microscopic dynamics and how they change from room temperature to above  $T_g$ . The glass transition is characterized by a rapid drop in viscosity, an increase in the temperature coefficient of volume expansion and the onset of long-range atomic diffusion on laboratory time scales. Mössbauer spectroscopy is sensitive to atomic motion since it causes the nucleus to experience an additional time dependent phase shift in the radiation field of the  $\gamma$ -rays. Although only the motion of the iron atoms is detected, we may nonetheless obtain information about the glass as a whole since the motion of the iron atoms reflects the motion of the other atoms in the glass. Furthermore, the iron atoms are, in size and mass, comparable to the nickel atoms.

The motion of an atom in a solid or a liquid may be separated into two com-

ponents: fast vibrational motion, which has a frequency of typically  $10^{13}$  Hz, and slower diffusional motion. The vibrational motion gives rise to the temperature dependence of the recoil-free fraction  $f$ . During the lifetime of the excited state, about  $10^6$  vibrations occur. Because of the effectively random oscillation between emitter and absorber, there is a random phase-shift in the radiation seen by the absorber which leads to a reduction in  $f$  by a factor  $\exp(-k^2\langle x^2 \rangle)$ , where  $k$  is the wave number of the  $\gamma$ -ray (see Section 2.6.1). The full calculation can be found in the original paper by Lamb, (1938) [92].

The slow diffusive motion is distinguished from the vibrational motion in so far as it changes the equilibrium position of the atom and thus introduces a phase shift that does not average to zero over time. The wavelength of the 14.4 keV  $\gamma$ -ray, which gives the length scale against which atomic motion is measured, is 0.863 Å. If  $\tau$  is the time necessary for an atom to move over a significant fraction of this distance, the absorption line is shifted randomly which leads to a broadening of the order of  $\hbar/\tau$ , since the energy broadening is related to the lifetime of the state by the Heisenberg uncertainty relation. A more careful calculation shows that the maximum broadening of the line is in fact [93,94]:

$$\Delta\Gamma = \frac{2\hbar}{\tau}. \quad (4.1)$$

Thus Mössbauer spectroscopy is sensitive to diffusion if it increases the line by a measurable fraction, which requires that the atom diffuses on about the same time scale as the lifetime of the excited state.

If we assume that diffusion occurs by sudden jumps, the diffusion constant relates the hopping time  $\tau$  to the hopping distance  $r$  by the Einstein-Smoluchowski equation:

$$D = \frac{\langle r^2 \rangle}{6\tau},$$

so that:

$$\Delta\Gamma = \frac{12\hbar D}{\langle r^2 \rangle}. \quad (4.2)$$

If, on the other hand, the diffusional motion is continuous (i.e. many small steps

occur which are much shorter than  $0.863 \text{ \AA}$ ), then we have to consider the time that an atom needs to move over the distance of a wavelength:

$$\tau \approx \frac{1}{k^2 D},$$

giving:

$$\Delta\Gamma = 2\hbar k^2 D. \quad (4.3)$$

Jump diffusion and continuous motion are the two limiting cases of atomic diffusion. In liquids close to the melting point generally jump diffusion is the more important process [95]. In combination with an independent diffusion measurement, Mössbauer spectroscopy offers, at least in principle, a way to determine both the jump frequency and the jump distance, although it must be remembered that diffusivity measured macroscopically and by the Mössbauer effect may differ slightly since the latter includes jumps which take the atom back to its original position. Here these differences are too small to be of importance for the interpretation of the data.

Thus Mössbauer spectroscopy can detect the two components of atomic motion, vibration and diffusion. The reliability of this method has been shown in several instances (see the review article by Vogl [96]), and in particular for pure crystalline iron at high temperatures [97,98].

Quite soon after the discovery of the Mössbauer effect, Mössbauer spectroscopy was used to study liquids, glasses and the glass transition in non-metallic materials. Some of these studies and their principle results are listed in the Tables 4.1 and 4.2. Some representative data are reproduced in the Figures 4.1 and 4.2. In all these measurements the glass transition is quite distinct. Although the detailed observations are quite varied, some generalizations are possible. Above the glass transition the  $f$ -factor begins to decrease more rapidly with temperature (with the exception of the measurement on the polymer), which implies that the amplitude of motion increases more rapidly with temperature above  $T_g$ . All studies that give data on the center shift  $\delta$ , apart from the results on oxide glasses, indicated that

Table 4.1: Measurements of the glass transition by Mössbauer spectroscopy.

Year	Authors	System / Addition	Change at $T_g$
1963 [99]	Bernas and Langevin	$\text{FeCl}_3 \cdot 6\text{H}_2$	$f$ drops to zero
1963 [100]	Craig and Sutin	Glycerol / $^{57}\text{CoCl}_2$	$\Delta\Gamma$ sudden increase
1966 [95]	Elliott <i>et al.</i>	Glycerol / $^{57}\text{Fe}$	$\Delta\Gamma$ different types of diffusion processes
1970 [101]	Simopoulos <i>et al.</i>	Methanol / $\text{FeCl}_2$	$f$ decrease $\langle Q \rangle$ decrease
1971 [102]	Ruby and Pelah	HCl in water / $\text{SnCl}_4$	$f$ slope decreases $\Delta\Gamma$ sudden increase
1971 [103]	Brunot <i>et al.</i>	$\text{FeCl}_2$ in water	$f$ does not change (rotational transition) $\langle Q \rangle$ decrease $\Delta\Gamma$ continuous exponential increase $\delta$ no change
1972 [104]	Reich and Michaeli	Polymer / $\text{Fe}(\text{ClO}_4)_2$	$f$ slope increases
1972 [105]	Abras and Mullen	Glycerol-Water / $\text{FeCl}_2$	$f$ decrease $\langle Q \rangle$ decrease $\Delta\Gamma$ decrease of $E_a$ for diffusion $\delta$ no change
1976 [106]	Ruby <i>et al.</i>	Butyl Phthalate / Ferrocene	$f$ pronounced decrease of slope $\Delta\Gamma$ decrease of $E_a$ for diffusion

Table 4.2: Measurements of the glass transition by Mössbauer spectroscopy (cont.).

Year	Authors	System / Addition	Change at $T_g$
1976 [107]	Flinn <i>et al.</i>	H <sub>3</sub> PO <sub>4</sub> in water / <sup>57</sup> Fe	$f$ decrease of slope $\langle Q \rangle$ slope decreases $\Delta\Gamma$ continuous exponential increase $\delta$ no change
1977 [108]	Litterst <i>et al.</i>	Propanediol / Fe <sup>2+</sup>	$f$ decrease $\langle Q \rangle$ decrease $\Delta\Gamma$ continuous exponential increase $\delta$ no change
1980 [109]	LaPrice and Uhrich	Liquid Crystals / <sup>57</sup> Fe	$f$ decrease of slope $\langle Q \rangle$ decrease $\Delta\Gamma$ sudden increase $\delta$ no change
1983 [110]	Bharati <i>et al.</i>	Oxide Glasses / <sup>57</sup> Fe	$f$ small change of slope $\langle Q \rangle$ change of slope (positive or negative) $\Delta\Gamma$ continuous exponential increase $\delta$ change of slope (positive or negative)

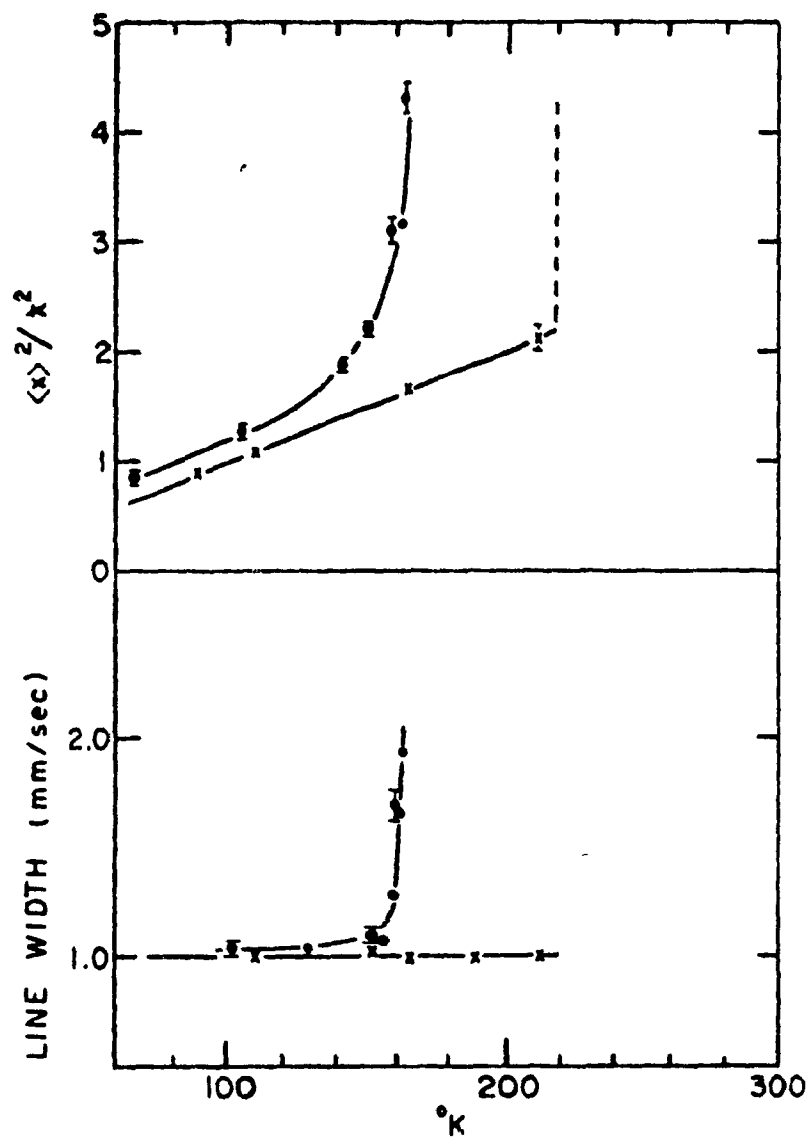


Figure 4.1: The vibrational amplitude and the linewidth obtained from Mössbauer spectroscopy in  $\text{HCl} \cdot 6\text{H}_2\text{O}$  with dissolved  $\text{SnCl}_4$  to perform the Mössbauer experiment. The linear lines give the results for the crystallized solutions [102].

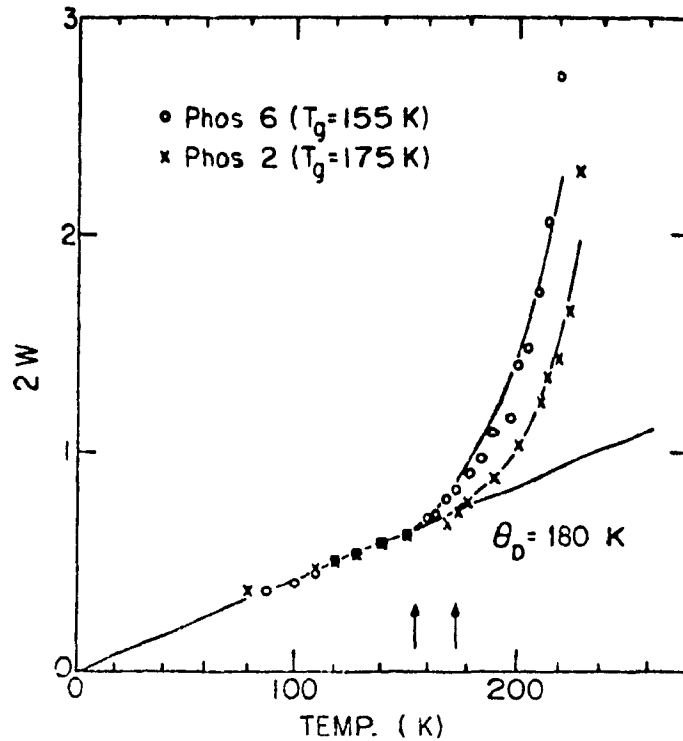


Figure 4.2: [The  $f$ -factor of supercooled  $\text{H}_3\text{PO}_4 \cdot \text{H}_2\text{O}$  (Phos 2) and  $\text{H}_3\text{PO}_4 \cdot 6\text{H}_2\text{O}$  (Phos 6). Note that  $2W = k^2\langle x^2 \rangle$ .

the center shift did not change at  $T_g$ . In all cases where it was reported, again with the exception of some oxide glasses, the quadrupole splitting  $\langle Q \rangle$  decreases. The linewidth increased in all cases at  $T_g$  as the atomic diffusion increased. However, the details of this increase vary substantially between the systems. In some cases it starts well below  $T_g$ , in others only at  $T_g$ .

In many cases interesting qualitative results have been obtained, but in general no quantitative analysis of the data was made, probably because the relative complexity of conventional insulating glasses makes interpretation difficult; indeed the only property that has been analyzed quantitatively and compared to macroscopic measurements is the diffusion constant (Craig and Sutin, 1963 [100] and Elliott *et al.*, 1966 [95]).

We present here the first measurement of the glass transition in a metallic glass by Mössbauer spectroscopy. Such a study has a two-fold interest. First, we are interested in the microscopic dynamics of the metallic glass where we already know

the result of the atomic motion, *i.e.* we want to know *how* the structural changes described in the previous chapter occur. Secondly, metallic glasses are, in contrast to conventional glasses, structurally much less complex: there is less residual atomic ordering since metallic ions can be considered, to a good approximation, as spherical units, and the metallic bonding as isotropic (as can be seen from the fact that most metals have a close packed structure, and also that hard sphere models provide a good description of the structure of a metallic glass). Of course this is also why they crystallize so readily, which in most cases prevents prolonged measurements at high temperatures. Since metallic glasses are so simple, they are also the best model system to study the glass transition, as is shown by the popularity of molecular dynamics simulation of the glass transition in metallic glasses (see *e.g.* [49–52]). Indeed these measurements may provide an experimental comparison for such simulations by providing data on atomic motion, which otherwise are not readily available.

Since the structure of metallic glasses is simple, and furthermore metallic glasses, and in particular  $\text{Pd}_{40}\text{Ni}_{40}\text{P}_{20}$ , are well characterized, we can analyze the data quantitatively and relate them to the macroscopic measurements of specific heat, thermal expansion and diffusion.

## 4.2 The Spectra

The furnace designed for the specific requirements of this experiment has already been described in Section 2.6.6. The same sample system was used as for structural relaxation, namely  $\text{Pd}_{40}\text{Ni}_{40}\text{P}_{20}$ , and for the same reason. However, special samples had to be cast as it was found that small ribbon pieces mounted in the same way as for the room temperature measurements (see Section 2.6.5) showed that slippage due to thermal expansion of the overlapping pieces caused random changes in the signal at different temperatures. The new sample doped with 0.3 at. %  $^{57}\text{Fe}$  was cast 9 mm wide, wide enough that only a single piece of material of uniform thickness

was needed as an absorber.

Three typical spectra, at room temperature, below and above  $T_g$ , are shown in Figure 4.3. The decrease of the absorption and the shift of the centroid of the spectra, due to the second order Doppler shift (see Section 2.6.2) and a broadening of the spectrum above  $T_g$  can be seen very clearly.

In an experiment in which the temperature is swept, such as calorimetry, glass transition and crystallization may be widely separated (see Section 3.2.1). This is not the case in isothermal measurements, so that the time available to collect a spectrum of sufficient quality is restricted. Crystallization appears in the spectra as an increase in the  $f$ -factor, because the iron atoms are more tightly bound in the crystalline lattice than in the glass or supercooled liquid. Indeed, even if only a small portion of the sample has crystallized, it will contribute most of the resonant absorption signal. In Figure 4.4 the increase of the absorption due to crystallization (at 603 K) with time is shown.

Before measurement, the sample was heated to 579 K (above  $T_g$ ) in order to remove all effects of irreversible relaxation. The data were taken in a random temperature sequence, so that deterioration of the sample is not concealed as a trend in the data. Four measurements at 524 K bracket the series. The order of the measurements was 524, 579, 524, 574, 544, 505, 566, 425, 317, 555, 474, 375, 534, 514, 582, 524, 587 and 524 K. Most spectra were collected for  $\approx 20$  h. The spectra at 579, 582 and 587 K were collected over shorter periods, 360, 50 and 50 min, respectively.

At 582 K and 587 K, the measured spectrum was saved every 10 min. These spectra were fitted separately to look for deterioration of the sample. The parameters did agree within error for the time series at 582 K, but not for the time series at 587 K, which showed an increase of the  $f$ -factor. Also the measurement at 524 K following the measurement at 587 K showed that the sample had begun to crystallize. Therefore these data were discarded.

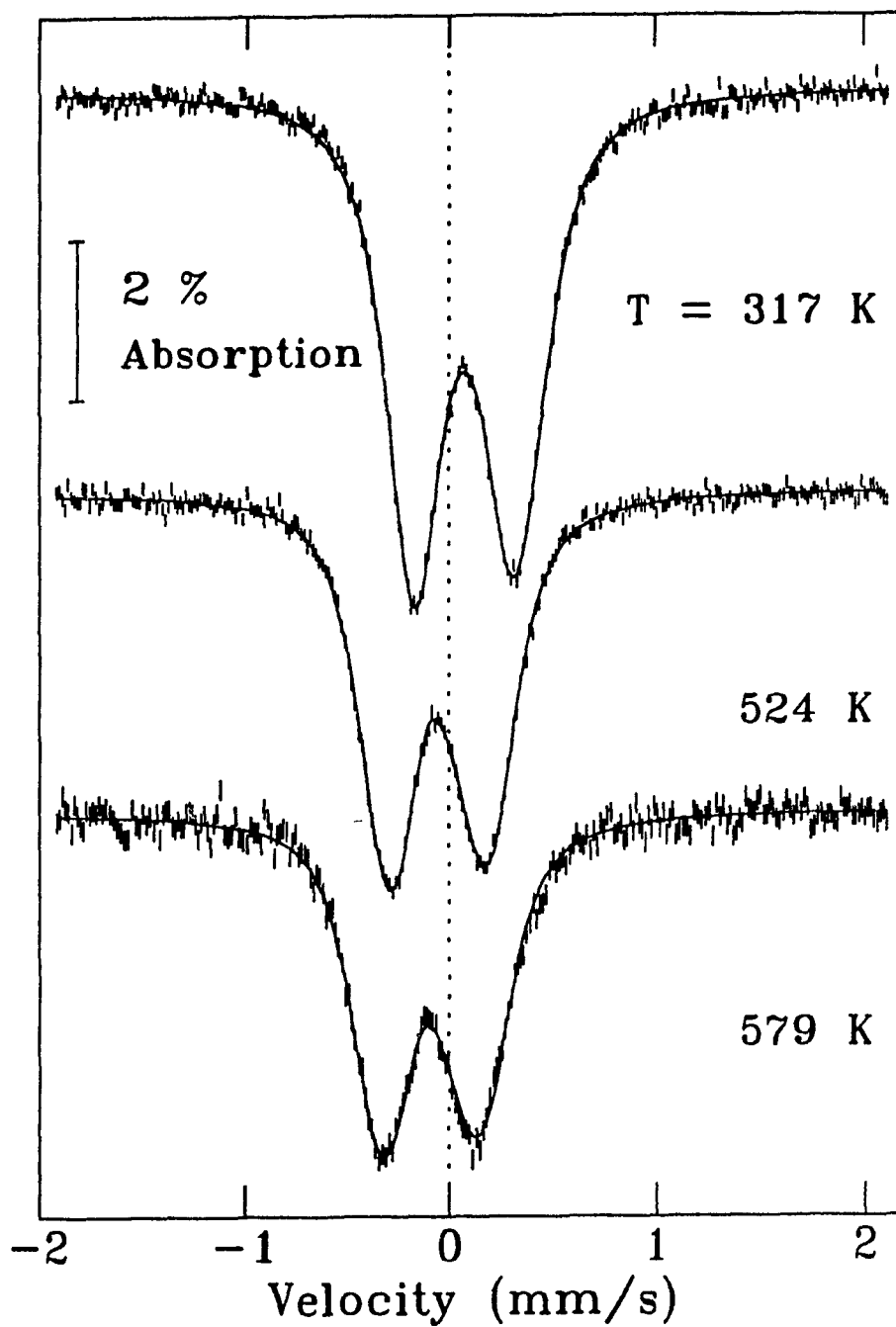


Figure 4.3: Mössbauer spectra of  $\text{Pd}_{40}\text{Ni}_{40}\text{P}_{20}$  at room temperature, below and above the glass transition temperature. The solid line is the fit to the data (see Section 4.3).

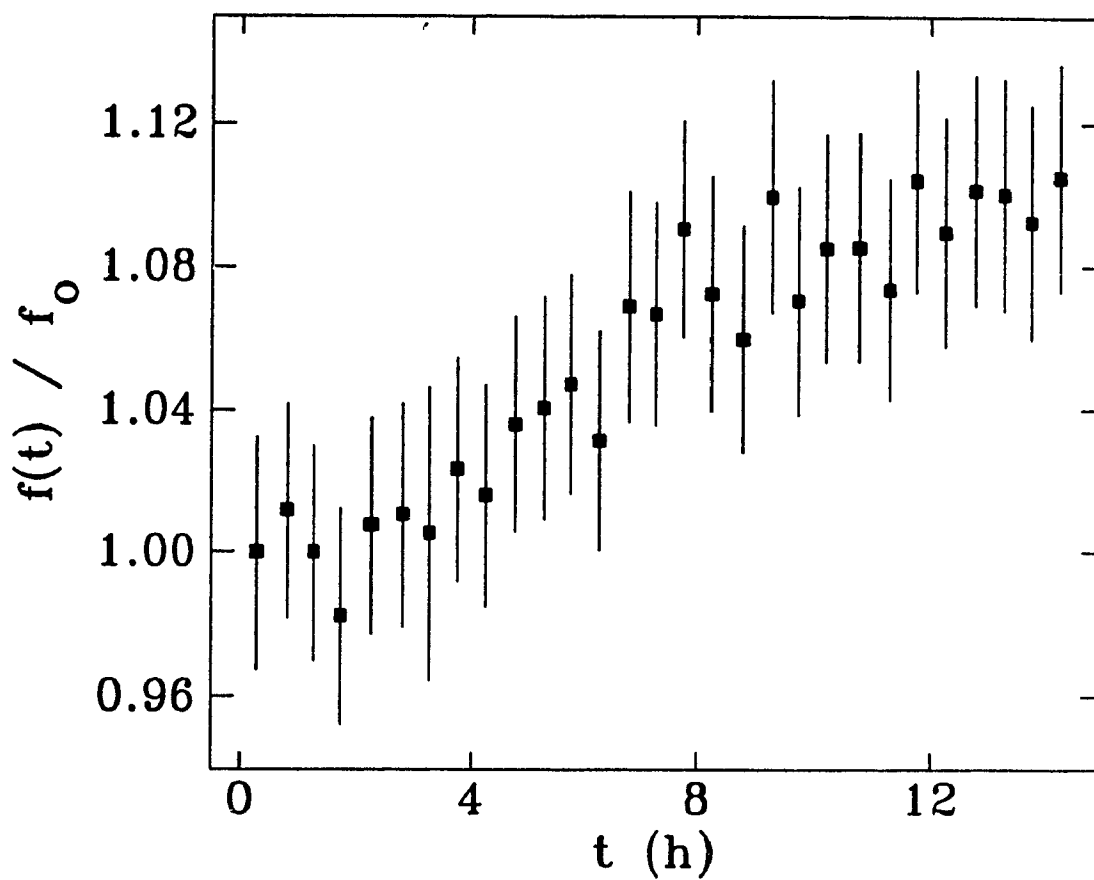


Figure 4.4: The increase of the  $f$ -factor during isothermal crystallization at 603 K. The  $f$ -factor was normalized to the initial value obtained for the amorphous sample,  $f_0$ .

### 4.3 Procedure for Fitting the Spectra

The general procedure for fitting data is the same as in Section 2.6.7. But, because we compare spectra at different temperatures, it is necessary proceed in a somewhat different way than in Section 3.4.

In the previous chapter we were interested in the changes of  $\sigma$ , the width of the quadrupole field distribution. The linewidth  $\Gamma$  was held fixed to the measured value of the instrumental resolution (since we do not expected that it to vary between different measurements at room temperature). Here we are interested in the diffusive broadening of the linewidth, so that we have to allow it to vary. Unfortunately  $\sigma$  and  $\Gamma$  cannot be varied simultaneously, because their effects on the spectrum are too similar; an attempt to do this gave fitted values of  $\Gamma$  that were below the instrumental resolution. For this reason we allowed only  $\Gamma$  to vary.  $\sigma$  was set to  $0.167 \text{ mm}^2/\text{s}^2$ , which is the value that was obtained by fitting the room temperature spectrum with  $\Gamma$  set to the instrumental resolution. We will show later in the data analysis that the changes of  $\Gamma$  at  $T_g$  result from a broadening of the linewidth, and not from an increase in  $\sigma$ . However, a small contribution of  $\sigma$  to the fitted value of  $\Gamma$  was taken into account (refer to Section 4.4.4).

Figure 4.5 shows that the correlation between the quadrupole splitting and the isomer shift,  $a$ , does not depend on the temperature if it is allowed to vary freely. To reduce the number of variable parameters in the fitting procedure - which makes the procedure more stable -  $a$  was held fixed at its average fitted value,  $4.5 \times 10^{-2}$ .

It is important to test whether the quality of the spectra affects the fitting parameters in any systematic way. Only if this is not the case is it possible to compare spectra that were collected for different times. The five spectra obtained as a time series at 582 K were added to form a compound spectrum, which was then fitted. The average of fitted parameters of the partial spectra was compared with the fitted parameters of the five spectra summed before fitting spectrum, and it was found that the values agree. The reason for the agreement is that the fitting

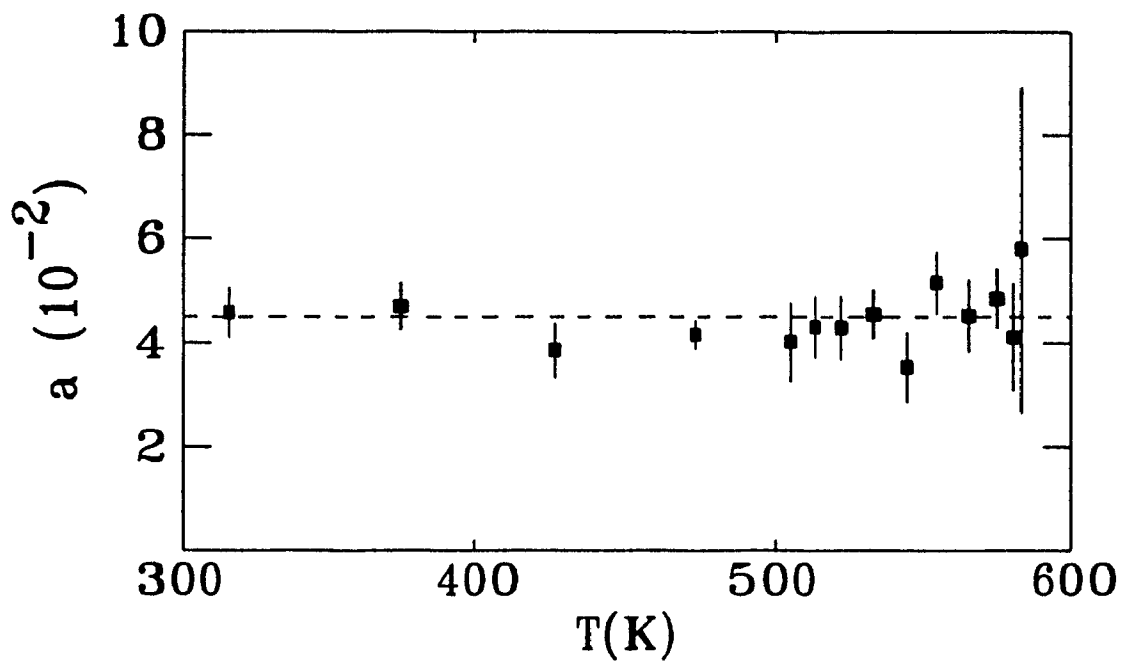


Figure 4.5: The temperature dependence of the correlation between the quadrupole splitting and the isomer shift  $a$ . The Figure shows that  $a$  does not depend on the temperature when it is allowed to vary, and thus data were fitted again with the value of  $a$  fixed to the average value indicated by the dashed line.

parameters have no strong correlations (for example, an error in the fitted value of the baseline cannot be offset by a shift in the fitted value of the absorption).

## 4.4 Data Analysis

### 4.4.1 The Recoil-Free Fraction

At the glass transition the recoil-free fraction decreases because the atoms are less tightly bound to their surrounding atoms. This decrease appears here at and above 566 K. The onset of the glass transition observed by the  $f$ -factor agrees well with the increase of volume expansion coefficient (measured by dilatometry at 10 K/min) and the heat flow (measured by DSC at 10 K/min) shown in Figure 4.6.b and 4.6.c.

The areas of the spectra are proportional to the  $f$ -factor, and therefore related to the amplitude of motion of the iron atoms. We cannot calculate the  $f$ -factor directly because several quantities are not known precisely enough to calculate the constant of proportionality: the  $f$ -factor of the source, the number of absorbing iron atoms and the non-resonant absorption by the sample. The relation between  $f$  and the area of the spectra can however be obtained by extrapolating the area to zero temperature, and then using this value as the normalizing constant. Here we use the fact that the Debye model of solids in its high temperature limit ( $T > \Theta_D/2 \approx 150$  K) gives a linear relationship between  $T$  and  $\langle x^2 \rangle$ :

$$\langle x^2 \rangle = \frac{3\hbar^2 T}{M k_B \Theta_D}, \quad (4.4)$$

where  $\Theta_D$  is the Debye temperature and  $M$  is the mass of the atom (here  $^{57}\text{Fe}$ ). This relationship describes the data quite well, except above  $T_g$ . This fit to the data is shown by the line in Figure 4.6.a. The data in Figure 4.6.a are already normalized with the area at zero temperature, i.e.  $f$  extrapolates to 1. The fitted value for  $\Theta_D$  is  $(309 \pm 5)$  K. The data points above 560 K have been excluded from the data for the fitting, since for them the Debye model clearly is not valid.

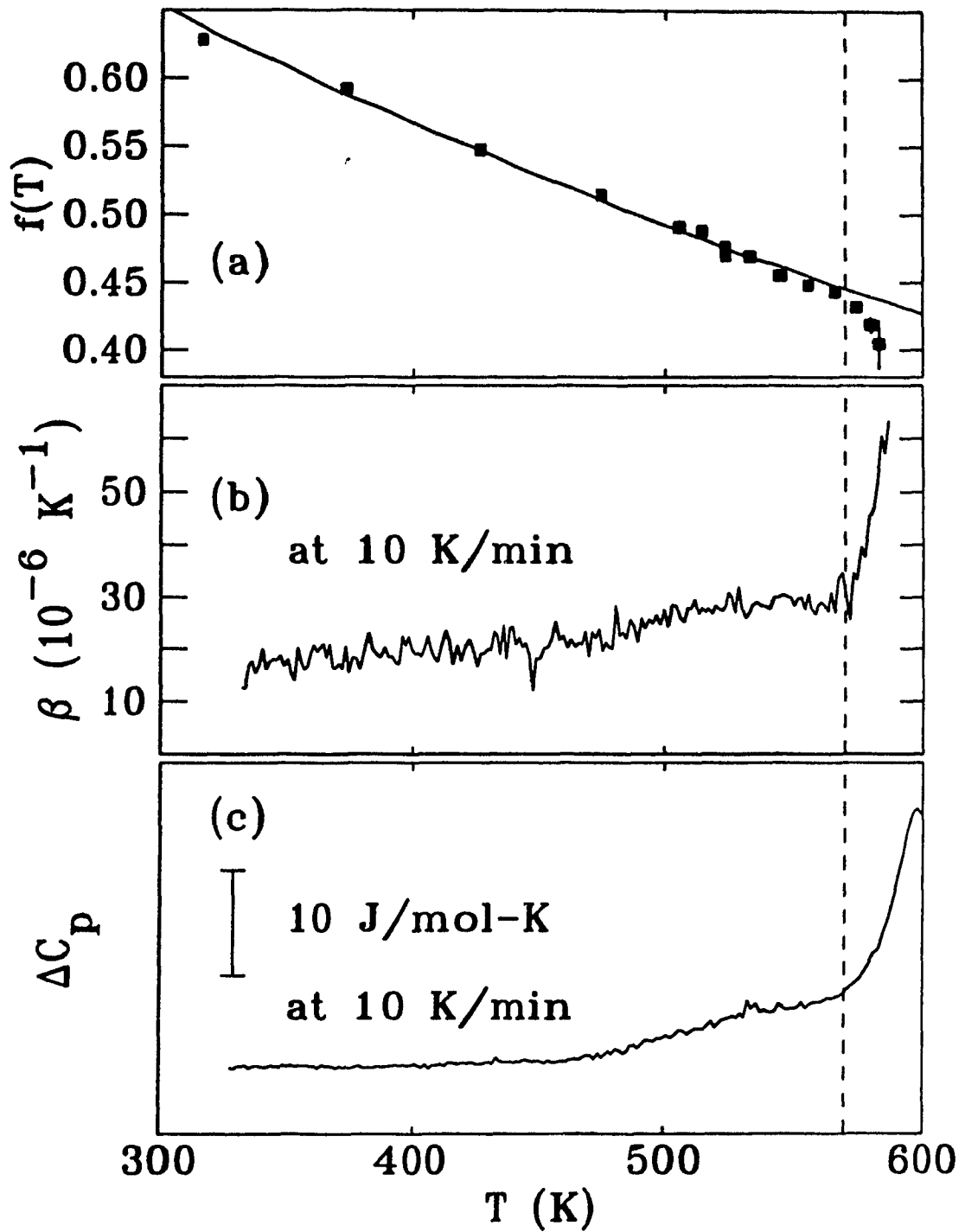


Figure 4.6: Observation of the glass transition in  $\text{Pd}_{40}\text{Ni}_{40}\text{P}_{20}$  by the change in  $f$ -factor (a), thermal expansion (b) and heat flow (c). The glass transition temperature is marked by the dashed line at 570 K. The solid line in (a) is a fit of the data below  $T_g$  to the Debye model.  $\Delta C_p$  (c) is the difference in heat flow between the amorphous and the crystallized sample.

$\sqrt{\langle x^2 \rangle}$ , the root mean square amplitude of vibration, is plotted in Figure 4.7. The amplitude of vibration,  $\sqrt{\langle x^2 \rangle}$ , is 0.088 Å and 0.12 Å at room temperature and  $T_g$ , respectively. This corresponds to a maximum displacement of 0.24 Å and 0.34 Å.

The onset of the change in the volume expansion and the change in  $\langle x^2 \rangle$  occur at the same point. The question arises whether the volume of the sample and  $\langle x^2 \rangle$  may be related to each other. (Figure 4.8 shows the volume increase of the sample as a function of temperature.) The Debye model does not consider thermal expansion, since it only describes the vibration of the atoms with a harmonic interatomic potential, and cannot lead to a displacement of the equilibrium positions of the atoms. Thermal expansion results from an anharmonic interatomic potential, of which the simplest (and lowest order) form is [111]:

$$U = cx^2(1 - \alpha x),$$

where  $x$  is the displacement of the atom from the minimum of the potential and  $\alpha x$  a small anharmonic correction. The constant  $c$  is related to the Debye temperature by:

$$c = \frac{Mk_B^2\Theta_D^2}{3\hbar^2}.$$

The thermal average for  $x^2$  is:

$$\langle x^2 \rangle = \frac{k_B T}{c} [1 + O(\alpha^2 \langle x^2 \rangle)], \quad (4.5)$$

as in the classical limit of the Debye model. The thermal average of  $x$  is:

$$\langle x \rangle = \frac{3\alpha}{4c} k_B T + [1 + O(\alpha^2 \langle x^2 \rangle)]. \quad (4.6)$$

This term gives rise to the thermal expansion.  $\langle x \rangle$  is related to the volume,  $V$ , of the sample by:

$$\frac{V(T)}{V_0} = 1 + \frac{3\langle x \rangle}{2R_0} + O(\langle x \rangle^2/R_0^2),$$

where  $V_0$  is the classical extrapolation of the volume to zero temperature (without zero point motion) and  $2R_0$  the diameter of the atomic site at zero temperature.

Thus:

$$\frac{V(T)}{V_0} = 1 + \frac{9\alpha k_B T}{8R_0 c}. \quad (4.7)$$

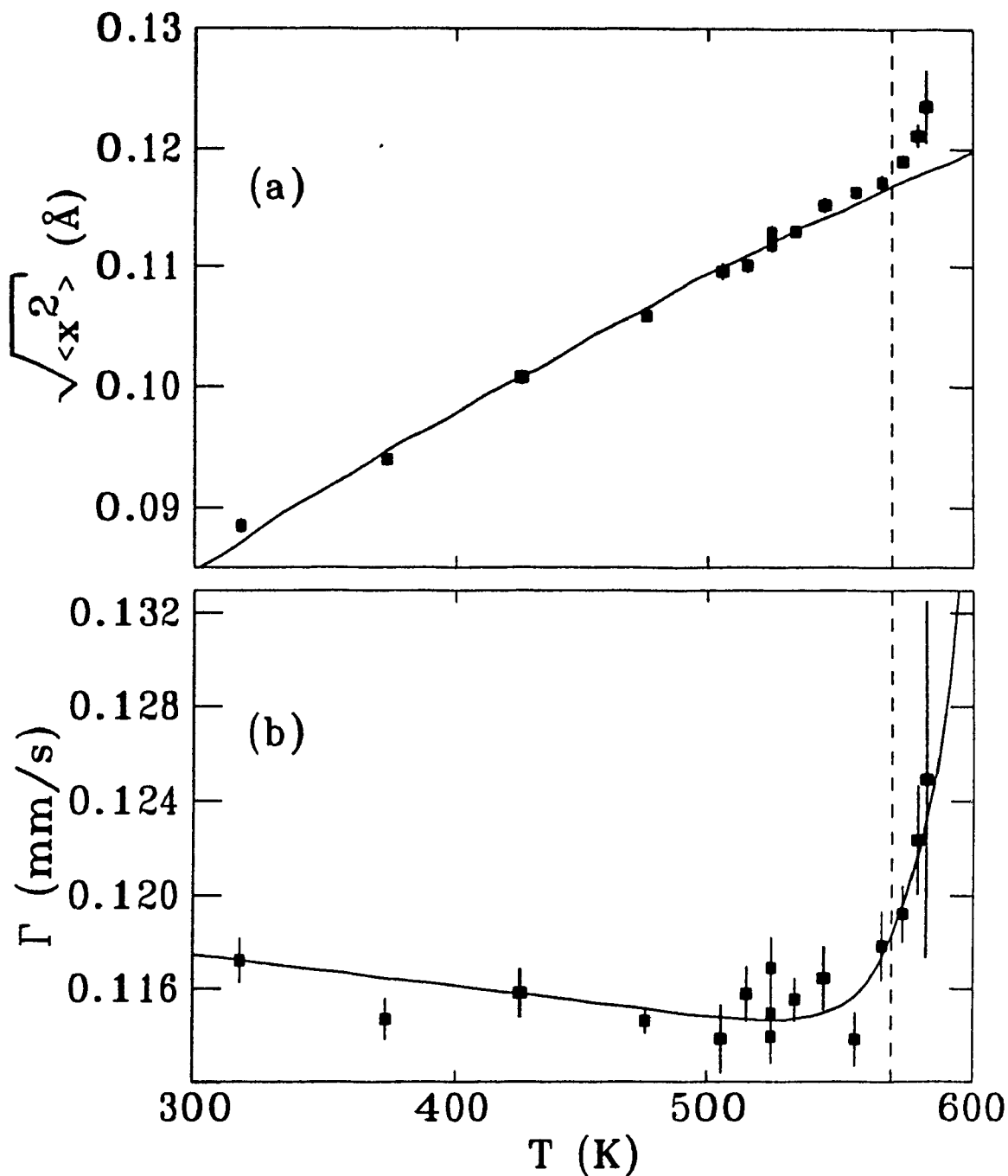


Figure 4.7: The root mean square amplitude of atomic vibration (a) and the diffusion line broadening (b) between room temperature to above  $T_g$ . The dashed line indicates  $T_g = 570$  K. The solid line in (a) is the fit of the data below  $T_g$  to the Debye model. The solid line in (b) is a fit of the linewidth to the atomic diffusion (see Section 4.4.4). The onset of the line broadening is about 20 K below  $T_g$ .

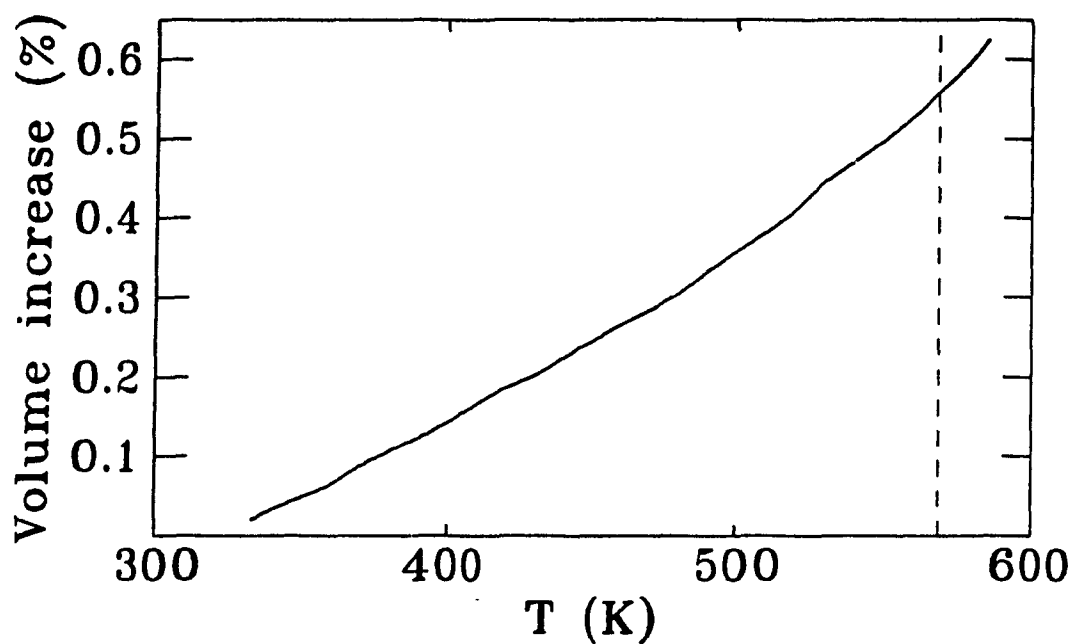


Figure 4.8: The volume increase of amorphous  $\text{Pd}_{40}\text{Ni}_{40}\text{P}_{20}$  as a function of temperature, measured with respect to the volume of the sample at 320 K.  $T_g$  is marked by the dashed line. The volume expansion coefficient  $\beta$  in Figure 4.6.b was obtained by taking the derivative of this curve.

If we take  $R_0$  as the radius of the iron atom,  $\approx 1.26 \text{ \AA}$ , we may obtain, by extrapolating  $V(T)$  to obtain  $V_0$ , the estimate  $\alpha = 0.5 \text{ \AA}^{-1}$ . This shows that the correction terms in the Equations 4.5 and 4.6 may indeed be neglected.

Equation 4.5 and 4.7 predict a linear temperature dependence, which is only an approximation of the data and which is in particular not followed at  $T_g$ . Both Equations contain the parameter  $c$ , which is proportional to  $\Theta_D^2$ . Therefore, by eliminating  $c$ , we will be able to test how these quantities are related. The Debye model is only an approximation of the behavior of the solid, as we have already seen from the discussion of the thermal expansion (and most solids deviate even more from the predictions of the Debye model than metals). In metal-metalloid glasses the most important cause for the deviations from the Debye model below the glass transition is the presence of several types of atoms, and thus different interatomic potentials (Tanaka *et al.*, (1986) [112]). It is common to represent the deviation of a solid from the behavior predicted by the Debye model as temperature dependence of  $\Theta_D$ . Eliminating  $c$ , and thus  $\Theta_D$ , from the Equations 4.5 and 4.7 gives:

$$\langle x^2 \rangle(T) = \frac{8R_0}{9\alpha} \left( \frac{V(T)}{V_0} - 1 \right). \quad (4.8)$$

Since we only have data above the temperature  $T_1 = 318 \text{ K}$  we write Equations 4.8 as:

$$\langle x^2 \rangle(T) = \frac{8R_0}{9\alpha} \frac{V(T_1)}{V_0} \left( \frac{V(T)}{V(T_1)} - 1 \right) + \langle x^2 \rangle(T_1). \quad (4.9)$$

This equation directly relates two experimentally observable quantities, the  $f$ -factor (Figure 4.6.a) and the macroscopic volume change (Figure 4.8). It should hold independently of a change in the Debye temperature.

In Figure 4.9 the measured value of  $\langle x^2 \rangle(T)$  is plotted against the value calculated by Equation 4.9, with the value of  $8R_0V(T_1)/(9\alpha V_0)$  as an adjustable parameter. This solid line, which was obtained from the volume expansion measurement, fits the data in over the whole temperature range, including the glass transition. Indeed is the fit to the data much better, even below  $T_g$ , than the Debye model (this fit is indicated by the dotted line). This shows that the macroscopic volume

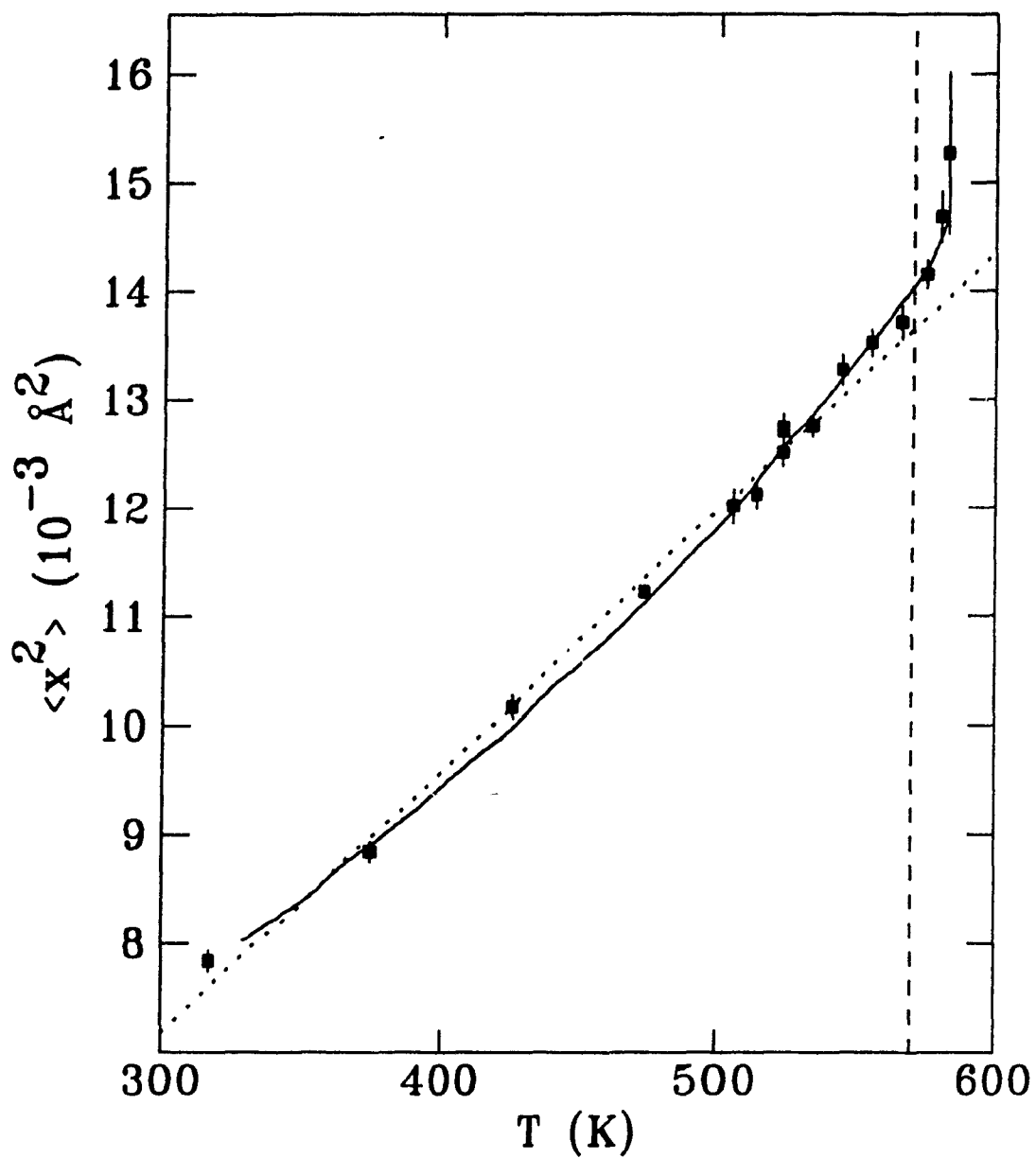


Figure 4.9: Comparison of the mean square vibrational displacement obtained from the  $f$ -factor and thermal expansion. The points give the value of  $\langle x^2 \rangle$  obtained from the  $f$ -factor. The solid line is the scaled volume expansion curve (see Equation 4.9). The dotted line is the best fit to the Debye model.

expansion and the microscopic atomic motion are controlled by a single variable (for example  $\Theta_D$ ).

Now we turn to the relation between the specific heat and the volume expansion coefficient. A comparison of Figure 4.6.b and Figure 4.6.c shows that the temperature dependence of these two quantities is strikingly similar. The reason for this is the relationship between the specific heat at constant pressure and the specific heat at constant volume:

$$C_P = C_V + TVE\beta^2, \quad (4.10)$$

where  $V$  is the volume and  $E$  is the Young's modulus. Independent of whether the system is in the glassy state or in the crystalline state,  $C_V$  is  $3k_B T$ , since the high temperature limit of the Debye model applies here. In particular, this relation is independent of a change in  $\Theta_D$ . The temperature dependence of  $C_P$  which we observe by calorimetry is thus entirely due to the second term in Equation 4.10, which arises from the volume dependence of the internal energy. We will now look at the differences between the specific heat and the volume expansion of the glass and the crystal,  $\Delta C_P$  and  $\Delta\beta$ . Kui and Turnbull showed that for  $\text{Pd}_{40}\text{Ni}_{40}\text{P}_{20}$  there is no difference of specific heat between the glass and the crystal below 440 K [72]. Because of Equation 4.10 the same has to be true for  $\Delta\beta$ . For small  $\Delta C_P$  and  $\Delta\beta$  we may expand Equation 4.10, which gives:

$$\Delta C_P \approx TVE\beta(\Delta\beta).$$

The change in specific heat is therefore to first order proportional to the volume expansion, which shows that the also  $C_P$  may be mapped on the the temperature dependence of  $\Theta_D$ .

Thus we can map the amplitude of motion onto the volume expansion and the specific heat by eliminating the Debye temperature between room temperature to above  $T_g$ . This indicates that the change of these quantities is governed by a single, universal variable which may be used to fully describe the glass transition.

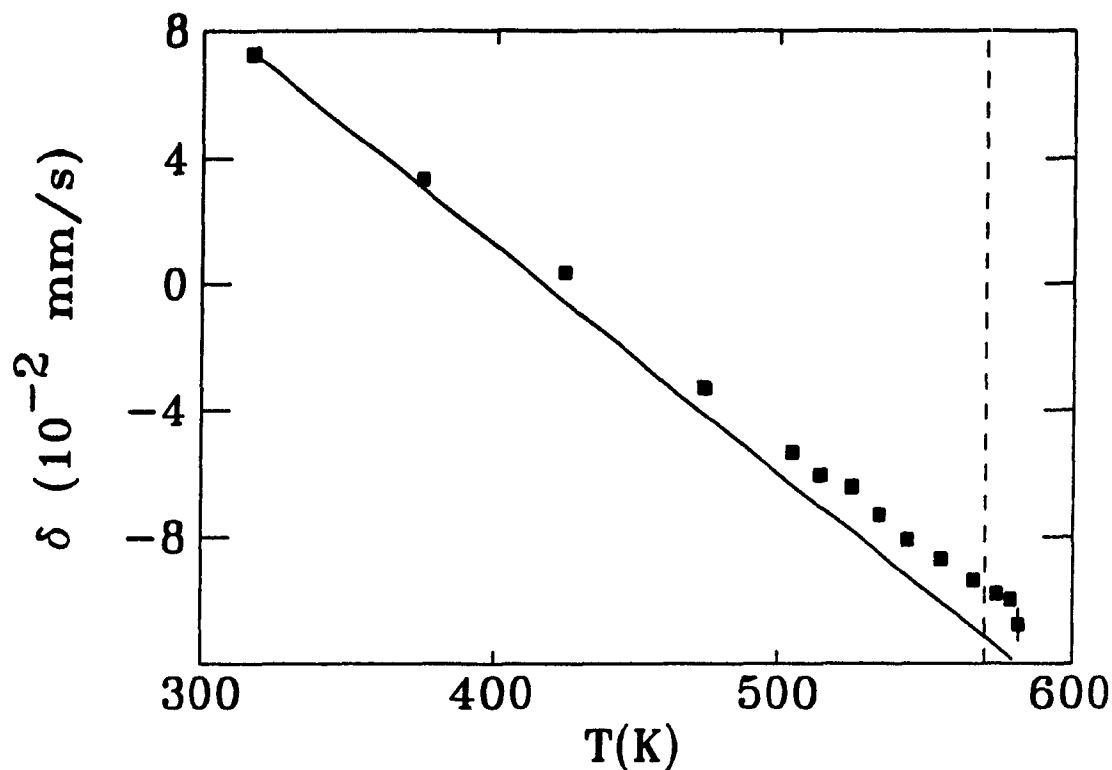


Figure 4.10: The temperature dependence of the center shift  $\delta$ . The solid line indicates the temperature dependence due to the SOD. The dashed line indicates  $T_g = 570$  K.

#### 4.4.2 The Center Shift

The behavior of the center shift,  $\langle\delta\rangle$ , is shown in Figure 4.10. The solid line shows the temperature dependence of the SOD (see Section 2.6.2),

$$\frac{\partial\langle\delta_{SOD}\rangle}{\partial T} = -\frac{3RE_\gamma}{Mc^2} = 7.31 \times 10^{-4} \frac{\text{mm}}{\text{sK}},$$

which clearly accounts for most of the effect. The residue gives the isomer shift  $\langle\delta_{ISO}\rangle$ , and is plotted in Figure 4.11. It is linear in temperature and shows no, or only very little, change at  $T_g$ , as in all non-metallic glasses apart from the oxide glasses (see Tables 4.1 and 4.2). The change in  $\langle\delta_{ISO}\rangle$  with temperature is most likely a result of the volume expansion, which changes the electron density at the nucleus. Taking an average value of the volume expansion coefficient (see Figure 4.6.b),  $\beta = 22 \times 10^{-6} \text{ K}^{-1}$ , the volume dependence of the isomer shift calculated from the slope

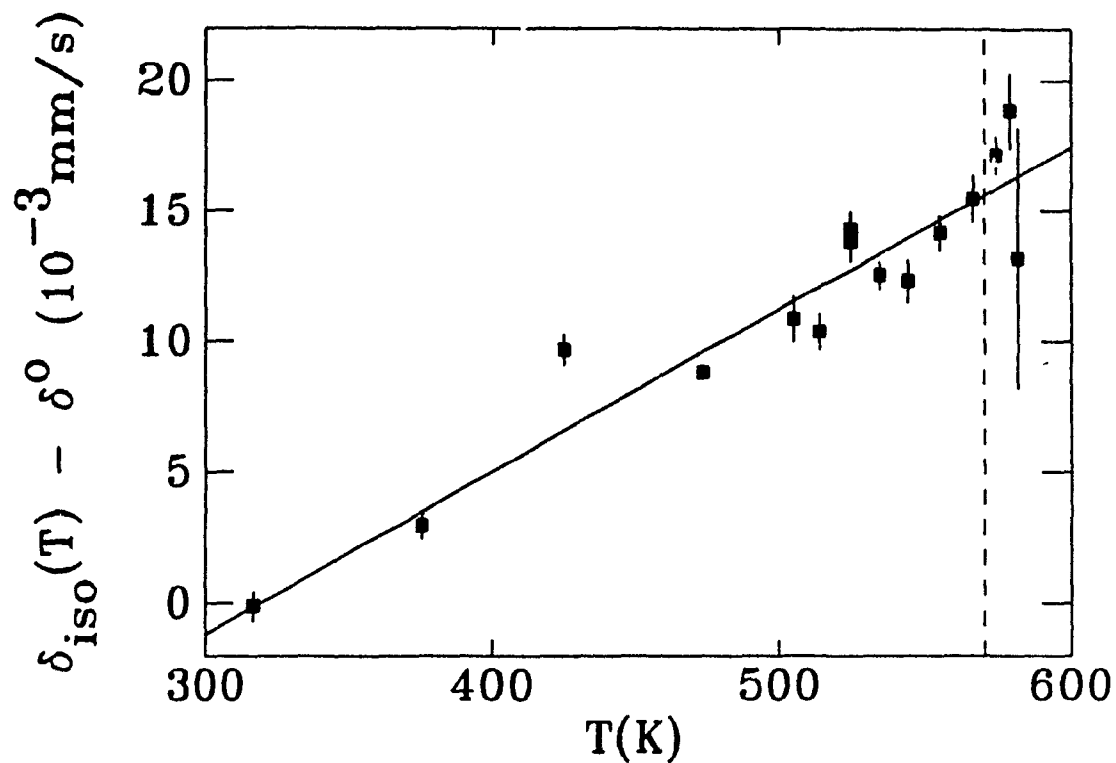


Figure 4.11: The temperature dependence of the center shift  $\delta_{ISO}$ .  $\delta^0$  is the isomer center shift at 317 K. The solid line gives the best fit to a linear temperature dependence with a slope of  $(6.2 \pm 0.5) \times 10^{-5} \text{ mm s}^{-1} \text{ K}^{-1}$ . The dashed line indicates  $T_g = 570 \text{ K}$ .

$\langle \delta_{ISO} \rangle$ ,  $(6.2 \pm 0.5) \times 10^{-5} \text{ mm s}^{-1} \text{ K}^{-1}$ , is:

$$\frac{\partial \langle \delta_{ISO} \rangle}{\partial \ln V} = \frac{1}{\beta} \frac{\partial \langle \delta_{ISO} \rangle}{\partial T} = 2.8 \text{ mm s}^{-1}.$$

This value is of the same order of magnitude as the volume dependence of  $\langle \delta_{ISO} \rangle$  for  $^{57}\text{Fe}$  in various metals, measured by applying pressure, ranging from 0.5 to  $1.8 \text{ mm s}^{-1}$ .

The volume expansion coefficient increases at  $T_g$ . This should be reflected in  $\langle \delta_{ISO} \rangle$ , but cannot be detected with certainty because the experimental error is too large. In addition, reversible relaxation effects may contribute changes in  $\langle \delta_{ISO} \rangle$  of up to  $6 \times 10^{-3} \text{ mm/s}$  (see Figure 3.25.c).

### 4.4.3 The Quadrupole Splitting

Figure 4.12 shows  $\langle Q \rangle$  as a function of temperature. Within experimental error no change occurs at  $T_g$ . The slight decrease between 520 and 570 K is consistent with reversible relaxation effects, which may cause changes of up to  $4 \times 10^{-3} \text{ mm/s}$  (Figure 3.25.a).

The temperature dependence of the quadrupole splitting in non-cubic metals is generally described by the empirical relationship [58]:

$$Q(T) = Q_0(1 - mT^{3/2}). \quad (4.11)$$

The coefficient  $m$  is inversely proportional to the force constant in the harmonic term of the interatomic potential,  $c$ :

$$m \propto \frac{1}{M\Theta_D^2}.$$

Calculations have related this expression to the screening by the conduction electrons in the metal and the increase in the amplitude of motion (Jena, 1975 [113] and Nishiyama *et al.*, 1976 [114]). The solid line in Figure 4.12 is a fit to Equation 4.11, with the value  $m = (7.5 \pm 0.3) \times 10^{-6} \text{ K}^{-3/2}$ . Deppe and Rosenberg found as an empirical approximation for metallic glasses [115,116]:

$$m \times 10^6 \text{ K}^{3/2} = -18 + \left( \frac{11}{M\Theta_D^2} \right) \times 10^7 \frac{\text{K}^2 \text{g}}{\text{mol}}.$$

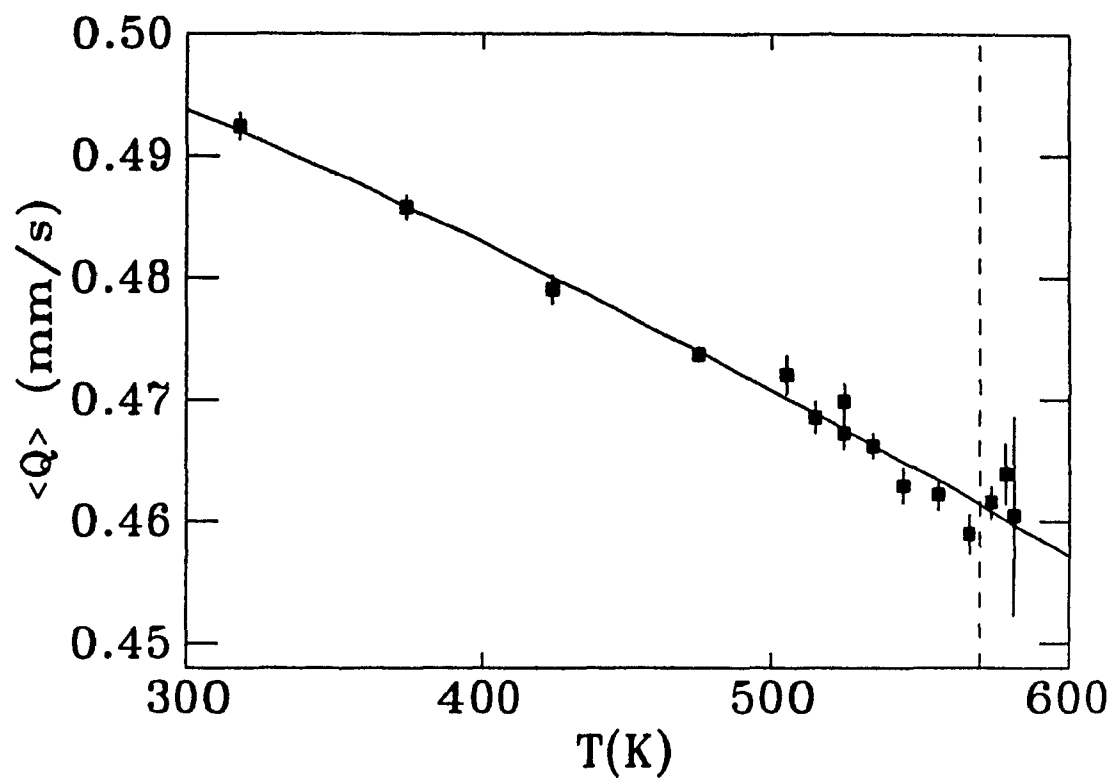


Figure 4.12: The temperature dependence of the mean quadrupole splitting  $\langle Q \rangle$ . The solid line shows the best fit to the  $T^{-3/2}$  dependence (Equation 4.11). The dashed line indicates  $T_g = 570$  K.

Using this relationship, we obtain  $\Theta_D \approx 280$  K, in fair agreement with the value of 309 K determined from the temperature dependence of the  $f$ -factor.

As in the case of the isomer shift, the relatively large experimental errors cover the changes of  $\langle Q \rangle$  caused by the change of  $\Theta_D$  at  $T_g$ .

#### 4.4.4 The Linewidth

Figure 4.7.b shows the values obtained by  $\Gamma$  as a function of temperature while keeping the width of the quadrupole distribution,  $\sigma$ , fixed to the value obtained from the room temperature spectrum. The linewidth increases strongly at  $T_g$  as atomic diffusion starts to be significant on the time scale of the Mössbauer event. A comparison with Figure 4.7.a shows that the observed onset of diffusion is about 20 K below the onset of the glass transition measured by the  $f$ -factor.

Before proceeding to analyze these data further, we have to consider the possibility that the increase of  $\Gamma$  at  $T_g$  might be due to an increase in the width of the quadrupole field distribution. If the atomic environment changes during the Mössbauer event (which it most certainly will at  $T_g$ ), the mean value of  $Q$  will decrease because of the time averaging of the electric field gradient. As  $\langle Q \rangle$  approaches zero, the shape of the spectrum changes completely to a single, broad line, which narrows at even higher temperatures, (Lindley and Debrunner, 1966 [117]). Here, however, the decrease of  $\langle Q \rangle$  was only 7% over the whole temperature range, and this decrease could be accounted for result by the increase of the vibrational motion. No measurable change of  $\langle Q \rangle$  occurred at  $T_g$ . Thus we can safely assume that the increase in  $\Gamma$  at  $T_g$  is caused by diffusional line broadening.

The fitted value of  $\Gamma$  decreases with increasing temperature. Since the natural linewidth cannot decrease, this decrease must be due to a decrease of  $\sigma$ . A decrease of  $\sigma$  with temperature is most likely a result of the decrease of  $Q$  (Equation 4.11), which affects  $\sigma$  as well as  $\langle Q \rangle$ . When we fit the data in Figure 4.7.b, we take the decrease of  $\sigma$  into account by a linear term, which corrects the linewidth with a

coefficient  $S$ :

$$\Gamma_c(T) = \Gamma(T) - S(T - 318 \text{ K}). \quad (4.12)$$

The increase of  $\Gamma_c$  between 555 and 582 K is 0.010 mm/s. This corresponds to a rest time for the atom,  $\tau$  (see Equation 4.1), of 17  $\mu\text{s}$  at 582 K. This is quite long compared to the duration of the Mössbauer event, as one should expect as the line is broadened only by 6 %.

The diffusion constant depends exponentially on the temperature:

$$D(T) = D_0 \exp\left(-\frac{E_a}{k_B T}\right),$$

where  $E_a$  is the activation energy for diffusion. It is more convenient here to express  $D$  in terms of its value at  $T_g$ :

$$D(T) = D(T_g) \exp\left[\frac{E_a}{k_B} \left(\frac{1}{T_g} - \frac{1}{T}\right)\right],$$

where  $D(T_g)$  is the diffusion constant at  $T_g = 570 \text{ K}$ . This makes the numerical fit of the data more stable, and directly provides the quantity  $D(T_g)$  that may be compared to macroscopic diffusion data.

Assuming jump diffusion according to Equation 4.2, we may fit the linewidth to the relation:

$$\Gamma_c(T) = \Gamma_0 + \frac{12\hbar D(T_g)}{\langle r^2 \rangle} \exp\left[\frac{E_a}{k_B} \left(\frac{1}{T_g} - \frac{1}{T}\right)\right],$$

with the adjustable parameters  $E_a$ ,  $D(T_g)/\langle r^2 \rangle$  and  $S$  (from Equation 4.12). The solid line in Figure 4.7.b shows the best fit, and one can see that the sudden increase of the linewidth is well described by this relationship. The fitted value for  $E_a$  is  $(1.8 \pm 0.9) \text{ eV}$ . The product  $D(T_g)/\langle r^2 \rangle$  has the value  $(2.7 \pm 0.7) \times 10^4 \text{ s}^{-1}$ .

To obtain the diffusion constant, we have to estimate the value of  $\langle r^2 \rangle$ . The mean jump distance  $\sqrt{\langle r^2 \rangle}$  is most likely to be less than the interatomic spacing,  $\approx 2.5 \text{ \AA}$ , but certainly larger than the maximum displacement from the equilibrium position due to the vibrational motion at  $T_g$ ,  $\approx 0.17 \text{ \AA}$ . The onset of diffusion at  $T_g$

suggests that  $\sqrt{\langle r^2 \rangle}$  should be quite close to the latter limit. Using the value  $0.2 \text{ \AA}$ , we obtain:

$$D(T_g) \approx 1.1 \times 10^{-17} \frac{\text{m}^2}{\text{s}}.$$

Data for diffusion in metal-metalloid glasses have been compiled by Cantor and Cahn [81]. They found a universal behavior for each element, independent of the host matrix, as long as the temperature is rescaled with the glass transition temperature,  $T_g$ , which enables us to compare the data. Their plot of  $D(T)$  against  $T/T_g$  is reproduced in Figure 3.8. The diffusivity of iron at  $T_g$  is about  $10^{-18} \text{ m}^2/\text{s}$ .<sup>1</sup> This value is within error of our value, but the values for the diffusion (measured by tracer diffusion or Mössbauer spectroscopy) are only known within fairly large errors, the estimate of  $T_g$  might be slightly different, the rescaling of  $T$  with  $T_g$  induces some uncertainty, and finally the Mössbauer measurement includes, as we discussed above, diffusion processes which lead the atom back to its original position.

The slope in Figure 3.8 gives a value  $E_a = 33 k_B T_g = 1.6 \text{ eV}$ , where  $570 \text{ K}$  was taken here as the value for  $T_g$ , in good agreement with the value obtained here.

## 4.5 Discussion

The glass transition is generally understood as the freezing - or unfreezing - of degrees of freedom of the liquid. The transition is a cooperative effect; below  $T_g$  the atoms impede each other from moving freely. We have seen already in section 3.2.1 that the heating rate dependence of  $T_g$  indicates a behavior similar to that of a phase transition. From this point of view, the decrease of  $\Theta_D$ , a measure of the interatomic binding force, is a result of the glass transition on the length scale of a

---

<sup>1</sup>Here we assumed that iron is the diffusing atom. The alternative would be that the iron atom is moved temporarily because of the diffusive motion of another atom. The agreement of the values of  $D(T_g)$ , as well as the fact that at  $T_g$  the diffusivity of Fe is larger than the diffusivity of P or Pd, makes this unlikely. Unfortunately no diffusion data are available for Ni, so that it is still possible that the Ni atoms diffuse instead of, or as well as, the Fe atoms.

single atom.

We found that the maximum vibrational displacement of the iron atom at  $T_g$  is  $0.34 \text{ \AA}$ . The Lindemann melting formula relates the melting point,  $T_m$ , of solids to the vibrational displacement of the atoms at the melting point. According to this formula, the solid melts when the quantity:

$$t = \sqrt{\frac{\sum_i \langle x_i^2 \rangle}{r_s^2}},$$

where  $r_s$  is the root means square radius of a unit cell, attains some value, usually between 0.20 and 0.25 [118]. If we replace  $T_m$  by  $T_g$ , take the measured value  $\langle x^2 \rangle = 0.015 \text{ \AA}^2$  at  $T_g$  from Figure 4.9 and use the value  $r_s = 1.37 \text{ \AA}$  (see Figure 3.20), we find  $t = 0.15$  for amorphous  $\text{Pd}_{40}\text{Ni}_{40}\text{P}_{20}$ . This low value implies that the stability of the glass is less than the stability of crystalline solids.

Another, perhaps more valid criterion, to predict the glass transition temperature may be found by considering the structure of the glass. Lamparter and Steeb obtained the partial structure factors of  $\text{Ni}_{80}\text{P}_{20}$  by neutron diffraction measurements using isotopic substitution [82]. The widths of the nearest neighbor spheres are  $0.39 \text{ \AA}$  for Ni-Ni and  $0.32 \text{ \AA}$  for Ni-P. If we assume that the environments of the iron atoms are similar to the environments of the nickel atoms, we find that the maximum vibrational displacement at  $T_g$ ,  $0.34 \text{ \AA}$ , is very close to the width of the nearest neighbor peak. The width of the nearest neighbor peak - which varies only very little between room temperature and  $T_g$  - indicates the energetically possible nearest neighbor distances. The glass transition occurs when the structure of the glass - stable below  $T_g$  - cannot accommodate the amplitude of vibration any more. It necessarily must undergo a change at that point. This is the geometric equivalent of the explanation for the glass transition put forward by Kauzmann [68]: the specific heat of the supercooled liquid is much larger than the specific heat of the crystal, but the integrated difference in specific heat below the melting point may not exceed the heat of fusion (otherwise the enthalpy of the crystal would become larger than the enthalpy of the glass). This is shown schematically in Figure 3.1,

where the supercooled (line AB) liquid must undergo a transition to the glass above the temperature  $T_0$ .

From the validity of Equation 4.9 below and above  $T_g$  we conclude that the increase of the amplitude of motion of the atoms at  $T_g$  can be mapped onto the volume expansion of the glass. The same argument applies for the specific heat, since it is also related to the amplitude of motion by the Debye model. This indicates that all these phenomena are governed by the same order parameter, or in other words, that any one of these properties - or a temperature dependent Debye temperature - is suitable as an order parameter to describe the glass transition.

The diffusion of the iron atoms begins to be measurable at a temperature close to, but somewhat below,  $T_g$ . This might be a coincidence - that just at  $T_g$  the time necessary for diffusion becomes comparable to the lifetime of the excited state of  $^{57}\text{Fe}$ . The agreement of the data obtained by Mössbauer spectroscopy with the diffusion data measured macroscopically below  $T_g$  would support that it is indeed a coincidence.

On the other hand is it unlikely that the additional atomic motion above  $T_g$  should not affect diffusion. The data obtained here are unfortunately not sufficient to shed light on this problem. The viscosity is proportional to  $D(T)/T$  (Stokes-Einstein relation) and viscosity of  $\text{Pd}_{40}\text{Ni}_{40}\text{P}_{20}$  may be measured over a wider temperature range, from 552 to 602 K (Volkert and Spaepen, 1988 [27]). Even these data show no clear deviation from Arrhenian behavior. However, data obtained for  $\text{Pd}_{77.5}\text{Cu}_6\text{Si}_{16.5}$  deviate from the Arrhenius form [25]. They are better described by the Vogel-Fulcher relation:

$$\eta = \eta_0 \exp \left[ \frac{E_a}{(T - T_0)} \right], \quad (4.13)$$

where  $T_0$  is typically a temperature somewhat below, but of the order of,  $T_g$ . This explains why diffusion becomes measurable around  $T_g$ , as observed by most Mössbauer experiments. In two cases a sudden decrease of the activation energy for diffusion at  $T_g$  has been observed in Mössbauer diffusion studies (Abram and Mullen, [105], Ruby *et al.* [106], see Tables 4.1 and 4.2), which indicates an even more discontinuous

change of the diffusion behavior than predicted by Equation 4.13.

## Chapter 5

### Conclusion

This thesis has presented measurements of (a) the microscopic processes that occur during structural relaxation of a metallic glass, and (b) the motion of atoms in a metallic glass between room temperature and the glass transition. Three important experiments were made for the first time:

- The first measurement of reversible structural relaxation by x-ray diffraction. This experiment showed that there were two types of changes of topological short range order, which are independent from each other.
- The first measurement of structural relaxation in a metallic glass by Mössbauer spectroscopy. This experiment accessed the change of the average symmetry of the atomic sites, and gave information complementary to the radial distribution function obtained from x-ray diffraction.
- The first measurement of the glass transition by Mössbauer spectroscopy. This measurement made the atomic motion at the glass transition experimentally accessible.

To analyze the x-ray diffraction data, a technique was developed which should be applicable to amorphous solids in general. It could, for the first time, reliably extract changes of the x-ray density (the density deduced from the x-ray measurement

of the interatomic spacing), and it was able to quantify the change in atomic order. Because it is directly linked to a microscopic model of atomic motion, the type of spacial re-ordering can be distinguished and its spacial extend can be measured.

The main conclusions from the measurements on irreversible structural relaxation may be summarized as follows:

- Irreversible relaxation in metal-metalloid glasses involves an increase in density, and an increase in atomic order which conserves the density.
- The increase in x-ray density agrees with the increase in macroscopic density. This shows that the densification proceeds by the filling of voids which are much smaller than an atomic volume. The densification changes the average interatomic distance by of the atoms by  $2.6 \times 10^{-3} \text{ \AA}$ .
- The distribution of distances between the metal atoms became narrower (atomic ordering). The neighbor shells further away than the nearest neighbor shell are more strongly affected, which shows that the geometric constraints allow only small adjustments of the nearest neighbor shell structure. The displacement of the atoms necessary to cause the observed changes in the atomic order are about  $93 \times 10^{-3} \text{ \AA}$ .

The results of the measurements on reversible relaxation are:

- Unlike irreversible relaxation, reversible relaxation involves no change in density. However, annealing close to  $T_g$  increases the ordering of the metal atoms in a way similar to irreversible relaxation. Heating the glass to above  $T_g$  reverses this processes and broadens the distribution of metal atoms.
- Annealing at low temperature does not affect the distribution of the metal atoms. The remaining structural degree of freedom is a change in the symmetry of the atomic sites: as the glass minimizes its internal energy, on average more anisotropic sites develop. This behavior is reminiscent of phase

transitions, where the low temperature phase is always marked by a broken symmetry.

- In binary glasses and metal-metalloid glasses changes in chemical short range order play no detectable role. Instead the diffusivity of the elements is the main factor which determines the susceptibility of the glass to reversible relaxation.
- For the first time evidence has been found for reversible changes in chemical short range order in ternary glasses of the type FeCuZr.

The most important results of the measurement of the glass transition by Mössbauer spectroscopy are:

- Atomic motion may be split into vibrational motion and diffusion.
- The amplitude of motion of an iron atom in  $\text{Pd}_{40}\text{Ni}_{40}\text{P}_{20}$  is  $0.24 \text{ \AA}$  at room temperature and  $0.34 \text{ \AA}$  at  $T_g$ . The value at  $T_g$  is similar to the width of the distribution of metal-metal nearest neighbor distances. This indicates that the structure of the glass must undergo a change when the amplitude of atomic vibration exceeds the intrinsic structural disorder, which provides a volume that is easily accessible for vibrational motion.
- The thermal expansion of the glass and the mean square vibrational displacement of the atoms have the same temperature dependence. The deviations from a linear behavior below and at the glass transition can in both instances be mapped onto the change of a single parameter (for example the Debye temperature).
- The diffusional motion of iron at  $T_g$  observed by Mössbauer spectroscopy is in agreement with macroscopic measurements.

While this research has yielded much new and valuable information, it also raised several new questions which require future experiments for their answer.

- Here we have concentrated our efforts on the investigation of a metal-metalloid glass. However, the indications of CSRO changes in ternary metal-metal glasses make these systems particularly interesting for measurements of changes in the atomic structure. An experiment suited to address this problem might be anomalous x-ray scattering, which allows the determination of the partial structure factors.
- The method of analysis that has been developed for the evaluation of changes of amorphous diffraction patterns should be applied to measurements of the structural changes in monatomic glasses, such as amorphous selenium or silicon.
- In view of the Mössbauer measurement of the glass transition in  $\text{Pd}_{40}\text{Ni}_{40}\text{P}_{20}$ , a measurement of the change of the diffraction pattern through  $T_g$  seems feasible, in particular if use is made of synchrotron radiation as a high intensity source of x-rays. To our knowledge, such an experiment is has not been carried out on metallic glasses.
- The data here obtained on the glass transition and structural relaxation lend themselves for the direct comparison with computer simulations of metallic glasses, such as molecular dynamics calculations. While the data offer an experimental check for the validity of the simulations, the modeling may be used to further the understanding of experimental findings. For example, one might look for the rearrangement of the metalloid atoms at low annealing temperatures, and the scaling behavior at the glass transition in the results of computer simulations.

## References

- [1] M. From, *Ph.D. Thesis* (McGill University, Montreal, 1989).
- [2] M.J. Huijben and W. van der Lugt, *Journal of Physics F* **6**, L225 (1976).
- [3] G. Etherington and C.N.J. Wagner, *Proc. of the 5<sup>th</sup> Conf. on Liquid and Amorphous Metals*, C.N.J. Wagner and W.L. Johnson (eds.), *Journal of Non-Crystalline Solids* **61-62**, 325 (1984).
- [4] T. Egami, *Materials Research Bulletin* **13**, 557 (1977).
- [5] H.S. Chen, L.C. Kimerling, J.M. Poate and W.L. Brown, *Applied Physics Letters* **32**, 461 (1978).
- [6] A.I. Taub and F. Spaepen, *Acta metallurgica* **28**, 1781 (1980).
- [7] A. Kursmovic and M.G. Scott, *Scripta metallurgica* **14**, 1303 (1980).
- [8] H.S. Chen, *Journal of Applied Physics* **52**, 1868 (1981).
- [9] A.C. Anderson, C.C. Koch and J.O. Scarborough, *Physical Review B* **24**, 1156 (1982).
- [10] N. Morito and T. Egami, *IEEE Transactions on Magnetics* **19**, 1901 (1983).
- [11] R.W. Cahn, N.A. Pratten, M.G. Scott, H.R. Sinning and L. Leonardsson, *Materials Research Society Symposium Proceedings Vol. 28* (Elsevier, Amsterdam, 1984).
- [12] R.C. O'Handley, B.W. Corb, J. Megusar and N.J. Grant, *Journal of Non-Crystalline Solids* **61+62**, 773 (1984).
- [13] E. Balanzat and J.T. Stanley, *Acta metallurgica* **33**, 785 (1985).
- [14] H.Q. Guo, H. Kronmüller, N. Moser and A. Hofmann, *Scripta metallurgica* **20**, 185 (1986).
- [15] G. Dietz and F. Stanglmeier, *Journal of Physics F* **17**, 1847 (1987).
- [16] D.M. Herlach, H.W. Gronert, E.F. Wassermann and W. Sander, *Zeitschrift für Physik B* **65**, 353 (1987).
- [17] T. Egami, *Reports on Progress in Physics* **47**, 1601 (1984).
- [18] T. Egami, *Proc. Int. Workshop on Amorphous Metals and Semiconductors*, P. Haasen and R.I. Jaffee ed. (Pergamon, Oxford, 1986).
- [19] M.R.J. Gibbs and G. Hygate, *Journal of Physics F* **16**, 809 (1986).
- [20] R. Brüning, Z. Altounian and J.O. Ström-Olsen, *Journal of Applied Physics* **62**, 3633 (1987).
- [21] H.S. Chen, *Journal of Applied Physics* **49**, 3289 (1978).

- [22] G. Hunger, H.U. Fritsch and H.W. Bergmann, *Materials Research Society Symposium Proceedings Vol. 28*, (Elsevier, Amsterdam, 1984).
- [23] D. Turnbull and M.H. Cohen, *Journal of Chemical Physics* **34**, 120 (1961).
- [24] F. Spaepen, *Acta metallurgica* **25**, 407 (1976).
- [25] S.S. Tasao and F. Spaepen, *Acta metallurgica* **33**, 881 (1985).
- [26] S.S. Tasao and F. Spaepen, *Acta metallurgica* **33**, 891 (1985).
- [27] C.A. Volkert and F. Spaepen, *Proc. of the 6<sup>th</sup> Int. Conf. on Rapidly Quenched Metals*, R.W. Cochrane and J.O. Ström-Olsen (eds.), *Materials Science and Engineering* **97**, 449 (1988).
- [28] A. van den Beukel and S. Radelaar, *Acta metallurgica* **31**, 419 (1983).
- [29] J.R. Cost, J.T. Stanley and B.J. Thijsse, *Proc. of the 6<sup>th</sup> Int. Conf. on Rapidly Quenched Metals*, R.W. Cochrane and J.O. Ström-Olsen (eds.), *Materials Science and Engineering* **97**, 523 (1988).
- [30] E. Kokmeijer, E. Huizer and B.J. Thijsse, *Proc. of the 6<sup>th</sup> Int. Conf. on Rapidly Quenched Metals*, R.W. Cochrane and J.O. Ström-Olsen (eds.), *Materials Science and Engineering* **97**, 505 (1988).
- [31] T. Egami, *Journal of Materials Science* **13**, 2587 (1978).
- [32] Y. Waseda and T. Egami, *Journal of Materials Science* **14**, 1249 (1979).
- [33] T. Mizoguchi, H. Narumi, N. Akutsu, N. Watanabe, N. Shiotani and N. Ito, *Proc. of the 5<sup>th</sup> Conf. on Liquid and Amorphous Metals*, C.N.J. Wagner and W.L. Johnson (eds.), *Journal of Non-Crystalline Solids* **61-62**, 285 (1984).
- [34] E. Chason, A.L. Greer, K.F. Kelton, P.S. Pershan, L.B. Sorensen, F. Spaepen and A.H. Weiss, *Physical Review B* **32**, 3399 (1985).
- [35] P. Schaal, P. Lamparter and S. Steeb, *Proc. 4<sup>th</sup> Int. Conf. on the Structure of Non-Cryst. Mat.* C.N.J. Wagner and A.C. Wright (eds.), *Journal of Non-Crystalline Solids* **137-146**, 56 (1988).
- [36] T.W. Wu and F. Spaepen, *Acta metallurgica* **33**, 2185 (1985).
- [37] K. Schild, F. Frisius, P. Lamparter and S. Steeb, *Zeitschrift für Naturforschung* **40a**, 551 (1985).
- [38] A.R. Yavari, *Journal de Physique Lettres* **46**, L-189 (1985).
- [39] P. Lamparter and S. Steeb, *Proc. 4<sup>th</sup> Int. Conf. on the Structure of Non-Cryst. Mat.*, C.N.J. Wagner and A.C. Wright (eds.), *Journal of Non-Crystalline Solids* **106**, 137 (1988).
- [40] Z. Yu, D. Rongheng, H. Gongxian and H. Zhongyi, *Journal of Materials Science Letters* **7**, 555 (1988).
- [41] G. Cocco, S. Enzo, A. Balerna, S. Mobilio and J.M. Dubois, *Physical Review B* **36**, 4734 (1987).

- [42] Y. Takahara, K. Hatade and H. Matsuda, *Transactions of the Japan Institute of Metals* **29**, 774 (1988).
- [43] P. Heubes, D. Korn, G. Schatz and G. Zibold, *Physics Letters* **74A**, 267 (1979).
- [44] G. Czjzek, J. Fink, F. Götz, H. Schmidt, J.M.D. Coey, J.P. Rebouillat and A. Liénard, *Physical Review B* **23**, 2513 (1981).
- [45] H.S. Chen, *Materials Science and Engineering* **23**, 151 (1976).
- [46] E. Wachtel, H. Haggag, T. Gödecke and B. Predel, *Zeitschrift für Metallkunde* **76**, 120 (1985).
- [47] A.J. Drehman, A.L. Greer and D. Turnbull, *Journal of Applied Physics Letters* **41**, 716 (1982).
- [48] H.W. Kui, A.L. Greer and D. Turnbull, *Journal of Applied Physics Letters* **45**, 615 (1984).
- [49] T.A. Weber and F.H. Stillinger, *Physical Review B* **31**, 1954 (1985).
- [50] J.J. Ullo and S. Yip, *Physical Review Letters* **54**, 1509 (1985).
- [51] H. Miyagaawa, Y. Hiwatari, B. Bernu and J.P. Hansen, *Journal of Chemical Physics* **88**, 3879 (1988).
- [52] F. Yonezawa, S. Nosé and S. Sakamoto, *Proc. of the 6<sup>th</sup> Conf. on Liquid and Amorphous Metals*, R. Hensel and E. Luscher (eds.), *Zeitschrift für Physikalische Chemie Neue Folge* **136**, 77 (1988).
- [53] R. Brüning, *M.Sc. Thesis* (McGill University, Montreal, 1986).
- [54] R. Richter, *Ph.D. Thesis* (McGill University, Montreal, 1988).
- [55] N.A. Pratten, *Journal of Materials Science* **16**, 1737 (1981).
- [56] H. Kuchling, *Taschenbuch der Physik* (VEB Fachbuchverlag, Leipzig, 1977).
- [57] R.C. Weast, *CRC Handbook of Chemistry and Physics, 66<sup>th</sup> Edition* (CRC Press, Cleveland, 1985).
- [58] B.P. Bardes, *Metals Handbook* (American Society for Metals, Metals Park, Ohio, 1979).
- [59] D.E. Cray, *American Institute of Physics Handbook, 3<sup>rd</sup> Edition* (McGraw-Hill, New York, 1972).
- [60] B.E. Warren, *X-Ray Diffraction* (Addison-Wesley, Reading, 1969).
- [61] H.P. Klug and L.E. Alexander, *X-Ray Diffraction Procedures 2<sup>nd</sup> Edition* (John Wiley and Sons, New York, 1974).
- [62] N.N. Greenwood and T.C. Gibb, *Mössbauer spectroscopy* (Chapman and Hall, London, 1971).
- [63] G. Le Caër, J.M. Cadogan, R.A. Brand, J.M. Dubois and H.J. Güntherodt, *Journal of Physics F* **14**, L73 (1984).

- [64] B. Kolk, A. Bloch, D.B. Hall, Y. Zheng and K.E. Patton-Hall, *Review of Scientific Instruments* **56**, 1597 (1985).
- [65] J. Hesse and A. Rübartsch, *Journal of Physics E* **7**, 526 (1974).
- [66] B. Window, *Journal of Physics E* **4**, 401 (1971).
- [67] S. Margulies and J.R. Ehrman, *Nuclear Instruments and Methods* **12**, 131 (1961).
- [68] W. Kauzmann, *Chemical Review* **43**, 219 (1948).
- [69] R.O. Davies and G.O. Jones, *Philosophical Magazine* **2**, 370 (1953).
- [70] A. Feltz, *Amorphe und glasartige anorganische Festkörper* (Akademie Verlag, Berlin, 1983).
- [71] A.Q. Tool, *Journal of The American Ceramic Society* **29**, 240 (1946).
- [72] H.W. Kui and D. Turnbull, *Journal of Non-Crystalline Solids* **94**, 62 (1987).
- [73] H.W. Gronert, F. Gillessen and D.M. Heilach, *Proc. of the 6<sup>th</sup> Int. Conf. on Rapidly Quenched Metals*, R.W. Cochrane and J.O. Ström-Olsen (eds.), *Materials Science and Engineering* **97**, 191 (1988).
- [74] H.E. Kissinger, *Analytical Chemistry* **29**, 1702 (1957).
- [75] Z. Altounian, *Proc. of the 6<sup>th</sup> Int. Conf. on Rapidly Quenched Metals*, R.W. Cochrane and J.O. Ström-Olsen (eds.), *Materials Science and Engineering* **97**, 461 (1988).
- [76] L. Schultz and E. Hellstern, *Materials Research Society Symposium Proceedings* Vol. 80, M. Tennyson, L.E. Tanner, and W.L. Johnson (eds.), **3** (1987).
- [77] R.B. Schwarz and W.L. Johnson, *Physical Review Letters* **51**, 415 (1983).
- [78] H.S. Chen, *Journal of Non-Crystalline Solids* **46**, 289 (1981).
- [79] A. Inoue, T. Masumoto and H.S. Chen, *Journal of Materials Science* **20**, 4057 (1985).
- [80] R.O. Suzuki and P.H. Shingu, *Proc. of the 5<sup>th</sup> Conf. on Liquid and Amorphous Metals*, C.N.J. Wagner and W.L. Johnson (eds.), *Journal of Non-Crystalline Solids* **61-62**, 1003 (1984).
- [81] B. Cantor and R.W. Cahn, *Amorphous Metallic Alloys*, F.E. Luborsky ed. (Butterworths, London, 1983).
- [82] P. Lamparter and S. Steeb, *Proc. of the 5<sup>th</sup> Int. Conf. on Rapidly Quenched Metals*, S. Steeb and H. Warlimont ed. (Elsevier, Amsterdam, 1984).
- [83] M. Maret, P. Chieux and P. Hicter, *Journal of Physics F* **17**, 315 (1987).
- [84] H.S. Chen, K.T. Aust and Y. Waseda, *Journal of Materials Science Letters* **2**, 153 (1983).
- [85] J.K. Percus and G.J. Yevick, *Physical Review* **110**, 1 (1958).

- [86] D. Srolovitz, T. Egami and V. Vitek, *Physical Review B* **24**, 6936 (1981).
- [87] Y. Suzuki, J. Haimovich and T. Egami, *Physical Review B* **35**, 2162 (1987).
- [88] M.E. Lines and M. Eibschütz, *Physical Review B* **27**, 5308 (1983).
- [89] G. Czjzek, *Physical Review B* **25**, 1908 (1982).
- [90] D. Williamson, *Mössbauer Isomer Shifts*, G.K. Shenoy and F.E. Wagner ed. (Elsevier, Amsterdam, 1978).
- [91] I. Vincze, F. van der Woude and M.G. Scott, *Solid State Communications* **37**, 567 (1981).
- [92] W.E. Lamb, *Physical Review* **55**, 190 (1938).
- [93] K.S. Singwi and A. Sjölander, *Physical Review* **120**, 1093 (1960).
- [94] C.T. Chudley and R.J. Elliott, *Proceeding of the Physical Society* **72**, 353 (1960).
- [95] J.A. Elliott, H.E. Hall and P. Bunbury, *Proceeding of the Physical Society* **89**, 595 (1966).
- [96] G. Vogl, *Proceedings of the International Conference on the Application of the Mössbauer Effect*, to appear in *Hyperfine Interactions*, (1990).
- [97] T. Heumann and R. Imm, *Journal Phys. Chem. of Solids* **29**, 1613 (1968).
- [98] D.W. James and G.M. Leak, *Philosophical Magazine* **14**, 701 (1966).
- [99] H. Bernas and M. Langevin, *Journal de Physique* **23**, 1034 (1963).
- [100] P.P. Craig and N. Sutin, *Physical Review Letters* **11**, 460 (1963).
- [101] A. Simopoulos, H. Wickman, A. Kostikas and D. Petrides, *Chemical Physics Letters* **7**, 615 (1970).
- [102] S.L. Ruby and I. Pelah, *Journal de Physique Colloque C6* **37**, C6-745 (1976).
- [103] B. Brunot, U. Hauser and W. Neuwirth, *Zeitschrift für Physik* **249**, 134 (1971).
- [104] S. Reich and I. Michaeli, *Journal of Chemical Physics* **56**, 2350 (1972).
- [105] A. Abras and J.G. Mullen, *Physical Review A* **6**, 2343 (1972).
- [106] S.L. Ruby, B.J. Zabransky and P.A. Flinn, *Mössbauer Effect Methodology* **6**, 21 (1971).
- [107] P.A. Flinn, B.J. Zabransky and S.L. Ruby, *Journal de Physique Colloque C6* **37**, C6-739 (1976).
- [108] F.J. Litterst, R. Ramisch and G.M. Kalvius, *Journal of Non-Crystalline Solids* **24**, 19 (1977).
- [109] W.J. LaPrice and D.L. Uhrich, *Journal of Chemical Physics* **72**, 678 (1980).
- [110] S. Bharati, R. Parthasarathy, K.J. Rao and C.N.R. Rao, *Solid State Communications* **46**, 457 (1983).

- [111] C. Kittel, *Introduction to Solid State Physics 6<sup>th</sup> Edition* (John Wiley & Sons, New York, 1986).
- [112] K. Tanaka, N. Soga, K. Hirao and K. Kimura, *Journal of Applied Physics* **60**, 728 (1986).
- [113] P. Jena, *Physical Review Letters* **36**, 418 (1975).
- [114] K. Nishiyama, F. Dimmling, T. Kornstrumpf and D. Riegel, *Physical Review Letters* **37**, 357 (1976).
- [115] P. Deppe and M. Rosenberg, *Hyperfine Interactions* **15-16**, 735 (1983).
- [116] M. Kopcewicz, B. Kopcewicz and U. Gonser, *Journal of Magnetism and Magnetic Materials* **66**, 79 (1987).
- [117] D.H. Lindley and P.G. Debrunner, *Physical Review* **146**, 199 (1966).
- [118] J.M. Ziman, *Principles of the Theory of Solids* (Cambridge University Press, Cambridge, 1964).